Beam Measurements of the Longitudinal Impedance of the CERN Super Proton Synchrotron

Alexandre Samir Lasheen

To cite this version:

Alexandre Samir Lasheen. Beam Measurements of the Longitudinal Impedance of the CERN Super Proton Synchrotron. Accelerator Physics [physics.acc-ph]. Université Paris Saclay (COmUE), 2017. English. NNT : 2017SACLS005 . tel-01565969

HAL Id: tel-01565969
https://theses.hal.science/tel-01565969

Submitted on 20 Jul 2017

NNT : 2017SACLS005

THÈSE DE DOCTORAT DE L'UNIVERSITÉ PARIS-SACLAY
PREPARÉE À L'UNIVERSITÉ PARIS-SUD

ÉCOLE DOCTORALE N°576
Particules Hadrons Énergie et Noyau : Instrumentation, Image, Cosmos et Simulation (PHENIICS)
Spécialité de doctorat : Physique des accélérateurs

Par
M. Alexandre Samir Lasheen

MESURES DE L'IMPÉDANCE LONGITUDINALE AVEC LE FAISCEAU DU CERN SUPER PROTON SYNCHROTRON

Thèse présentée et soutenue à Orsay, le 13 Janvier 2017

Composition du jury:
Dr. Guy Wormser, *LAL*, Président du jury
Prof. Costel Petrache, *CSNSM*, Directeur de thèse
Dr. Elena Shaposhnikova, *CERN*, Co-directrice de thèse
Prof. Jean-Marie De Conto, *LPSC*, Rapporteur
Prof. Mauro Migliorati, *Univ. La Sapienza*, Rapporteur
Dr. Elias Métral, *CERN*, Examinateur
Dr. Ryutaro Nagaoka, *SOLEIL*, Examinateur
Dr. Olivier Napoly, *CEA*, Examinateur

À ma famille, à Marie…

Un voyage de mille lieues commence toujours par un premier pas…

Acknowledgements

First and foremost, I would like to thank Elena Shaposhnikova for giving me the chance to do my PhD under her supervision. During these three years and since the very first day, her advice and guidance was always relevant and in my interest to progress. Thanks for sharing with me your immense knowledge, for your kindness and your endless curiosity that I will keep as a great source of inspiration as a researcher and for my life in general.

I would like also to thank Costel Petrache, for accepting to be my supervisor on behalf of the university. Costel was also my supervisor as a master's degree student, and supported me when I applied for a PhD at CERN. Thanks for always supporting me for my last steps as a student and the first ones as a researcher, allowing me to do this exciting work.

I am thankful to the members of the jury: Prof. Jean-Marie De Conto and Prof. Mauro Migliorati for accepting the important task to review the manuscript as referees, Dr. Elias Métral, Dr. Ryutaro Nagaoka and Dr. Olivier Napoly as members of the examining committee and Dr. Guy Wormser as president of the jury. Thanks for your interesting questions and remarks on my work.

The work presented here would not have been possible without the help of many colleagues. Since my arrival, I could always count on my exceptional office mates, Theodoros Argyropoulos and Juan Esteban Müller. Theo and Juan showed me all the tricks I needed to know to be efficient in my work, as well as being remarkable people. Thanks to both of you for making every working day enlightening, enjoyable and for your friendliness. In that respect, I would also like to thank Helga Timko for introducing me to the topic at my arrival, and Joël Repond to whom I introduced the topic in the end of my PhD.

Special thanks to Thomas Bohl and Steve Hancock, for helping me to tame the RF systems of the whole injector chain and showing me all I needed to know to perform autonomously beam measurements. Thanks for the countless hours you devoted me in the SPS BA3 Faraday cage and in the CPS island in the CCC, to share your knowledge with me.

My work was done in the Beams and RF section at CERN. I would like to thank all the members of this section where I felt well integrated and part of a great project, with special thanks to Simon Albright and James Mitchell for proofreading my thesis. I would like also to thank the students passing by and always bringing a great atmosphere.

The simulation code BLonD was used for all the simulations done during my PhD. The development of this code was the result of a fruitful collaboration, and I would like to thank Danilo Quartullo and Konstantinos Iliakis for maintaining and optimising the code, as well as Helga, Juan, Joël and Simon for their development.

The work presented in this thesis relies on the important work of the impedance team at CERN. Extensive efforts were devoted to develop the SPS impedance model, mainly by Jose Varela, Benoit Salvant, Carlo Zannini, with additional contributions from Thomas Kaltenbacher, Patrick Kramer, Christine Vollinger, Toon Roggen and Rama Calaga. Many thanks to all of you and for the fruitful discussions.
All the measurements presented in this thesis were made possible thanks to the help of Giovanni Rumolo and Hannes Bartosik as MD coordinators. Thanks for your confidence in my work, and for the beam time you gave me. I am also thankful to the SPS and CPS operation teams, for giving me their time to adjust the machine parameters.
Pour finir je tiens à remercier ceux par qui tout a commencé. Merci à mes parents et ma sœur pour leur soutien inconditionnel depuis mes tout premiers pas. Merci à toi Marie de m'avoir accompagné au quotidien et d'avoir donné tout son sens à ma vie.
Merci finalement à tous ceux qui ne sont pas nommés ici mais qui ont contribué à leur façon, par leurs encouragements, leur amitié, et leur bienveillance...

A.S.L.

Abstract

One of the main challenges of future physics projects based on particle accelerators is the need for high intensity beams. However, collective effects are a major limitation which can deteriorate the beam quality or limit the maximum intensity due to losses. The CERN SPS, which is the last injector for the LHC, is currently unable to deliver the beams required for future projects due to longitudinal instabilities.

The numerous devices in the machine (accelerating RF cavities, injection and extraction magnets, vacuum flanges, etc.) lead to variations in the geometry and material of the chamber through which the beam is travelling. The electromagnetic interaction within the beam (space charge) and of the beam with its environment are described by a coupling impedance which affects the motion of the particles and leads to instabilities for high beam intensities. Consequently, the critical impedance sources should be identified and solutions assessed. To have a reliable impedance model of an accelerator, the contributions of all the devices in the ring should be evaluated from electromagnetic simulations and measurements.

In this thesis, the beam itself is used to probe the machine impedance by measuring the synchrotron frequency shift with intensity and bunch length, as well as the line density modulation of long bunches injected with the RF voltage switched off. These measurements are compared with macroparticle simulations using the existing SPS impedance model, and the deviations are studied to identify missing impedance sources and to refine the model.

The next important step is to reproduce in simulations the measured single bunch instabilities during acceleration, in single and double RF system operation. Thanks to the improved impedance model, a better understanding of instability mechanisms is achieved for both proton and ion beams.

Finally, as the simulation model was shown to be trustworthy, it is used to estimate the beam characteristics after the foreseen SPS upgrades the High Luminosity-LHC project at CERN.

Key words: particle accelerators, longitudinal beam dynamics, beam-based measurements, CERN SPS, beam coupling impedance, beam instabilities

Résumé

Un des défis pour les futurs projets en physique basé sur les accélérateurs de particules est le besoin de faisceaux à hautes intensités. Les effets collectifs sont cependant une limitation majeure qui peuvent détériorer la qualité du faisceau ou limiter l'intensité maximale à cause des pertes. Le CERN SPS, qui est le dernier injecteur pour le LHC, n'est actuellement pas en mesure de délivrer les faisceaux requis pour les futurs projets à cause des instabilités longitudinales.

Les nombreux équipements dans la machine (les cavités RF accélératrices, les aimants d'injection et d'extraction, les brides de vide, etc.) entrainent des variations dans la géométrie et les matériaux de la chambre dans laquelle le faisceau transite. Les interactions électromagnétiques internes au faisceau (charge d'espace) et du faisceau avec son environnement sont représentées par une impédance de couplage qui affectent le mouvement des particules et mènent à des instabilités pour des intensités élevées de faisceau. Par conséquent, les sources d'impédance critiques doivent être identifiées et des solutions évaluées. Pour avoir un modèle d'impédance fiable d'un accélérateur, les contributions de tous les équipements dans l'anneau doivent être évaluées à partir de simulations et de mesures électromagnétiques.

Dans cette thèse, le faisceau lui-même est utilisé comme une sonde de l'impédance de la machine en mesurant le déplacement de la fréquence synchrotronique avec l'intensité et la longueur du paquet, ainsi que la modulation de longs paquets injectés avec la tension RF éteinte. Ces mesures sont comparées avec des simulations par macroparticules en utilisant le modèle d'impédance du SPS existant, et les déviations sont étudiées pour identifier les sources d'impédance manquantes pour raffiner le modèle.

L'étape suivante consiste à reproduire en simulations les instabilités mesurées pour un paquet unique durant l'accélération. Grâce à l'amélioration du modèle d'impédance, une meilleure compréhension des mécanismes de l'instabilité est rendue possible pour les faisceaux de protons et d'ions.

Finalement, le modèle pour les simulations étant digne de confiance, il est utilisé pour estimer les caractéristiques du faisceau après les améliorations prévues du SPS pour le projet High Luminosity-LHC au CERN.

Mots clefs : accélérateurs de particules, dynamique longitudinale du faisceau, mesures avec le faisceau, CERN SPS, impédance de couplage, instabilités du faisceau

Contents

Introduction

The CERN accelerator complex

Particle accelerators were originally designed to provide beams for nuclear and particle research, fulfilling various needs in terms of beam intensity, energy, as well as particle types. Many more uses of particle accelerators were then found, ranging from industrial applications to particle therapy for cancer treatment. Over the past years, technological progression have allowed an increased performance of particle accelerators, leading to important discoveries. The continuous need for higher beam intensities leads to reach the limits of machine performances defined by the electromagnetic fields induced by the beam. One of these limits are beam instabilities, which can degrade the beam quality and eventually lead to particle losses, and hence represent a limitation for future projects.

The European Organisation for Nuclear Research (CERN) hosts a wide chain of particle accelerators, including the well-known Large Hadron Collider (LHC) and many lower energy rings. The complete schematic map of the complex is shown in Fig. I.1. One of the most recent highlights at CERN is the discovery of a new boson compatible with the Higgs boson, produced from the collision of the two proton beams of the LHC at an energy of 3.5 TeV (7 TeV in the centre of mass) and measured by the ATLAS and CMS detectors [1, 2].

The number of events registered in the LHC experiments is given by the luminosity $\mathcal{L}$, which is determined by the number of particles in the colliding bunches N_b, with $\mathcal{L} \propto N_b^2$. To increase the number of events and therefore the probability to detect particles of interest, high bunch intensities are needed. This is also one of the requirements of the High Luminosity-LHC (HL-LHC) project [3], where the goal is to increase the luminosity by a factor of 10. One of the ingredients to achieve this aim is an increase in bunch intensity by a factor of 2 with respect to present operation. However, the collective (or intensity) effects will also increase, and this goal is currently not achievable without machine upgrades.

The LHC is filled by an injector chain consisting of several particle accelerators. Their role is to accelerate the beam up to the energy acceptable by the LHC. Protons are first accelerated in the Linear Accelerator 2 (LINAC2, up to a kinetic energy of 50 MeV), the Proton Synchrotron Booster (PSB, up to 1.4 GeV), the Proton Synchrotron (PS, up to 25 GeV) and finally the Super Proton Synchrotron (SPS, up to 450 GeV). The second role of the injector chain is to shape the

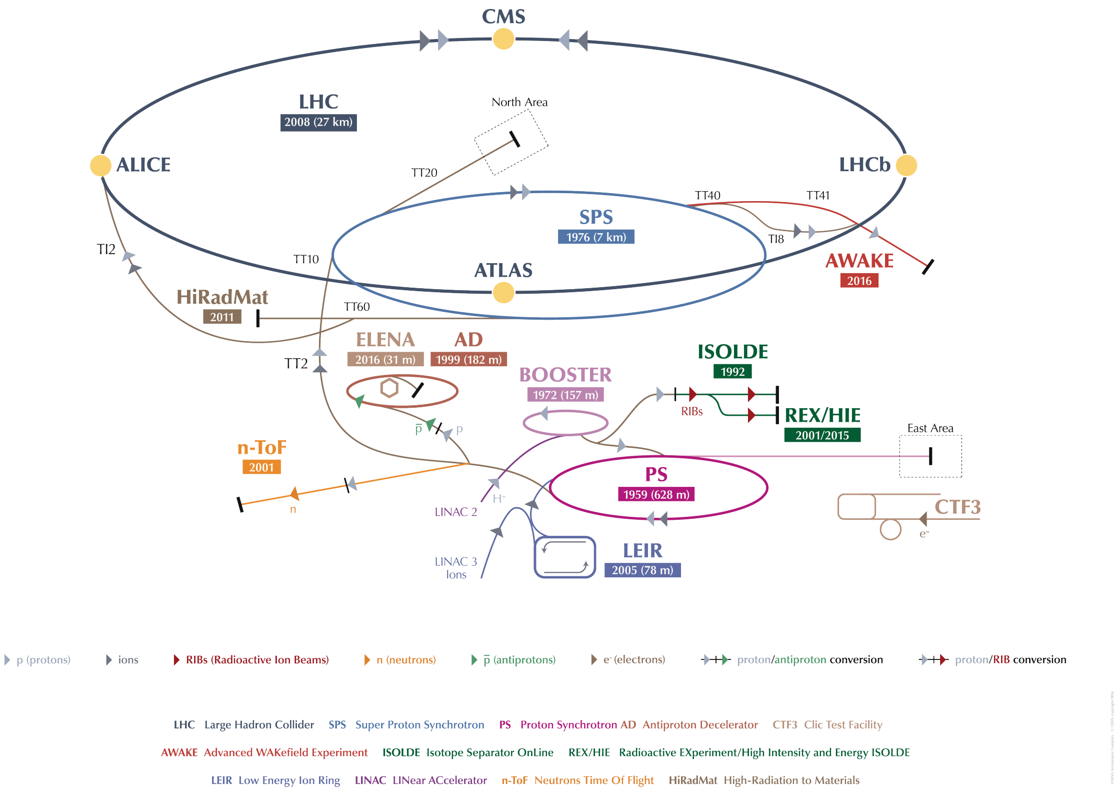

Figure I.1 – The CERN accelerator complex (© CERN).

beam in several bunches, with the time structure required by the LHC experiments. A single bunch is formed in the PSB and sent to the PS, where this bunch is split into several bunches using RF manipulations. In the nominal operation, 6 PSB bunches are split into 72 bunches spaced by 25 ns, where each bunch is composed of 1.2×10^{11} protons. Up to four batches of 72 bunches are injected from the PS into the SPS, and many injections are done to fill the LHC with the nominal number of bunches per beam. When the two counter-rotating beams are ready in the LHC, they are finally accelerated from 450 GeV to collision energy, which was 3.5 TeV during the LHC run 1 (2010-2013) and since the restart in 2015 is 6.5 TeV .

Each ring of the LHC injector chain has different limitations due to intensity effects. If a single accelerator in the chain is limited in its performance, the required beam is not able to reach the LHC and fulfil the needs of the experiments. The goal of the LHC Injectors Upgrade (LIU) project [4] is to identify the limitations and to find and implement solutions which would allow delivery of the beam required for the HL-LHC project. Presently, one of the main bottlenecks is the SPS due to beam loading and longitudinal instabilities (more details are below).

The injector chain is also able to accelerate ions for collisions in the LHC and fixed target experiments. The LIU project includes an upgrade of the injector chain for ion beams [5] for the HL-LHC project (Pb-Pb and p-Pb collisions). The ion beam follows a different path than the proton beam. The Pb beam is first accelerated in the Linear Accelerator 3 (LINAC3, up to a kinetic energy of 4.2 MeV/u), the Low Energy Ion Ring (LEIR, up to 72 MeV/u), then follows the same path as the proton beam in the PS (up to 5.9 GeV/u) and finally the SPS (up to 176.4 GeV/u).

Many other physics experiments are located at different stages in the CERN accelerator chain and also rely on the low energy accelerators. A relevant example in the frame of this thesis is the Advanced WAKefield Experiment (AWAKE) [6] at extraction from the SPS. The AWAKE project aims at studying plasma wakefield acceleration, which is expected to give much higher accelerating gradients with respect to conventional methods (order of GV/m in plasma wakefield acceleration, in comparison with order of MV/m in RF acceleration). In the future, this could lead to more compact particle accelerators for physics studies at the high energy frontier. The requirement to the SPS from the AWAKE project is a single bunch with a high density (small bunch length and high bunch intensity) at 400 GeV to be sent into a plasma chamber. However, the achievable bunch parameters are also limited by beam instabilities.

Both the HL-LHC and AWAKE projects rely on a successful acceleration of the required beam in the SPS. The intensity effects need to be well controlled since the delivered beam should be reproducible from one cycle to another and remain within the specifications. Therefore, it is necessary to study the intensity effects in the SPS, and in particular beam instabilities in the longitudinal plane. To do so, an accurate impedance model of the SPS is essential to identify the sources of the instabilities, and to hence find possible cures.

The CERN Super Proton Synchrotron and beam instabilities

The SPS was commissioned in 1976 and is presently the second largest accelerator at CERN, with a circumference of 6.9 km. During those 40 years, it was used as a proton-antiproton collider (Sp$\bar{\text{p}}$S), as an injector for the Large Electron Positron collider (LEP), and provided beams for various fixed target experiments (e.g., North Area experiments, CNGS, HiRadMat). The SPS accelerated all kind of particles: protons, antiprotons, electrons, various ions. It is also used as a test bench for new accelerator physics concepts and devices, an example being the crab-cavities which will be used in the HL-LHC project to increase the luminosity [3]. These cavities will be tested in the SPS before installation in the LHC. Major scientific discoveries were done using the SPS beam, for example the W and Z bosons in 1983 [7, 8]. The present SPS machine parameters are shown in Table I.1.

The versatility of the SPS was made possible thanks to many upgrades of the machine. However, this longevity implies that some elements in the machine were not designed in prevision of the requirements of the HL-LHC project, and are now a problem. The many devices, present in a particle accelerator, introduce some changes in the geometry of the vacuum chamber through which the beam is travelling. A particle passing through a cavity-like structure will deposit some energy in the form of an electromagnetic perturbation (wakefield). The frequency distribution of the wakefield, called the beam coupling impedance (or simply impedance below) depends on the geometry of the surroundings. This perturbation can affect the motion of the following particles within the same bunch (single bunch effects), the following bunches (multi-bunch effects), and even the same bunches at the following revolution turn (multi-turn effects). Due to the long history of the SPS, many impedance sources are present in the machine and are responsible for the present machine performance limitations. The intensity effects are different in transverse and longitudinal beam dynamics. In the SPS the limitations of the LHC beam are mainly due to the effects in the longitudinal beam dynamics, which are the main focus of this thesis. The beam parameters presently achieved in the SPS together with the goals of the LIU project are shown in Table I.2.

Table I.1 – Machine parameters of the CERN SPS for the LHC (protons and ions) and AWAKE beams. Values separated with / correspond to injection/extraction. Values with ~ are approximate and have small variations during the ramp.

Parameter		**LHC beam**	**LHC-ION beam**	**AWAKE beam**
Circumference C	[m]	6911.50		
Particle type and charge Z	[e]	p+ (Z=1)	^{208}Pb^{82+} (Z=82)	p+ (Z=1)
Momentum p	[Z GeV/c]	26/450	17/450	26/400
Lorentz factor γ		27.7/479.6	7.3/190.6	27.7/426.3
Transition Lorentz factor γ_t		Q20 optics: 17.95 – Q26 optics: 22.77		
Revolution period T_{rev}	[μs]	~23.1		
Main RF system				
Harmonic number h_{200}		4620		
RF frequency $f_{\mathrm{RF},200}$	[MHz]	~ 200.2		
Max. RF voltage V_{200}	[MV]	~ 7.5		
Fourth harmonic RF system				
Harmonic number h_{800}		18480	–	18480
RF frequency $f_{\mathrm{RF},800}$	[MHz]	~ 800.8	–	~ 800.8
Max. RF voltage V_{800}	[kV]	~ 850	–	~ 850

Table I.2 – Beam parameters achieved in the SPS for the LHC-type beam and goals of the LIU project [4]. Values separated with / correspond to injection/extraction.

Parameter		**Achieved**	**LIU target**
Number of batch×bunches		4×72	
Bunch spacing	[ns]	25	
Batch spacing	[ns]	225	
Bunch intensity N_b	$\times 10^{11}$	1.3/1.2	2.6/2.4
Longitudinal emittance ε_L	[eVs]	0.35/0.6	<0.65
Extracted bunch length $\tau_L = 4\sigma_{\mathrm{rms}}$	[ns]	1.65	<1.7
Transverse emittance $\varepsilon_{x,y}$	[μm]	2.36	1.89

Beam loading is one of the important SPS limitations. Beam acceleration in the SPS relies on the electric field (RF voltage) provided by a Travelling Wave RF System. It is composed of four Travelling Wave Cavities (TWC) tuned to a frequency of 200 MHz [9]. Each of them is composed of several sections, so the total system includes two TWC with four sections and two TWC with five sections. The available RF voltage for the acceleration is reduced by the wakefield left by the beam in the TWC (beam loading), and for the beam intensities required for the HL-LHC project the available voltage is no longer sufficient. An upgrade of the RF system is foreseen to overcome this limitation [10]. It consists of an increase in the total number of (shorter) cavities, which together with an upgrade of the RF power supply will allow a larger RF voltage to be reached in the TWC. The increased number of sections (from 18 to 20) will be reorganised to get a total of six TWC (four TWC with three sections and two TWC with four sections). With shorter cavities, the total impedance of the RF system is lower and the beam loading effect will be reduced. After this upgrade (2021), the available RF voltage is expected to be sufficient to accelerate a beam with the intensity required for the HL-LHC project. However, other limitations exist due to other SPS impedance sources.

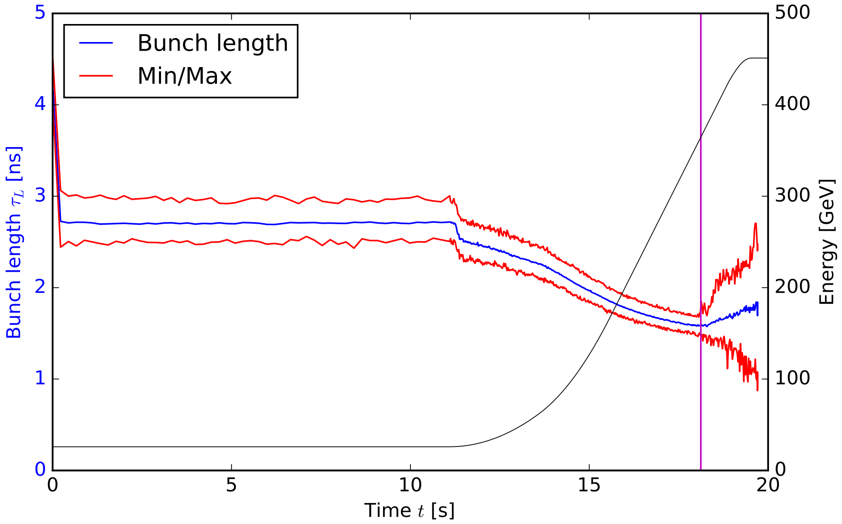

Figure I.2 – Longitudinal instability during the SPS accelerating cycle for a batch of 72 bunches spaced by 25 ns, with an average bunch intensity of $N_b \approx 1.2 \times 10^{11}$ ppb in the Q20 optics (see Table I.1). The average bunch length (blue) is shown, together with the beam energy (black) as a function of time. The minimum and maximum bunch lengths in the batch (red) are used as a criterion to determine when the beam becomes unstable, shown here with the vertical magenta line.

The cumulative effect of the wakefields on the beam can eventually lead to instabilities for high beam intensities. An example of measurements for the LHC type beam in the SPS is shown in Fig. I.2, where the beam becomes unstable during the acceleration ramp. The instability manifests in coherent oscillations of the bunch distribution (bunch length oscillations in this example), resulting in an uncontrolled increase of the longitudinal emittance and intensity losses. The bunch length at SPS flat top energy should not exceed 1.7 ns to minimise particle losses at injection into the LHC which has a 400 MHz RF system (twice shorter acceptable bunches compared to the SPS). In the example in Fig. I.2, the maximum bunch length within the batch is too large and this beam cannot be injected in the LHC.

The mechanism of the instability depends on multiple parameters: the longitudinal emittance, the bunch length and intensity, the RF voltage program, the optics, the impedance sources etc. The wakefields perturb the bunch motion. In the stable regime, this perturbation is damped naturally thanks to the spread in the frequencies of the individual particles composing the bunch (incoherent synchrotron frequency spread). This effect is called Landau damping, which was first introduced in plasma physics to describe the damping of plasma oscillations [11]. For high beam intensities, the incoherent spread is modified by the wakefields (see Chapter 2) and this effect leads to a loss of Landau damping. In this situation, the excitation from the wakefield is not damped anymore and coherent oscillations can grow exponentially, leading to a degradation of the beam parameters. Another example is the microwave instability, which is driven by wakefields with a wavelength much shorter than the bunch length. The microwave instability manifests as a fast emittance growth [12]. To mitigate the longitudinal instabilities in the SPS, another RF system composed of two TWC tuned at a frequency of 800 MHz is available. Its only use is to stabilise the beam through Landau damping by adding non-linearities to the RF bucket [13, 14]. However, the optimisation of the RF parameters of the 800 MHz RF system is not straightforward due to the complexity of the SPS impedance. In addition, the 800 MHz RF system has a limited effect on the microwave instability [15].

Even if the beam loading limitation in the SPS is solved after the RF upgrade, initial estimations of future limitations due to instabilities, based on scaling from the present situation showed that the HL-LHC requirements may still not be reachable [16, 17]. Therefore it is essential to identify the impedance sources responsible for the instabilities, in order to find a relevant cure (e.g. damping or shielding the impedance source). In addition, it is necessary to have an accurate SPS impedance model to be able to find means of optimisation of the operational cycles, and to do more precise predictions for future projects with the help of macroparticle simulations.

The SPS beam coupling impedance

One approach to develop the impedance model of a machine is to consider each element individually and evaluate the wakefields generated by a particle passing through this element (see Section 1.2.4 for wake potentials). The impedance of this device can be found using analytical calculations (e.g. [18, 19]), electromagnetic simulations (e.g. [20, 21, 22]), and from bench measurements (e.g. [23]). In practice, a combination of the three is usually required. The model described here and shown in Fig. I.3 is the present SPS impedance model [24]. It was developed over a long period of time in parallel with beam dynamics studies, with inputs from different groups at CERN (e.g. [25, 26], with regular updates presented in the LIU-SPS Beam Dynamics Working Group [27]). The typical bunch length range in the SPS is (1.5-3) ns, therefore the frequency range of the stable bunch spectrum is within 1 GHz. The frequency range of interest for the impedance in calculations was taken up to (3-5) GHz, to account for the effect of high frequency impedance sources on the beam. There are three main groups of longitudinal impedance sources relevant to the studies presented in this thesis: the Travelling Wave Cavities, the injection and extraction kicker magnets and the vacuum flanges.

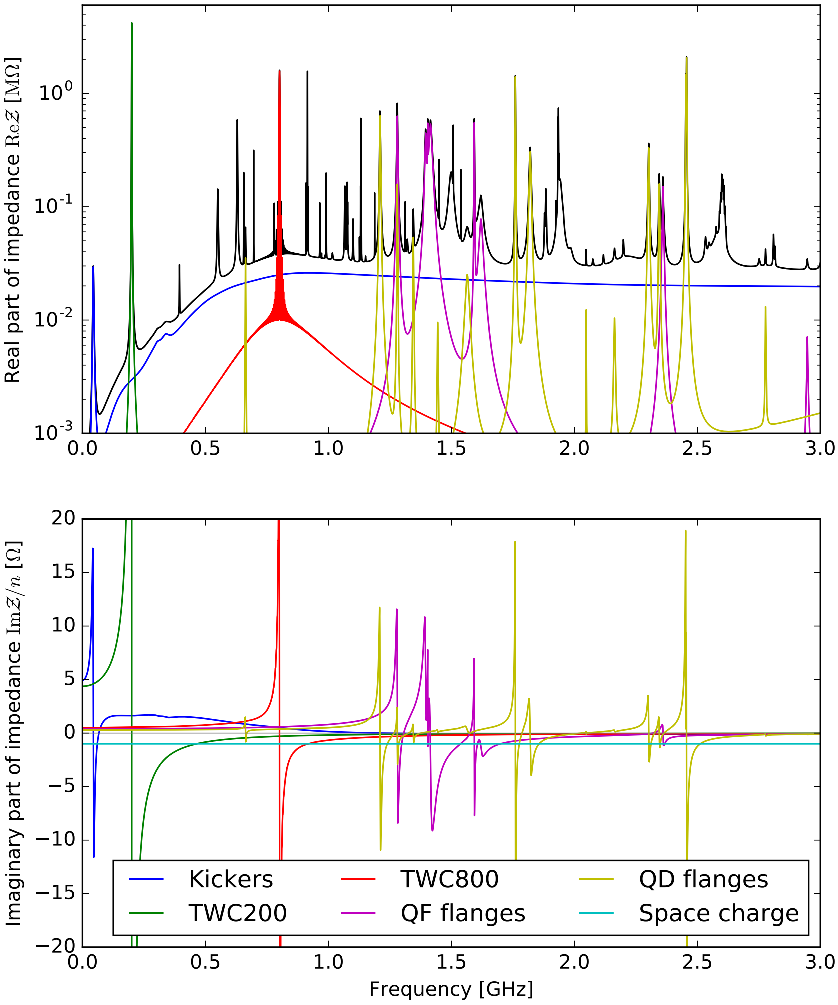

Figure I.3 – The present SPS impedance model up to 3 GHz [24]: resistive part (top) and reactive part (bottom). The most relevant groups of impedance for the studies presented in this thesis are shown in different colours, while the full SPS impedance is shown in black (only for the resistive part, for clarity purpose).

The impedance of the TWC at 200 MHz and 800 MHz is responsible for the beam loading effects mentioned above. An evaluation of their impedances was done in [9, 28, 29]. In addition to the main harmonic, several High Order Modes (HOM) present in the TWC have large impedance. For the 200 MHz TWC, the most significant HOM is located at a frequency of 629 MHz, and is damped by HOM couplers. Other HOMs were also identified at higher frequencies (915 MHz and 1.13 GHz). Concerning the 800 MHz, an HOM exists at a frequency around 1.9 GHz [30].

The kicker magnets, used for the injection and extraction of the beam, are the most important contributions in terms of broadband impedance [31]. While the impedance sources can have

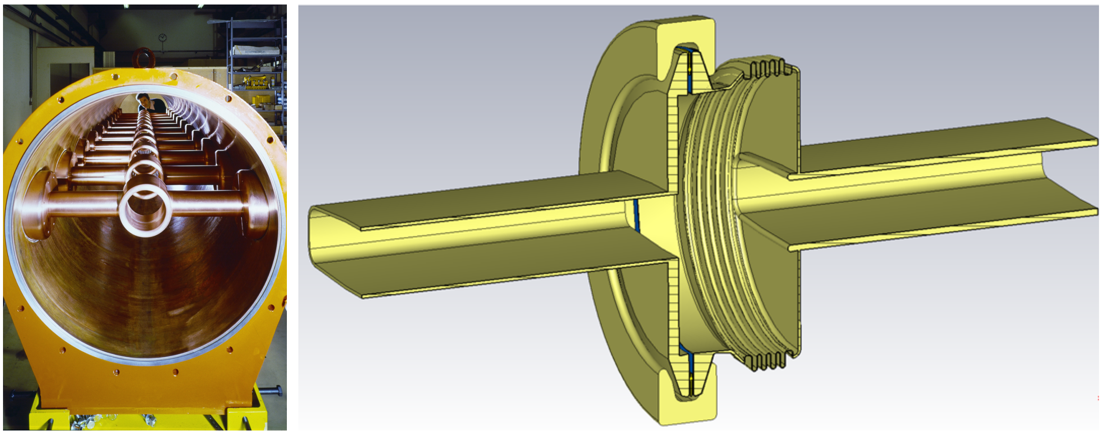
(a) TWC 200 MHz
(b) MBA-MBA vacuum flanges

Figure I.4 – Example of impedance sources in the SPS: (a) The 200 MHz SPS Travelling Wave Cavity (inside one section, © CERN), (b) The vacuum flange between two MBA type bending magnets modelled in the CST Microwave Studio software [22].

a detrimental effect on the beam, one should also take into account that the beam can damage the devices via RF heating, which is a critical effect for the kickers. Therefore, the impedance of all extraction kickers (MKE) was reduced by serigraphy [32], which is responsible for the resonance at 44 MHz visible in Fig. I.3.

The role of the vacuum flanges is to connect the beam pipes along the ring. In the SPS, many types of vacuum chambers are used along the ring and also depend on the type of the neighbouring magnets. An example of vacuum flange between two MBA-type bending magnets is shown in Fig. I.4b. Due to the large number of these cavity-like structures in the ring, these vacuum flanges are the biggest source of resonant impedances at high frequency (above 1 GHz) in the SPS [33]. The different types of vacuum chambers can be classified in two main groups depending on their connecting beam pipe: the QF-type vacuum flanges for those close to focusing magnets (QF), and the QD-type vacuum flanges for those close to defocusing magnets (QD).

Other impedance contributions are also included in the SPS model: the resistive wall impedance (which depends on the conductivity of the beam pipe material [31]), the Beam Position Monitors (BPM) [34], the vacuum pumping ports [35], the Y-chambers (used to switch between two beam pipes at certain locations in the ring to put a device in and out of the ring), the tanks of the beam scrapers used to clean beam tails or halos before extraction to the LHC [27, 36].

The longitudinal space charge effect can also be modelled by an impedance, and more precisely by a constant reactive impedance $\mathrm{Im}\mathcal{Z}/n$ ($n = f/f_{\mathrm{rev}}$ with f the frequency and f_{rev} the revolution frequency). It is shown to be an important contribution in the study of the synchrotron frequency shift with intensity in Chapter 2. Therefore, the longitudinal space charge impedance was accurately evaluated and added to the SPS impedance model (see

Chapter 3) [37].

Beam measurements of the impedance

Thanks to the progress in computing tools, very detailed evaluations of the impedance sources can be done. Nevertheless, all the particularities of the impedance sources may not be taken into account (e.g. the material properties as a function of the frequency). In addition, the actual implementation of a device in the machine may be different from the ideal case in simulations or in the lab because of fabrication errors, installation constraints, or beam induced damage while operating the accelerator.

Measurements of the impedance with the beam are necessary to verify the existing impedance model. The beam characteristics are measured as a function of intensity and compared with analytical formulae or macroparticle simulations using the impedance model. Measurements using a stable beam can give information about the effective impedance corresponding to the product of the bunch spectrum with the impedance. The resistive part of the impedance $\mathrm{Re}\mathcal{Z}$ and the reactive part $\mathrm{Im}\mathcal{Z}$ have different effects on the beam, and various methods are possible to measure them separately. The impedance can also be probed using an unstable beam. In this case, the beam spectrum also includes specific information about the main impedance source driving the instability. A review of the methods is presented in Chapter 1, where the effect of induced voltage on synchrotron motion is described.

Beam measurements can serve several purposes. The first one is to keep track of the changes in the machine after the successive installation/removal of devices (e.g. reference measurements in the SPS [38]), or to verify the correct impedance reduction of a critical impedance source (e.g. impedance reduction of the SPS pumping ports in 2000 [39]). The second purpose is to identify contributions potentially missing from the model. An example is presented in Chapter 4 where measurements allowed to reveal a source of microwave instability as a resonant impedance at 1.4 GHz, which was identified subsequently to come from the vacuum flanges [40].

The goal of this thesis was to perform beam measurements of the longitudinal impedance to benchmark the existing model. The methods used were adapted and extended to take into account the complex impedance of the SPS (see Fig. I.3). Eventually, this allowed evaluation of the possible missing impedance and its dependence on frequency.

Thesis outline

This thesis is divided into six chapters, each contains the description of one study. Altogether, the order of the chapters corresponds to the approach used in the SPS to verify and improve the longitudinal impedance model using the beam as a source of information.

The first topic is the delimitation of the contours of this thesis. It is composed of the present introduction, together with Chapter 1. It consists of a description of the problem and the motivations for this research, as well as the theoretical background necessary for the studies. Some elements in the design of the simulation code BLonD are presented together with the main equations for longitudinal beam dynamics. This code was used for all the macroparticle simulations presented in this thesis.

The main research work is presented in Chapters 2 to 5. In Chapter 2, the reactive part of the SPS impedance is evaluated from the measurements of the synchrotron frequency shift with intensity. This method was extended to scan the shift with bunch length, which allowed to identify missing impedance in the model, together with its possible dependence on frequency. This study also showed that the longitudinal space charge should not be neglected at low energy in the SPS. Consequently, the longitudinal space charge impedance was evaluated in detail and is presented in Chapter 3.

In Chapter 4, the high frequency impedance sources were probed by measuring the modulation of the profiles of long bunches, injected into the ring with the RF voltage switched off. This modulation, driven by microwave-like instabilities, allowed the main impedance sources responsible for microwave instabilities to be identified.

Another way to evaluate the accuracy of the impedance model is to test the ability to reproduce the measured instabilities in macroparticle simulations. Unlike the measurements presented in the previous chapters, which give a more specific information, the comparison of measured instabilities and simulations gives an evaluation of the accuracy of the impedance model as a whole. Studies done with a single proton bunch for various RF configurations (different RF programs, in single and double RF operation) are described in Section 5.2, and with a single ion bunch in Section 5.3.

The work presented in this thesis showed that simulations can reproduce reasonably all the aforementioned measurements using the present impedance model. Chapter 6 shows applications of the impedance model to explore the beam parameters achievable for the HL-LHC project, taking into account the LIU-baseline scenario of the SPS RF upgrade and impedance reduction.

Finally, a conclusion is given to summarise the achievements of this PhD thesis.

1 Synchrotron motion with intensity effects

1.1 Introduction

In this chapter the theoretical basis necessary for the thesis is reviewed, with input taken from [18, 19, 41, 42, 43]. The equations of motion were adapted to their use in the macroparticle tracking code BLonD (Beam Longitudinal Dynamics [44]), which was developed in collaboration with other members of the BE/RF group at CERN. The motivation for the development of this code was the need for an efficient and modular simulation tool to study complex problems (e.g. multi-bunch instabilities), in all the synchrotrons of the CERN accelerator complex. BLonD was designed to simulate the synchrotron motion with intensity effects, and the equations of motions were adapted to be able to simulate the various low-level RF (LLRF) systems used in operation. The code is written in Python, with optimisations in C++ for the most time demanding operations. It was benchmarked against theoretical calculations [45] and against beam measurements. It was also benchmarked against other simulation codes: ESME [46], HEADTAIL [47] and PyORBIT [48, 49].

Below, the equations of motion are presented to show the effect of the induced voltage on the synchrotron motion, for stationary and unstable bunches. First, the notion of effective impedance is introduced to show what is the effect of the resistive and reactive part of the impedance on the beam. Then, the notion of potential well distortion is introduced followed by the basis to describe bunch oscillations and instabilities. Finally, a review of the methods to measure the machine impedance with the beam is given, to introduce the methods used in the SPS and presented in this thesis.

1.2 Longitudinal equations of motion

1.2.1 Synchronism condition in synchrotrons

In this thesis, the longitudinal beam dynamics in synchrotrons is considered. A synchrotron is a circular accelerator, in which the beam trajectory is modified using magnetic fields, and the beam accelerated using electric fields. The force exerted on a charged particle is described by the Lorentz force:

$$\vec{F} = q\left(\vec{E} + \vec{v} \times \vec{B}\right), \tag{1.1}$$

where q is the charge of the particle, $\vec{E}$ is the electric field, $\vec{B}$ is the magnetic field and $\vec{v}$ is the particle velocity ($v = \beta c$ with c the speed of light).

To maintain the beam on the central orbit of the synchrotron, dipole magnets are distributed along the ring to bend the beam trajectory. All the bending magnets are considered identical, with a bending radius ρ and a vertical magnetic field with an amplitude B. The necessary magnetic field to keep particles with the momentum p on the designed orbit of the dipole magnets is defined by the magnetic rigidity:

$$B\rho = \frac{p}{q}. \tag{1.2}$$

During acceleration, the magnetic field B is increased and the maximum range in the magnetic field determines the momentum range of the synchrotron. Note that the bending magnets occupy a large fraction of the total ring (e.g. in the SPS $\approx 67\%$). So the total circumference of the ring is linked to the bending radius with:

$$C = 2\pi R = 2\pi\rho + L, \tag{1.3}$$

where R is the radius average of the whole accelerator and L is the length of the straight sections.

The revolution period of the reference particle travelling on the central orbit with a momentum p is:

$$T_\mathrm{rev} = \frac{1}{f_\mathrm{rev}} = \frac{C}{\beta c}, \tag{1.4}$$

where $f_\mathrm{rev} = \omega_\mathrm{rev}/\left(2\pi\right)$ is the corresponding angular revolution frequency.

The particle is accelerated in an RF cavity where the longitudinal electric field is oscillating with the RF frequency $f_\mathrm{RF} = \omega_\mathrm{RF}/\left(2\pi\right)$. In the stationary case, the reference (or synchronous) particle is synchronised with the RF cavity and arrives each turn at the same RF phase. The synchronism condition is:

$$\omega_\mathrm{RF} = h\,\omega_\mathrm{rev}, \tag{1.5}$$

where h is the RF harmonic and an integer number. During acceleration, the revolution frequency of the synchronous particle changes with β and the RF frequency should be adjusted accordingly. The cavity bandwidth in the RF frequency also determines the range of achievable momenta in the machine, since normally it needs to cover the swing of the revolution frequency during the acceleration for a given h.

To derive the longitudinal equations of motion for an arbitrary particle, the reference coordinate in the longitudinal plane is set with respect to the designed energy and revolution period, noted with the subscript d. Note that the difference between the notion of design and synchronous particle is discussed in Section 1.2.5. For numerical computations, the equations are discretised as a function of the number of turns k. The design energy is defined as E_d^k, and corresponds to the energy of the particle on the central orbit of the synchrotron and for the magnetic field at a given turn B_d^k (see Eq. (1.2)). The energy of an arbitrary particle with respect to this reference is noted:

$$\Delta E^k = E^k - E_d^k. \tag{1.6}$$

An external reference clock is introduced and defined as:

$$t_{\mathrm{ref}}^k = \sum_{i=1}^{k} T_{\mathrm{rev},d}^i \tag{1.7}$$

where i is an iteration index corresponding to a number of turns in the synchrotron and k is the present turn. The revolution period at each turn $T_{\mathrm{rev},d}^i$ is obtained from the corresponding energy E_d^i. The arrival time of an arbitrary particle into the RF cavity with respect to the reference time at that turn is defined as:

$$\tau^k = t^k - t_{\mathrm{ref}}^k. \tag{1.8}$$

The equations of motion of a particle in the coordinate system $(\tau, \Delta E)^k$ are presented below.

1.2.2 Energy gain in the RF cavity

For a single passage through the RF cavity gap with the length l_{cav}, the energy gained by the particle is:

$$\delta E(\tau) = q \int_0^{l_{\mathrm{cav}}} \mathcal{E}_0 \sin\left(\omega_{\mathrm{RF}}\tau + \frac{\omega_{\mathrm{RF}}}{\beta c} s\right) ds \tag{1.9}$$

where $\mathcal{E}_0$ is the amplitude of the electric field, assumed constant in the RF gap. For a symmetric gap, the Eq. (1.9) can be written in the form:

$$\delta E(\tau) = q V_{\mathrm{RF}} \sin\left[\phi_{\mathrm{RF}}(\tau)\right], \tag{1.10}$$

where V_{RF} is the amplitude of the RF voltage and $\phi_{\mathrm{RF}}(\tau)$ is the RF phase at the time of the particle arrival τ. The RF voltage is defined as:

$$V_{\mathrm{RF}} = \mathcal{E}_0 l_{\mathrm{cav}} T, \tag{1.11}$$

where T is the transit time factor which takes into account that the particle passes in the RF cavity in a certain amount of time and sees a varying electric field ($T < 1$).

The RF phase at the particle arrival is:

$$\phi_{\mathrm{RF}}\left(\tau^{k}\right) = \left(\sum_{i=1}^{k} \omega_{\mathrm{RF}}^{i} T_{\mathrm{rev},d}^{i}\right) + \omega_{\mathrm{RF}}^{k} \tau^{k} + \phi_{\mathrm{off}}^{k}, \tag{1.12}$$

where ϕ_{off}^{k} is an arbitrary phase offset that can be used in simulations for adjustments. In the general case, the RF frequency is synchronous with the design revolution period. Therefore, the sum in Eq. (1.12) in this case is a multiple of 2π. The form (1.12) was introduced to be able to simulate the RF manipulations and the LLRF feedback loops, which can change the RF frequency and introduce a change in the RF phase at the next turn with respect to the reference clock t_{ref}^{k} (e.g. radial steering, the phase loop, etc.).

Multiples of 2π are subtracted to keep small the values of RF phase, which is more convenient for numerical evaluation of the sinus function:

$$\phi_{\mathrm{RF}}\left(\tau^{k}\right) = \left(\sum_{i=1}^{k} \frac{\omega_{\mathrm{RF}}^{i} - h^{i} \omega_{\mathrm{rev},d}^{i}}{h^{i} \omega_{\mathrm{rev},d}^{i}} 2\pi h^{i}\right) + \omega_{\mathrm{RF}}^{k} \tau^{k} + \phi_{\mathrm{off}}^{k}. \tag{1.13}$$

The particle passes once every turn in the cavity, therefore $\delta E = E^{k+1} - E^{k}$, which gives by summing over the N_{RF} systems available in the ring (the RF systems can be assumed to be at the same location if the revolution period is small compared to the synchrotron period, see below):

$$E^{k+1} = E^{k} + q \sum_{l=1}^{N_{\mathrm{RF}}} V_{\mathrm{RF,l}}^{k} \sin\left[\phi_{\mathrm{RF,l}}\left(\tau^{k}\right)\right]. \tag{1.14}$$

The Eq. (1.14) can be expressed in terms of relative energy, with respect to the design energy E_{d}^{k}. By subtracting E_{d}^{k+1} on both sides:

$$\Delta E^{k+1} = \Delta E^{k} + q \sum_{l=1}^{N_{\mathrm{RF}}} V_{\mathrm{RF,l}}^{k} \sin\left[\phi_{\mathrm{RF,l}}\left(\tau^{k}\right)\right] - \left(E_{d}^{k+1} - E_{d}^{k}\right), \tag{1.15}$$

where $\delta E_{\mathrm{acc},d}^{k\rightarrow k+1} = \left(E_{d}^{k+1} - E_{d}^{k}\right)$ is the increment in energy of the beam during acceleration (or deceleration).

The numerical equations (1.13) and (1.15) are the ones used for macroparticle tracking in BLonD.

1.2.3 Slippage in arrival time to the RF cavity

A particle with a small deviation in momentum Δp with respect to the reference momentum p_d has a different bending radius in the dipole magnets $\Delta\rho$, and therefore a different orbit radius ΔR in the synchrotron (see Eq. (1.2) and (1.3)). This effect is called the dispersion and is represented in transverse beam dynamics with the function $D_x(s)$ along the ring. The relationship between Δp and ΔR is obtained by integrating the dispersive function over one turn in the synchrotron and it is defined as the momentum compaction factor:

$$\alpha = \frac{1}{C}\oint \frac{D_x(s)}{\rho(s)} ds = \frac{\Delta R / R_d}{\Delta p / p_d}. \tag{1.16}$$

Therefore, depending on the particle relative momentum $\delta = \Delta p / p_d = \Delta E / \left(\beta_d^2 E_d\right)$, it will arrive in the RF cavity at the next turn at the time (in absolute):

$$t^{k+1} = t^k + T_{\mathrm{rev}}^{k+1} = t^k + \frac{2\pi}{\omega_{\mathrm{rev}}^{k+1}}. \tag{1.17}$$

The index $(k+1)$ in the revolution period of the particle comes from the fact that the energy gain in the RF cavity is applied first. Therefore, the new reference energy is E_d^{k+1}. The expression of Eq. (1.17) in terms of relative time τ is obtained by subtracting with the reference time t_{ref}^{k+1} on both sides:

$$\tau^{k+1} = \tau^k + \frac{2\pi}{\omega_{\mathrm{rev}}^{k+1}} - \frac{2\pi}{\omega_{\mathrm{rev},d}^{k+1}} \tag{1.18}$$

The relationship between the revolution frequency ω_{rev} of an arbitrary particle and the design one $\omega_{\mathrm{rev},d}$, can be obtained by combining Eqs. (1.4) and (1.16). It is defined as the slippage factor:

$$\eta_d = -\frac{\Delta\omega_{\mathrm{rev}} / \omega_{\mathrm{rev},d}}{\Delta p / p_d}, \tag{1.19}$$

which is related to the momentum compaction factor as:

$$\eta_d = \alpha - \frac{1}{\gamma_d^2} = \frac{1}{\gamma_t^2} - \frac{1}{\gamma_d^2}. \tag{1.20}$$

$\gamma_t = 1/\sqrt{\alpha}$ is the transition Lorentz factor. Two regimes can be distinguished, depending on the transition energy γ_t (which is constant for a given optics parameters), and the beam energy γ_d (which changes during acceleration). Below transition energy ($\gamma_d < \gamma_t$ and $\eta < 0$), particles with $\Delta p > 0$ makes one turn faster than the designed value and vice-versa above transition energy. In some cases, the transition is crossed during the acceleration ramp (e.g. ion cycle in the SPS).

Finally, the numerical equation of motion for the slippage in the time of arrival of the particles in the RF cavity is:

$$\tau^{k+1} = \tau^k + \frac{\eta_d^{k+1} T_{\mathrm{rev},d}^{k+1}}{\left(\beta_d^{k+1}\right)^2 E_d^{k+1}} \Delta E^{k+1}. \tag{1.21}$$

Note that the slippage factor (and the momentum compaction factor) can be a non-linear function of δ (the relationship between the various orders of η and α is given in [41]):

$$\eta\left(\delta\right) = \eta_0 + \eta_1 \delta + \eta_2 \delta^2 + \mathcal{O}\left(\delta^3\right). \tag{1.22}$$

Consequently, taking into account the non linear slippage factor the Eq. (1.21) can be written as:

$$\tau^{k+1} = \tau^k + T_{\mathrm{rev},d}^{k+1} \left(\frac{1}{1-\eta_d\left(\delta^{k+1}\right)\delta^{k+1}} - 1 \right). \tag{1.23}$$

Both Eq. (1.21) and (1.23) are included in BLonD for the most general case, only the linear slippage factor $\eta = \eta_0$ is considered below, and this assumption will be used for the rest of the thesis.

1.2.4 Induced voltage

To compute the effect on the beam of the various impedance sources described in the Introduction, let us first consider two particles: a source particle inducing an electric field $\mathcal{E}_{\mathrm{ind}}\left(s,t\right)$ into a cavity-like structure, and a witness particle which gets an energy loss (or gain) from the induced electric field. Particles are assumed not to have a transverse position offset and are aligned onto the longitudinal axis at a time distance τ (both particles are assumed to have the same velocity). In this configuration, the energy loss/gain for the witness particle is:

$$\delta E_{\mathrm{ind}}\left(\tau\right) = q \int_0^{l_{\mathrm{ind}}} \mathcal{E}_{\mathrm{ind}}\left(s, t=\frac{s}{\beta c}-\tau\right) ds = -q^2 \mathcal{W}\left(\tau\right), \tag{1.24}$$

where the induced electric field is integrated over the length l_{ind} of the cavity-like element and $\mathcal{W}\left(\tau\right)$ is the wake function per unit of charge defined as:

$$\mathcal{W}\left(\tau\right) = -\frac{1}{q} \int_0^{l_{\mathrm{ind}}} \mathcal{E}_{\mathrm{ind}}\left(s, t=\frac{s}{\beta c}-\tau\right) ds. \tag{1.25}$$

Let us now consider a bunch composed of N_b particles. The line density of the bunch in the longitudinal plane is noted $\lambda\left(\tau\right)$ and is normalised as:

$$\int_{-\infty}^{\infty} \lambda\left(\tau\right) d\tau = 1. \tag{1.26}$$

The total voltage induced by the bunch (or wake potential) corresponds to the convolution of the wake function with the bunch line density and can be calculated as:

$$V_{\mathrm{ind}}(\tau) = -qN_b \int_{-\infty}^{\infty} \lambda\left(\tau'\right) \mathcal{W}\left(\tau - \tau'\right) d\tau'. \tag{1.27}$$

The integral (1.27) can be also written in frequency domain as:

$$V_{\mathrm{ind}}(\tau) = -qN_b \int_{-\infty}^{\infty} \mathcal{S}(f)\, \mathcal{Z}(f)\, e^{j2\pi f\tau} df, \tag{1.28}$$

where the bunch spectrum $\mathcal{S}\left(f\right)$ is the Fourier transform of the line density:

$$\mathcal{S}\left(f\right) = \int_{-\infty}^{\infty} \lambda(\tau)\, e^{-j2\pi f\tau} d\tau. \tag{1.29}$$

The beam-coupling impedance $\mathcal{Z}\left(f\right)$ is defined as:

$$\mathcal{Z}\left(f\right) = \int_{-\infty}^{\infty} \mathcal{W}(\tau)\, e^{-j2\pi f\tau} d\tau. \tag{1.30}$$

Since the bunch passes through the impedance source every turn in the ring, the Eq. (1.28) can be rewritten as an expansion on the multiples of revolution harmonics with $n = f/f_{\mathrm{rev}}$ to take into account the periodicity of the ring:

$$V_{\mathrm{ind}}(\tau) = -qN_b f_{\mathrm{rev}} \sum_{n=-\infty}^{\infty} \mathcal{S}\left(nf_{\mathrm{rev}}\right) \mathcal{Z}\left(nf_{\mathrm{rev}}\right) e^{j2\pi n f_{\mathrm{rev}}\tau}. \tag{1.31}$$

Various models of impedance $\mathcal{Z}\left(f\right)$ can be used which are obtained using the methods described in the introduction. In many practical cases and by considering ultra relativistic particles ($\beta \approx 1$ in the SPS), a peak in the impedance can be described as a resonator by the following expression:

$$\mathcal{Z}\left(f\right) = \frac{R_s}{1 + jQ\left(\frac{f}{f_r} - \frac{f_r}{f}\right)}, \tag{1.32}$$

where R_s is the shunt impedance, Q is the quality factor and $f_r = \omega_r/(2\pi)$ is the resonant frequency. The corresponding wake function is:

$$\mathcal{W}(\tau) = \begin{cases} \alpha R_s & \text{for } \tau = 0, \\ 2\alpha R_s e^{-\alpha\tau}\left[\cos(\bar{\omega}\tau) - \frac{\alpha}{\bar{\omega}}\sin(\bar{\omega}\tau)\right] & \text{for } \tau > 0, \end{cases} \tag{1.33}$$

where $\alpha = \pi f_r/Q$ and $\bar{\omega} = \sqrt{\omega_r^2 - \alpha^2}$. The decay time of the wake function for a given resonant frequency f_r is given by the quality factor Q, which also determines the frequency bandwidth of the impedance ($\Delta\omega_r = \omega_r/(2Q)$). Depending on Q, impedance sources can be separated into two kinds: the broad-band impedance sources (small Q), for which the bandwidth of the impedance is larger than the bunch spectrum width ($\sim 1/\tau_L$ where τ_L is the bunch length) and the induced voltage affects only a single bunch, and the narrow-band impedance sources (large Q) which can affect several bunches.

For the Travelling Wave Cavities in the SPS, the impedance can be expressed as [9]:

$$\begin{aligned}\mathcal{Z}(f) = 4R_s \Bigg\{ & \left[\frac{\sin\frac{t_{\text{fill}}(f-f_r)}{2}}{\frac{t_{\text{fill}}(f-f_r)}{2}}\right]^2 - j\frac{t_{\text{fill}}(f-f_r) - \sin t_{\text{fill}}(f-f_r)}{2t_{\text{fill}}^2 (f-f_r)^2} \\ & + \left[\frac{\sin\frac{t_{\text{fill}}(f+f_r)}{2}}{\frac{t_{\text{fill}}(f+f_r)}{2}}\right]^2 - j\frac{t_{\text{fill}}(f+f_r) - \sin t_{\text{fill}}(f+f_r)}{2t_{\text{fill}}^2 (f+f_r)^2}\Bigg\},\end{aligned} \tag{1.34}$$

and the corresponding wake function is:

$$\mathcal{W}(\tau) = \begin{cases} \frac{2R_s}{\tilde{t}_{\text{fill}}} & \text{for } \tau = 0, \\ \frac{4R_s}{\tilde{t}_{\text{fill}}}\left(1 - \frac{\tau}{\tilde{t}_{\text{fill}}}\right)\cos\omega_r\tau & \text{for } 0 < \tau < \tilde{t}_{\text{fill}}, \\ 0 & \text{for } \tau \geq \tilde{t}_{\text{fill}}, \end{cases} \tag{1.35}$$

where $t_{\text{fill}} = 2\pi\tilde{t}_{\text{fill}} = l_{\text{cav}}/v_g$ is the filling time of the cavity (of length l_{cav} and where the travelling wave propagates with the group velocity $v_g = 0.0946c$) which gives the decay time of the wake function (comparable to $1/\alpha$ for a resonator). The length of the TWC depends on the number of sections (2x4 sections and 2x5 sections presently). Each section is composed of 11 cells, the length of each cell is 374 mm. The impedance of the TWC is given by $R_s = R_2 l_{\text{cav}}^2/8$, where the series impedance $R_2 = 27.1\ \text{k}\Omega/\text{m}^2$. The parameters for the present SPS TWC used in BLonD simulations are given in [24]. An RF upgrade is planned in the SPS [10], consisting in an increase of the number of TWC and reducing their sizes (4x3 sections and 2x4 sections). Since the impedance for one single TWC scales as $R_s \propto l_{\text{cav}}^2$, while the sum of the impedance of all the TWC is linear, this allows more TWC (and more RF voltage together with the power upgrade), with a lower total impedance (less beam loading).

Other electromagnetic interactions between the particles within a bunch, which are not driven by cavity-like structures, can also be modelled by an impedance. This is the case of the resistive-wall impedance [31], and the space charge which is discussed in detailed in Chapter 3.

Finally, the energy loss/gain for a particle due to the induced voltage of a bunch is given by:

$$\delta E_{\text{ind}}(\tau) = qV_{\text{ind}}(\tau), \tag{1.36}$$

and the corresponding numerical equation of motion is:

$$\Delta E^{k+1} = \Delta E^k - q^2 \frac{N_b^k}{N_{\text{macro}}} \sum_{l'=1}^{N_{\text{res}}} \left(\lambda^k * \mathcal{W}_{l'}\right)\left(\tau^k\right) \tag{1.37}$$

where the sign $*$ represents the numerical convolution for all the N_{res} resonant modes coming from the various impedance sources for one passage in the ring (assuming λ^k does not change over one turn). The convolution can either be done in time domain or in frequency domain using Fast Fourier Transforms. The bunch profile λ^k corresponds to the histogram in the τ dimension of the macroparticle distribution, composed of a total number of macroparticle N_{macro} and that is updated every turn. The resolution of the numerical bunch profile λ^k in simulations gives the frequency range of the impedance that will be used in simulations. Therefore, a careful selection of these parameters and the choice of doing calculations in time or frequency domain depends on the impedance source [50]. Note that the bunch intensity can change due to particle losses and therefore it also depends on the time (~ turn k). In some accelerators, the induced voltage may not be decaying over one turn and the contribution of the previous turns should also be included in Eq. (1.37). In the SPS, the multi-turn effects are considered to be negligible.

1.2.5 Single particle motion

The synchrotron motion is defined as the motion of particles in the coordinates $(\tau, \Delta E)$. To describe the synchrotron motion with intensity effects, the discrete equations of motion (1.15), (1.21) and (1.37) are expressed in a continuous time (with the differential time step $dt = T_{\text{rev}}$). The conditions are that the changes in the machine parameters (reference energy, RF voltage, etc.) are slow in comparison to the synchrotron motion (adiabaticity condition, see below). In this section, as a simplification, only a single RF system is considered. In addition the bunch is assumed to be stationary (or steady state bunch), with the line density $\lambda(\tau)$ and the induced voltage $V_{\text{ind}}(\tau)$ which are also stationary. In these conditions the continuous longitudinal equations of motion are:

$$\dot{\Delta E} = -\frac{\partial \mathcal{H}}{\partial \tau} = \frac{q}{T_{\text{rev}}} V_{\text{RF}} \sin(\omega_{\text{RF}}\tau) - \frac{\delta E_{\text{acc}}}{T_{\text{rev}}} + \frac{q}{T_{\text{rev}}} V_{\text{ind}}(\tau), \tag{1.38}$$

$$\dot{\tau} = \frac{\partial \mathcal{H}}{\partial (\Delta E)} = \frac{\eta}{\beta^2 E} \Delta E, \tag{1.39}$$

where the over-dot represents a derivative in time t and $\mathcal{H}$ is the Hamiltonian (see 1.2.6). Eqs. (1.38) and (1.39) can be combined to obtain the differential equation describing the evolution in time of the particle coordinate τ:

$$\ddot{\tau} - \frac{\eta}{\beta^2 E T_{\text{rev}}} \left[q V_{\text{RF}} \sin(\omega_{\text{RF}}\tau) + q V_{\text{ind}}(\tau) - \delta E_{\text{acc}} \right] = 0, \tag{1.40}$$

The synchronous particle is defined as the particle which gets the energy increment δE_{acc} every turn and therefore its deviation in energy with time is $\dot{\Delta E} = 0$. The stable motion of a particle in the phase space $(\tau, \Delta E)$ consists of periodic synchrotron oscillations around the stable point with coordinates $(\tau = \tau_s, \Delta E = 0)$ where τ_s is obtained from $\dot{\Delta E} = 0$. The Eq. (1.40) can be simplified by considering only particles with small amplitudes of synchrotron oscillation with linear RF force and ignoring intensity effects:

$$\ddot{\tau} + \omega_{s0}^2 \tau = 0. \tag{1.41}$$

This equation has the solution:

$$\tau(t) = \hat{\tau} \cos(\omega_{s0} t) + \tau_s. \tag{1.42}$$

The linear synchrotron frequency $f_{s0} = \omega_{s0}/(2\pi)$ from Eq. (1.41) is defined as:

$$f_{s0} = \frac{1}{2\pi} \sqrt{\frac{-\eta q V_{\mathrm{RF}} \omega_{\mathrm{RF}} \cos\phi_s}{\beta^2 E T_{\mathrm{rev}}}}. \tag{1.43}$$

From Eq. (1.43), since the slippage factor η can be positive or negative (for operation above or below the transition energy), the stability condition is given by $-\eta \cos\phi_s > 0$ which imposes the following ranges for ϕ_s:

$$\phi_s = \begin{cases} \arcsin\left(\frac{\delta E_{\mathrm{acc}}}{q V_{\mathrm{RF}}}\right) & \text{and} \in \left[-\frac{\pi}{2}, \frac{\pi}{2}\right] \text{ below transition energy,} \\ \pi - \arcsin\left(\frac{\delta E_{\mathrm{acc}}}{q V_{\mathrm{RF}}}\right) & \text{and} \in \left[\frac{\pi}{2}, \frac{3\pi}{2}\right] \text{ above transition energy.} \end{cases} \tag{1.44}$$

The synchronous particle was defined here assuming a constant (or slowly varying) energy increment δE_{acc}. The corresponding definition for the discrete equations of motion described previously is the particle getting the energy increment $\delta E_{\mathrm{acc},d}^{k\to k+1}$ for any turn k. During RF manipulations or by including intensity effects (see Section 1.3), the position of the point fulfilling the definition of the synchronous particle can move in phase space. It was found more convenient to use the reference defined by the machine parameters without RF manipulations and intensity effects shown in Section 1.2.1. Moreover, if the energy increment changes from one turn to the other, a given macroparticle cannot fulfil the conditions to remain synchronous on two consecutive turns. Therefore, the notion of design parameters with the subscript d was introduced to prevent from any ambiguity.

1.2.6 Hamiltonian of the synchrotron motion

In the general case, if the non-linearities of the RF voltage are not ignored, the synchrotron frequency depends on the particle amplitude $\hat{\tau}$. In addition, the induced voltage also adds non-linearities which depend on the impedance sources in the machine. A more general approach consists in describing the synchrotron motion using the Hamiltonian formalism. By combining Eqs. (1.38) and (1.39):

$$\mathcal{H}(\tau,\Delta E)=\frac{\eta}{2\beta^2 E}\Delta E^2+\overbrace{\underbrace{\frac{q}{T_\text{rev}}\int V_\text{RF}(\tau)\,d\tau-\frac{\delta E_\text{acc}}{T_\text{rev}}}_{\mathcal{U}_\text{RF}(\tau)}+\underbrace{\frac{q}{T_\text{rev}}\int V_\text{ind}(\tau)\,d\tau}_{\mathcal{U}_\text{ind}(\tau)}}^{\mathcal{U}(\tau)}+C_\mathcal{H}, \tag{1.45}$$

where $\mathcal{U}(\tau)$ is the potential well, $\mathcal{U}_\text{RF}(\tau)$ is the RF potential well and $\mathcal{U}_\text{ind}(\tau)$ the induced-voltage potential well responsible for the potential well distortion. The integration constant $C_\mathcal{H}$ of the Hamiltonian is usually adjusted to have $\mathcal{H}(\tau=\tau_s,\Delta E=0)=0$. The synchronous time τ_s corresponds to the minimum of the potential well $\mathcal{U}(\tau)$, so that $\dot{\mathcal{U}}(\tau_s)=0$.

A particle performing oscillations in the longitudinal phase space $(\tau,\Delta E)$ with a maximum amplitude $\hat{\tau}$ follows a trajectory with a constant Hamiltonian $\widehat{\mathcal{H}}$. The area enclosed by the trajectory of this particle is defined as the particle emittance given by:

$$\varepsilon(\hat{\tau})=2\pi\mathcal{J}(\hat{\tau})=\sqrt{\frac{2\beta^2E}{\eta}}\oint\left[\widehat{\mathcal{H}}(\hat{\tau},0)-\mathcal{U}(\tau)\right]^{\frac{1}{2}}d\tau, \tag{1.46}$$

where the action coordinate $\mathcal{J}(\hat{\tau})$ was also introduced.

The Eq. (1.46) can also be used to compute the area enclosed by the particle with the largest amplitude of oscillation $\hat{\tau}$ for the particle to remain captured in the potential well. This area corresponds to the RF bucket area, which is given by:

$$\mathcal{A}_b=\sqrt{\frac{2\beta^2E}{\eta}}\oint\left[\widehat{\mathcal{H}}(\hat{\tau}_\text{UFP},0)-\mathcal{U}(\tau)\right]^{\frac{1}{2}}d\tau, \tag{1.47}$$

where UFP stands for the unstable fixed point which corresponds to the lowest maximum of the potential well. In a single RF system and without induced voltage, this equation leads to:

$$\mathcal{A}_b\underset{N_b=0}{\approx}8\sqrt{\frac{2\beta^2EqV_\text{RF}}{h^3\omega_\text{rev}^2|\eta|\pi}}\left(\frac{1-\sin\phi_s}{1+\sin\phi_s}\right). \tag{1.48}$$

A particle oscillating with an amplitude $\hat{\tau}$ performs a complete oscillation in one synchrotron period:

$$T_s^{(0)}(\hat{\tau})=\frac{1}{f_s^{(0)}(\hat{\tau})}=\sqrt{\frac{2\beta^2E}{\eta}}\oint\left[\widehat{\mathcal{H}}(\hat{\tau},0)-\mathcal{U}(\tau)\right]^{-\frac{1}{2}}d\tau, \tag{1.49}$$

which corresponds to the synchrotron frequency:

$$f_s^{(0)}(\hat{\tau})=f_{s0}\frac{\pi}{2K\left[\sin(\omega_\text{RF}\hat{\tau}/2)\right]}. \tag{1.50}$$

The synchrotron frequency can also be obtained by using the action coordinate together with

$$f_s^{(0)}\left(\widehat{\tau}\right) = \frac{1}{2\pi}\frac{d\mathcal{H}}{d\mathcal{J}}, \tag{1.51}$$

this definition is useful in semi-analytical evaluations of the synchrotron frequency.

Let us consider now a stationary bunch distribution in phase space $\psi_0\left(\tau, \Delta E\right)$, the corresponding bunch line density is given by:

$$\lambda_0\left(\tau\right) = \int_{-\infty}^{\infty} \psi_0\left(\tau, \Delta E\right) d\left(\Delta E\right). \tag{1.52}$$

Using the fact that a stationary bunch distribution (or matched distribution) is a function of the Hamiltonian: $\psi_0\left(\mathcal{H}\right)$, the bunch distribution can be retrieved from the line density using the Abel transform [51]:

$$\psi_0\left(\mathcal{H}\right) = -\frac{1}{\pi}\sqrt{\frac{\eta}{\beta^2 E}}\int_{\tau}^{\infty} \frac{d\lambda_0/d\tau}{\sqrt{\mathcal{U}\left(\tau\right) - \mathcal{H}}} d\tau. \tag{1.53}$$

This equation is particularly useful for particle simulations to generate an initial bunch distribution matched to the RF bucket with intensity effects, starting from a measured bunch profile.

The area in phase space occupied by the stationary bunch distribution ψ_0 is noted ε_L. In practice, the longitudinal emittance of the bunch is obtained using Eq. (1.46) with the particle oscillation amplitude replaced by $\widehat{\tau_L} = 2\sigma_{\mathrm{rms}}$, where σ_{rms} is the rms bunch length (which usually contains > 95% of the particles from the distribution). For a stable bunch in a conservative system, assuming that changes in the machines parameters are done adiabatically, the bunch emittance is an invariant (Liouville theorem).

The synchrotron period $T_{s0} = 2\pi/f_{s0}$ defines the typical time of the particle motion in longitudinal phase space. Changes in the machine parameters should be slow in comparison to the synchrotron period to be considered adiabatic, and preserve the longitudinal emittance ε_L, otherwise the longitudinal emittance increases (blow-up). This condition is given by:

$$\frac{1}{\omega_{s0}^2}\left|\frac{d\omega_{s0}}{dt}\right| \ll 1. \tag{1.54}$$

In most of the situations in the SPS covered in this thesis, this criterion is respected.

All equations presented in this section are modified due to potential well distortion in Eq. (1.45), which can be measured using various methods reviewed in Section 1.3.

1.2.7 Coherent bunch motion and instabilities

The evolution of the particle distribution as a whole can be described by the Vlasov equation, which in absence of intra-bunch collisions and damping mechanism has the form:

$$\frac{\partial \psi}{\partial t} + \frac{\eta}{\beta^2 E} \Delta E \frac{\partial \psi}{\partial \tau} + \left[\frac{q}{T_{\mathrm{rev}}} V_{\mathrm{RF}}(\tau) - \frac{\delta E_{\mathrm{acc}}}{T_{\mathrm{rev}}} + \frac{q}{T_{\mathrm{rev}}} V_{\mathrm{ind}}(\tau, N_b) \right] \frac{\partial \psi}{\partial \Delta E} = 0. \tag{1.55}$$

Here the left hand side of the equation corresponds to the total derivative in time of the particle distribution $d\psi/dt = 0$.

Using perturbation theory the particle distribution can be divided in two parts:

$$\psi(\tau, \Delta E, t) = \psi_0(\tau, \Delta E) + \psi_1(\tau, \Delta E)\, e^{-j\Omega t} \tag{1.56}$$

where $\psi_0(\tau, \Delta E)$ corresponds to the stationary distribution and $\psi_1(\tau, \Delta E)$ describes the perturbation which oscillates with frequency Ω. The growth rate of the perturbation is given by $\mathrm{Im}\Omega$. For $\mathrm{Im}\Omega = 0$ the bunch oscillations do not grow, however the coherent motion is still affected by both the induced voltage from the stationary bunch distribution and the one coming from the perturbation. Therefore, measurements of the impedance based on coherent oscillations require the evaluation of both effects. For $\mathrm{Im}\Omega > 0$ the perturbation grows as an instability. Depending on the mechanism of the instability the measurements of the growth rates and/or the instability thresholds in intensity N_{th} can also give some information about the impedance driving the instability.

1.3 Beam measurements of the impedance

Using the solution (1.42) the exponential function in Eq. (1.28) can be expanded (Jacobi-Anger expansion), up to the linear order in τ:

$$V_{\mathrm{ind}}(\tau) = -qN_b \left[\mathcal{Z}_0 + \tau \mathcal{Z}_1 + \mathcal{O}\left(\tau^2\right) \right], \tag{1.57}$$

where $\mathcal{Z}_0$ and $\mathcal{Z}_1$ are respectively the effective resistive and reactive impedances defined as:

$$\mathcal{Z}_0 = \int_{-\infty}^{\infty} \mathcal{S}(f)\, \mathcal{Z}(f)\, J_0\left(2\pi f \hat{\tau}\right) df \underset{\hat{\tau} \to 0}{\approx} \int_{-\infty}^{\infty} \mathcal{S}(f)\, \mathrm{Re}\mathcal{Z}(f)\, df, \tag{1.58}$$

$$\mathcal{Z}_1 = \int_{-\infty}^{\infty} \mathcal{S}(f)\, \mathcal{Z}(f)\, j \frac{J_1\left(2\pi f \hat{\tau}\right)}{\hat{\tau}/2} df \underset{\hat{\tau} \to 0}{\approx} -2\pi \int_{-\infty}^{\infty} \mathcal{S}(f)\, \mathrm{Im}\mathcal{Z}(f)\, f\, df, \tag{1.59}$$

and $J_n(x)$ is the Bessel function of the first kind.

Using the expansion (1.57), the Eq. (1.40) can be rewritten as:

$$\ddot{\tau} + \omega_{s0}^2 \tau \approx \frac{\omega_{s0}^2 q N_b}{V_{\mathrm{RF}} \omega_{\mathrm{RF}} \cos\phi_s} \left[\mathcal{Z}_0 + \tau \mathcal{Z}_1\right], \tag{1.60}$$

with the solution describing the synchrotron motion of particle with intensity effects included:

$$\tau(t) = \hat{\tau} \cos\left[\{\omega_{s0} + \Delta\omega_{s0}(N_b)\} t\right] + \{\tau_s + \Delta\tau_s(N_b)\}. \tag{1.61}$$

In this approximation, the synchronous shift in time $\Delta\tau_s(N_b)$ is defined by the effective resistive impedance $\mathcal{Z}_0$, while the synchrotron frequency shift $\Delta\omega_{s0}(N_b)$ is due to the effective reactive impedance $\mathcal{Z}_1$. Therefore, measuring the synchronous time and synchrotron frequency shifts with intensity allows information about the effective impedances $\mathcal{Z}_0$ and $\mathcal{Z}_1$ of the machine to be extracted.

1.3.1 Synchronous phase shift and energy loss

The interaction of the beam with the resistive impedance leads to an energy loss of the bunch. The bunch finds a new equilibrium position where the energy loss in the various impedance sources is compensated by the RF system as follows from Eq. (1.60). The time of arrival of the synchronous (and small oscillation amplitude) particle is shifted by:

$$\Delta\tau_s(N_b) = \frac{q N_b}{V_{\mathrm{RF}} \omega_{\mathrm{RF}} \cos\phi_s} \mathcal{Z}_0. \tag{1.62}$$

In beam measurements, the measured phase shift corresponds to the one of the bunch as a whole, which includes the contribution of all the particles in the bunch. The energy loss of the bunch is:

$$\delta E_b = -\left(N_b q\right)^2 k_{\parallel}, \tag{1.63}$$

where $k_{\parallel}$ is the loss factor defined as:

$$k_{\parallel} = \int_{-\infty}^{\infty} \left|\mathcal{S}(f)\right|^2 \mathrm{Re}\mathcal{Z}(f)\, df. \tag{1.64}$$

Then the shift in the time of arrival to the RF cavity of the bunch is:

$$\Delta\tau_b(N_b) = \frac{q N_b}{V_{\mathrm{RF}} \omega_{\mathrm{RF}} \cos\phi_s} k_{\parallel}. \tag{1.65}$$

The measurement of $\Delta\tau_b$ as a function of intensity gives the loss factor $k_{\parallel}$.

First measurements of the synchronous phase shift were performed in 1975 in the SPEAR-II accelerator at SLAC [52], by measuring the phase of the RF signal in the cavity and comparing it with the bunch phase measured from a pick-up electrode. With this method, the measured phase shift does not include the contribution from the RF system, but only from the sources of resistive impedance in the rest of the ring. Similar phase measurements were done recently in the LHC, and are presently used to evaluate the electron-cloud effect which is also responsible for energy loss of the proton beam and therefore its synchronous phase shift [53]. Another method consists of measuring the phase distance of two bunches in the ring: one bunch with a low intensity as a time reference, and a second bunch used to measure the synchronous phase shift as a function of intensity [54]. With this method, the contribution of the RF system is included in the phase shift. Similar measurements were done at CERN to evaluate the resistive impedance of the PS [55].

Concerning the SPS, measurements comparable to the ones in [52] were done in 2004 [56]. The difference was that instead of using the RF signal directly in the cavity, the measured signal was the one sent from the power amplifiers to the cavity (not including the beam-loading voltage component). Consequently the phase shift was mainly defined by the contributions from the main impedance of the TWC, and the extraction kickers MKE (note that this energy loss is also responsible for the kickers heating mentioned in the Introduction). Measurements were in good agreement with the expectations from theory, and were not reiterated in this thesis. Nevertheless, a by-product of the study done in Chapter 4 allowed to probe the resistive part of the SPS impedance, by measuring the drift rate of unstable bunches with RF off. The mechanism can also be described by the Eq. (1.63). A particularity of this method is that the main source of energy loss comes from the high frequency impedance sources, since the loss rate also depends on the overlap of the unstable bunch spectrum with the resistive part of the high frequency impedance sources driving the instability. Therefore, this method can be considered complementary to the previous measurements done in the SPS.

1.3.2 Synchrotron frequency shift

The effect of the reactive impedance is a change in the voltage amplitude seen by the bunch, leading to a shift in the synchrotron frequency. Assuming linear RF force and that in Eq. (1.61) the perturbation coming from $\mathcal{Z}_1$ is small, the synchrotron frequency shift can be written as:

$$\frac{\Delta\omega_{s0}}{\omega_{s0}}(N_b) \approx \frac{qN_b}{2V_{\mathrm{RF}}\omega_{\mathrm{RF}}\cos\phi_s}\mathcal{Z}_1. \tag{1.66}$$

The measurement of $\Delta\omega_{s0}/\omega_{s0}$ as a function of intensity gives the effective reactive impedance. Depending on the sign given by $\cos\phi_s$, below or above transition energy, the effect of $\mathcal{Z}_1$ is different. In the case of the SPS (above transition, $\cos\phi_s < 0$), and inductive impedance $\mathcal{Z}_1 > 0$ reduces the synchrotron frequency while a capacitive one $\mathcal{Z}_1 < 0$ increases it.

Several methods exist to measure the synchrotron frequency shift. For example, the finite number of particles in the bunch generates some noise in the beam current called the Schottky signal. Using the spectrum of the (traditional) Schottky signal, the synchrotron frequency shift with intensity can be evaluated from the distance between the synchrotron side-bands at multiples of f_s [57]. An example is the measurements of the synchrotron frequency shift in both rings of the the Relativistic Heavy Ion Collider [58, 59]. The synchrotron frequency shift can also be measured from the Peak-Detected (PD) Schottky signal [60], this method was used to measure the LHC reactive impedance [61]. Since the reactive impedance of the LHC is very small, the resolution of the measurements was not sufficient and other methods were applied. The LHC reactive impedance was probed using the excitation of the beam by monochromatic RF phase modulation, and the measurements of the loss of Landau damping instability threshold (see Section 1.3.4) [61]. Another method consists of measuring the Beam Transfer Function (BTF) [62], by applying an external white noise to the bunch and measuring the response. The measurements of the PS reactive impedance [63] were used in this thesis. Indeed, studies done at injection in the SPS rely on the knowledge of the bunch distribution extracted from the PS, which is modified by potential well distortion (see Section 1.3.3 on bunch lengthening below).

The study presented in Chapter 2 relies on measurements of bunch length (quadrupole) oscillations at injection, initiated by the mismatch of the bunch into the capture RF bucket. The frequency of these oscillations f_{s2} is approximately twice the linear synchrotron frequency and it depends on the reactive part of the impedance as well as the bunch intensity and length. Since 1999, this approach was used to monitor the evolution of the SPS impedance as many pieces of equipment were shielded, removed or installed [38]. In the measurements of the synchrotron frequency shift from quadrupole oscillations, the non-linearities of the RF bucket should also be taken into account. The dependence of the shift on the amplitude of particle oscillations and the bunch length is discussed in Chapter 2, together with the effect of the frequency structure of the SPS impedance. The quadrupole oscillation frequency is also shifted due to coherent motion of the bunch (see Section 1.2.7). The coherent synchrotron frequency shift was also evaluated for the SPS impedance. The particularity of the study presented in Chapter 2 is the exploitation of the non-linear dependence of the synchrotron frequency shift on bunch length, which helped to evaluate possible missing impedance (and its possible frequency dependence) from the deviations of measurements from simulations.

1.3.3 Bunch lengthening

The shape of particle trajectories as well as of the RF bucket is changing with the bunch intensity due to potential well distortion, and the particle distribution in phase space can be distorted. To describe the results of this perturbation the distinction should be made between the light and heavy particles. For light particles (leptons), the equilibrium energy spread is usually determined by the synchrotron radiation. The particle distribution converges to a Gaussian distribution in energy, and the bunch line density in the stable regime can be described by the Haïssinski equation [64].

Heavy particles (hadrons) are normally less affected by synchrotron radiation, and in the stable regime the emittance ε_L is invariant. The distortion of the particle distribution is mainly due to the effective reactive impedance $\mathcal{Z}_1$ and the bunch lengthening with intensity can be described by [65]:

$$\left(\frac{\tau_L}{\tau_{L0}}\right)^4 + \frac{12 N_b q \mathrm{Im}\mathcal{Z}/n}{\omega_{\mathrm{rev}}^2 V_{\mathrm{RF}} h \cos\phi_s \tau_{L0}^3}\left(\frac{\tau_L}{\tau_{L0}}\right) - 1 = 0. \tag{1.67}$$

In practice it is difficult to use the bunch lengthening as a function of intensity for proton bunches for the evaluation of the impedance, since the bunch emittance should be ensured to be the same regardless of the bunch intensity. There are many steps in the acceleration of a single bunch up to the SPS that can introduce some emittance blow-up (e.g. the injection mismatch of the bunch from the PSB to the PS, then to the PS into the SPS due to potential well distortion). Nevertheless, the measurements of bunch lengthening as a function of intensity are considered in Chapter 5.2, for various RF configurations in the SPS.

1.3.4 Instability threshold and growth rate

The characteristics of bunch instabilities can also be exploited to get information about the machine impedance. The measured instabilities can be reproduced in macroparticle simulations using the impedance model. The degree of agreement between simulations and measurements can help to evaluate the accuracy of the impedance model as a whole. In some particular cases, where the instability mechanism is well known, the instability threshold or the growth rate can give information about the effective impedance of the machine. For example, the threshold for the loss of Landau damping in the presence of reactive impedance is given by [66]:

$$\frac{\mathrm{Im}\mathcal{Z}}{n} < \frac{F|\eta|E}{q^2\beta^2}\frac{\tau_L}{N_b}\left(\frac{\Delta E}{E}\right)^2\left(\frac{\Delta\omega_s}{\omega_s}\right), \tag{1.68}$$

where F is a form factor depending on the bunch distribution, $\Delta E/E$ is the energy spread and $\Delta\omega_s/\omega_s$ is the synchrotron frequency spread in the bunch. This method was used in the LHC to evaluate its very small inductive impedance, which is very difficult to measure using other methods [61].

In this thesis, various approaches to evaluate the SPS impedance from instabilities were used. An example is the modulation by microwave instabilities of long bunches with RF off [67]. This method was applied to reveal the present most critical SPS impedance sources at high frequencies, using measurements of the growth rate and the amplitude of the instability and results are presented in Chapter 4. Chapter 5 is devoted to longitudinal beam instabilities in single and double RF systems. The instability thresholds with RF on were measured for both proton and ion bunches and results are compared with macroparticle simulations using the SPS impedance model.

1.4 Conclusions

In this Chapter, a review of the various methods to measure the machine impedance with the beam, based on the effect of potential well distortion and instabilities is presented. Many other methods exist but were not discussed here (e.g. localised impedance measurements in the ring). Although the longitudinal plane is the main focus of this thesis, similar methods are also used in the transverse plane. The SPS impedance model was developed using studies in both longitudinal and transverse planes. Important SPS results include the measurements of the betatron tune shifts (horizontal and vertical), head-tail and transverse mode coupling instabilities for different optics settings [68, 69, 70]. The identification of new impedance contributions, along with beam measurements of the impedance, allowed to converge in both cases to a good agreement between measurements and simulations. Only a selection of methods was used in the work described in this thesis. Nevertheless, the known methods were extended to extract maximum information about the SPS impedance.

2 Quadrupole frequency shift as a probe of the reactive impedance

2.1 Introduction

In this chapter, the reactive part of the SPS impedance is measured from the synchrotron frequency shift. The method presented below relies on the measurements of bunch length oscillations at injection, initiated by a mismatched RF voltage. The frequency of these oscillations f_{s2} is approximately twice the linear synchrotron frequency and depends on the reactive part of the impedance as well as on the bunch intensity and length. Since 1999, this approach was used to monitor the evolution of the SPS impedance as many pieces of equipment were shielded, removed or installed [38]. Examples of recent measurements performed using bunches with different parameters are shown in Fig. 2.1.

The synchrotron frequency depends on the voltage seen by the beam, which is modified due to the voltage induced by the impedance sources. For bunches performing coherent oscillations, the induced voltage contribution coming from the stationary part of the bunch distribution can be separated from the one coming from the mismatched part. The frequency of coherent oscillations can be presented in the following form [42]:

$$f_{s,m}\left(N_b\right) \approx m f_{s0} + m\Delta f_{\text{inc}}\left(N_b\right) + \Delta f_{\text{coh},m}\left(N_b\right), \tag{2.1}$$

where N_b is the bunch intensity (number of particles in the bunch ppb), m is the mode of the oscillations ($m = 1$ is dipole or bunch position oscillations, $m = 2$ is quadrupole or bunch length oscillations), f_{s0} is the synchrotron frequency for small amplitude of oscillations, Δf_{inc} is the incoherent frequency shift due to induced voltage from the stationary bunch distribution and $\Delta f_{\text{coh},m}$ the coherent frequency shift defined by the perturbation due to the mismatched part. For dipole oscillations, the coherent and the incoherent shifts are exactly compensating each other for a parabolic bunch [19] (which is a common distribution for proton bunches in the SPS), meaning that no information could be extracted. Therefore, quadrupole oscillations are measured since in this case the incoherent and coherent shifts are not compensating each other.

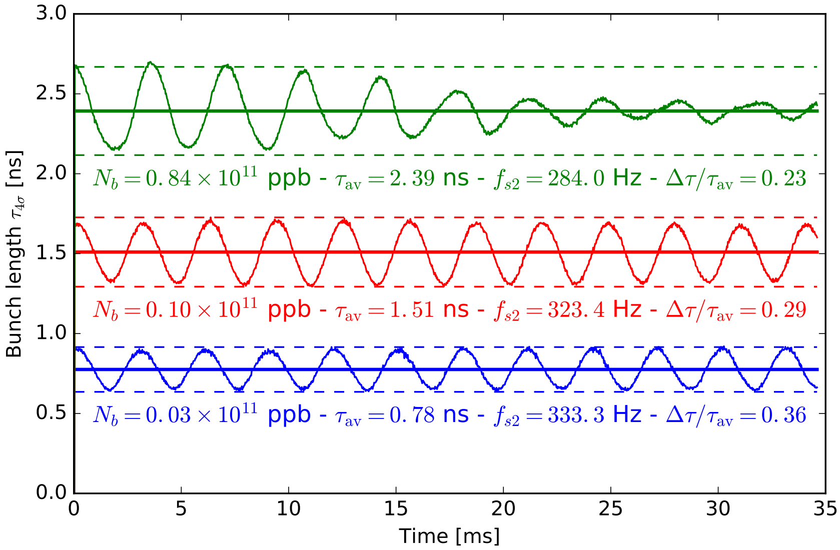

Figure 2.1 – Examples of bunch length oscillations at SPS injection measured in the Q26 optics for different average bunch lengths τ_{av} and intensities N_b.

So far, most of the impedance evaluations done by measuring the synchrotron frequency shift used the dependence of the quadrupole frequency on intensity. In this chapter, it is demonstrated that the dependence on bunch length should not be neglected and could even be used to extract additional information about the frequency characteristics of the impedance. First, the dependence of the synchrotron frequency shift on intensity and bunch length for quadrupole oscillations will be analysed. Following this, measurement methods and results obtained for the two different SPS optics are presented. Finally, measurements are compared with macroparticle simulations using the present SPS impedance model and deviations are exploited to estimate the remaining missing impedance.

2.2 Quadrupole synchrotron frequency shift

The bunch motion during quadrupole oscillations is shown in Fig. 2.2 in the $(\tau, \Delta E)$ phase space, where τ is the longitudinal coordinate of the particles and ΔE is the relative particle energy with respect to the beam total energy E. The measured bunch profile $\lambda(\tau)$ is the projection of the bunch distribution in phase space on the τ coordinate. Two parts in the bunch distribution can be distinguished: the first one (in grey) corresponds to the matched area (or stationary part) of the bunch, and the second (blue/orange) to the mismatched part (or quadrupolar perturbation). Only the particles of the mismatched distribution are contributing to the measured quadrupole oscillations. In absence of coherent oscillations (stable bunch), f_{s2} is defined by the frequency of the particles with the highest oscillation amplitude. Those are the ones that are the most affected by the non-linearities of the RF bucket implying that the simplified expression in Eq. (2.1) which is usually derived for small amplitudes of oscillations may not be accurate anymore. In this section, the synchrotron frequency of the particles with

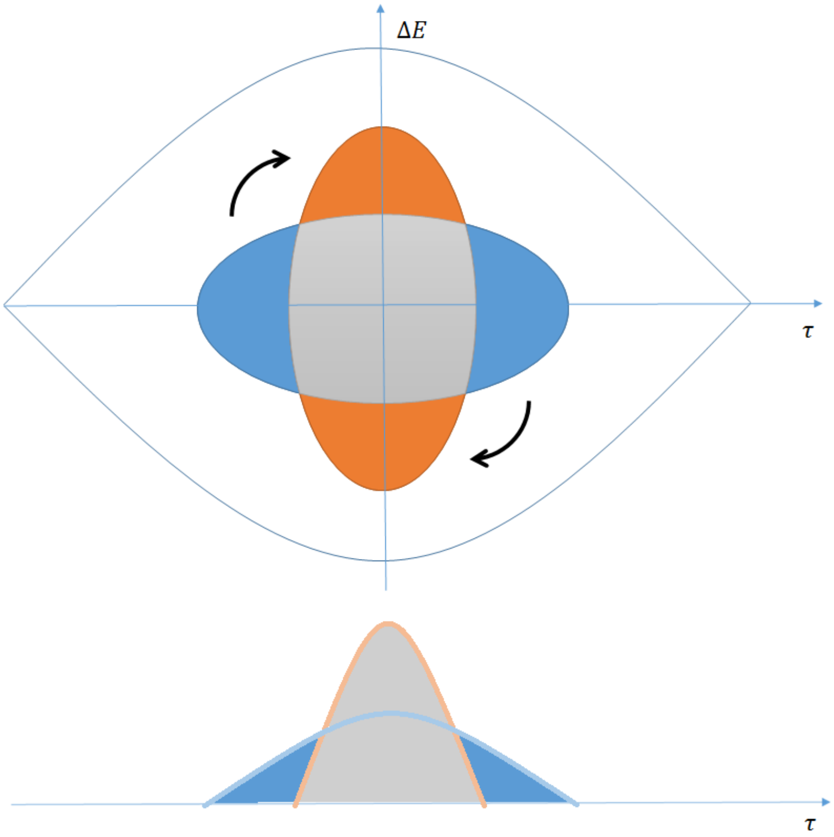

Figure 2.2 – Schematic presentation of the quadrupole oscillations. The upper figure represents the distribution in the phase space $(\tau, \Delta E)$, the lower one the corresponding longitudinal profile $\lambda(\tau)$, which is the projection of the bunch distribution in the τ dimension. The distribution is shown at two different times, in blue when the bunch length is the biggest and in orange when it is the smallest. The matched area (grey) does not contribute to the quadrupole oscillations, the mismatched area is in blue/orange.

large amplitude of oscillations will be considered.

2.2.1 Synchrotron frequency for particles with large oscillation amplitude

Let us first consider the quadrupole synchrotron frequency without intensity effects. For a particle oscillating in phase space with a maximum amplitude $\hat{\tau}$ in the τ dimension, the non-linear synchrotron frequency $f_s^{(0)}(\hat{\tau})$ is [43]:

$$\begin{aligned} f_s^{(0)}(\hat{\tau}) &= f_{s0}\frac{\pi}{2K\left[\sin\left(\omega_{\mathrm{RF}}\hat{\tau}/2\right)\right]} \\ &\approx f_{s0}\left[1-\frac{(\omega_{\mathrm{RF}}\hat{\tau})^2}{16}\right], \end{aligned} \tag{2.2}$$

where K is the complete elliptic integral of the first kind, ω_{RF} is the RF angular frequency, and f_{s0} is the synchrotron frequency for particles with small amplitude of oscillations ($\hat{\tau} \to 0$), defined as:

$$f_{s0} = \frac{1}{2\pi}\sqrt{\frac{\eta q V_{\mathrm{RF}} \omega_{\mathrm{RF}}}{\beta^2 E T_{\mathrm{rev}}}}. \tag{2.3}$$

Here $\eta = \gamma_t^{-2} - \gamma^{-2}$ is the slippage factor, q is the particle charge, V_{RF} is the RF voltage, β is the relativistic factor corresponding to E and $T_{\mathrm{rev}} = 1/f_{\mathrm{rev}} = 2\pi/\omega_{\mathrm{rev}}$ is the revolution period.

Without intensity effects, the synchrotron frequency $f_s^{(0)}$ has a quadratic dependence on the particle oscillation amplitude $\hat{\tau}$. Above, the mismatched part of the bunch distribution was assumed to be composed of particles with large amplitude of oscillations. For a small mismatch and assuming that the particles defining the mismatch have the same oscillation amplitude $\hat{\tau}$, by replacing in Eq. (2.2) $\hat{\tau} \approx \tau_L/2$, where τ_L is the full bunch length. Then, the quadrupole synchrotron frequency f_{s2} without intensity effects can be approximated as:

$$f_{s2}(\tau_L) \approx 2 f_{s0}\left[1 - \frac{(\omega_{\mathrm{RF}}\tau_L)^2}{64}\right]. \tag{2.4}$$

2.2.2 Incoherent synchrotron frequency shift

The effective voltage seen by a particle is modified by the induced voltage from all the impedance contributions along the ring. In this section, the modification of the synchrotron frequency distribution due to induced voltage from the stationary bunch distribution (incoherent shift Δf_{inc}) is considered. The induced voltage can be expressed as:

$$V_{\mathrm{ind}}(\tau) = -q N_b \int_{-\infty}^{\infty} \mathcal{S}(f)\, \mathcal{Z}(f)\, e^{j2\pi f \tau}\, df \tag{2.5}$$

where $\mathcal{S}(f)$ is the bunch spectrum corresponding to the stationary part of the bunch distribution. A first approximation is found by considering particles with small amplitude of oscillations and expanding Eq. (2.5) up to the linear terms in τ, giving:

$$V_{\mathrm{ind}}(\tau) \approx -q N_b (\mathcal{Z}_0 + \tau \mathcal{Z}_1). \tag{2.6}$$

The actual effect of the induced voltage on the bunch can be described by the effective resistive impedance $\mathcal{Z}_0$ and the effective reactive impedance $\mathcal{Z}_1$, and are defined as [43]:

$$\mathcal{Z}_0 \underset{\hat{\tau}\to 0}{\approx} \int_{-\infty}^{\infty} \mathcal{S}(f)\, \mathrm{Re}\mathcal{Z}(f)\, df, \tag{2.7}$$

$$\mathcal{Z}_1 \underset{\hat{\tau}\to 0}{\approx} -2\pi \int_{-\infty}^{\infty} f\, \mathcal{S}(f)\, \mathrm{Im}\mathcal{Z}(f)\, df. \tag{2.8}$$

The main effect of the effective resistive impedance $\mathcal{Z}_0$ is the asymmetry of the potential well and the synchronous phase shift. In the following development, the effect of $\mathcal{Z}_0$ on the synchrotron frequency shift is considered negligible. Therefore, the linear synchrotron frequency taking into account the induced voltage of a stationary bunch distribution is affected by the effective reactive impedance $\mathcal{Z}_1$ as:

$$f_{s0,\mathrm{inc}} = f_{s0}\sqrt{1+\frac{q}{\omega_\mathrm{RF}V_\mathrm{RF}}\mathcal{Z}_1 N_b}. \tag{2.9}$$

To evaluate the effective reactive impedance $\mathcal{Z}_1$, the relevant expressions of the bunch spectrum $\mathcal{S}\left(f\right)$ and the impedance $\mathcal{Z}\left(f\right)$ in the SPS are discussed. For proton bunches, the line density for a stationary distribution can be described using a binomial function:

$$\begin{aligned}\lambda\left(\tau\right) &= \frac{2\Gamma\left(3/2+\mu\right)}{\tau_L\sqrt{\pi}\Gamma\left(1+\mu\right)}\left[1-4\left(\frac{\tau}{\tau_L}\right)^2\right]^\mu,\\ \lambda\left(|\tau|>\tau_L/2\right) &= 0,\end{aligned} \tag{2.10}$$

where the line density $\lambda\left(\tau\right)$ is normalized to 1 and $\Gamma\left(x\right)$ is the Gamma function. Below, $\mu \geqslant 1$ with $\mu = 1$ giving a parabolic bunch and $\mu \to \infty$ a Gaussian bunch (typical values for the SPS bunches are in the range $\mu \in [1,2]$). The rms bunch length of the distribution (2.10) is:

$$\sigma_\mathrm{rms} = \frac{\tau_L}{2\sqrt{3+2\mu}}. \tag{2.11}$$

Below, the definition $\tau_{4\sigma} = 4\sigma_\mathrm{rms}$ is used, which is comparable to the full bunch length τ_L but is more convenient since for a fixed σ_rms, $\tau_L \to \infty$ if $\mu \to \infty$ ($\tau_{4\sigma}$ contains $\approx 95\%$ of the particles for $\mu \to \infty$ and 100% for $\mu = 1/2$). Moreover, the full bunch length τ_L is difficult to extract from measured profiles due to noise and it is not used for data analysis. Examples of bunch profiles are shown in Fig. 2.3a and the corresponding bunch spectra, shown in Fig. 2.3b, have the form:

$$\mathcal{S}\left(f\right) = {}_0F_1\left(\frac{3}{2}+\mu, -\frac{\left(\pi\tau_L f\right)^2}{4}\right), \tag{2.12}$$

where ${}_0F_1\left(x,y\right)$ is the Hypergeometric function.

In many practical cases, the impedance sources can be described as a resonator using the following expression:

$$\mathcal{Z}\left(f\right) = \frac{R_s}{1+jQ\left(\frac{f}{f_r}-\frac{f_r}{f}\right)}, \tag{2.13}$$

where R_s is the shunt impedance, Q is the quality factor determining the decay time of the wake, and f_r is the resonant frequency. The contribution to the low frequency reactive

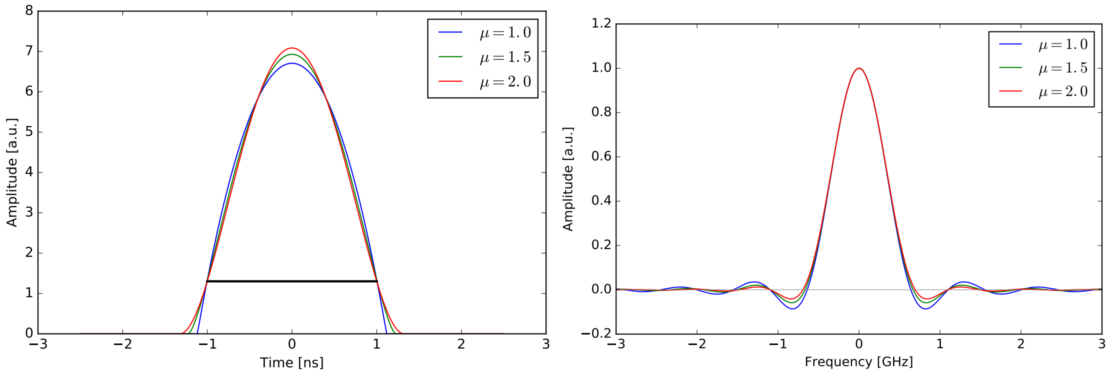

(a) Line density

(b) Spectrum

Figure 2.3 – Line densities (left) and corresponding spectra (right) for different μ values and the same rms bunch length σ_rms. The black line indicates the bunch length $\tau_{4\sigma}$.

impedance $\text{Im}\mathcal{Z}/n$, where $n = f/f_\text{rev}$, is:

$$\frac{\text{Im}\mathcal{Z}}{n} \underset{f\to 0}{=} \frac{R_s}{Q}\frac{f_\text{rev}}{f_r}. \tag{2.14}$$

Considering now a constant $\text{Im}\mathcal{Z}/n$ and using the bunch spectrum in (2.12) gives the analytical expression for $\mathcal{Z}_1$:

$$\begin{aligned}\mathcal{Z}_1 &= -\frac{2\pi}{f_\text{rev}}\text{Im}\mathcal{Z}/n\int_{-\infty}^{\infty}\mathcal{S}\left(f\right)f^2 df \\ &= -\frac{16\Gamma\left(3/2+\mu\right)}{\sqrt{\pi}\omega_\text{rev}\Gamma\left(\mu\right)}\frac{\text{Im}\mathcal{Z}/n}{\tau_L^3}.\end{aligned} \tag{2.15}$$

The expression (2.9) for the linear synchrotron frequency valid for any μ is:

$$f_{s0,\text{inc}} = f_{s0}\left[1-\frac{16\Gamma\left(3/2+\mu\right)q}{\sqrt{\pi}\Gamma\left(\mu\right)hV_\text{RF}\omega_\text{rev}^2}\frac{\text{Im}\mathcal{Z}/n}{\tau_L^3}N_b\right]^{\frac{1}{2}}, \tag{2.16}$$

where $h = \omega_\text{RF}/\omega_\text{rev}$ is the RF harmonic number. Assuming that the perturbation coming from the induced voltage is small and for a parabolic bunch ($\mu = 1$) the well-known formula for the incoherent synchrotron frequency shift is found back:

$$\frac{\Delta f_\text{inc}\left(\hat{\tau}\to 0\right)}{f_{s0}} \approx -\frac{6q}{hV_\text{RF}\omega_\text{rev}^2}\frac{\text{Im}\mathcal{Z}/n}{\tau_L^3}N_b. \tag{2.17}$$

Note that the incoherent synchrotron frequency shift has an inverse cubic dependence on bunch length, regardless of the bunch distribution (μ). Above transition, an inductive impedance ($\text{Im}\mathcal{Z}/n > 0$) decreases the linear synchrotron frequency, while a capacitive impedance ($\text{Im}\mathcal{Z}/n < 0$) increases it.

The expression for the incoherent synchrotron frequency shift in Eq. (2.16) is valid only for small amplitude of synchrotron oscillation. However the quadrupole oscillation frequency f_{s2} is determined by the particles with high amplitudes $\hat{\tau}$, as described in the previous section. It is not straightforward to express analytically $\Delta f_{\rm inc}$ for large $\hat{\tau}$. Moreover, for the usual bunch lengths the SPS impedance cannot be well represented by a constant $\mathrm{Im}\mathcal{Z}/n$ (which is also the case for most of the synchrotrons). For a resonant impedance (2.13), the reactive impedance $\mathrm{Im}\mathcal{Z}$ is inductive for $f < f_r$ and capacitive for $f > f_r$. Hence, the effective impedance $\mathcal{Z}_1$ can be either inductive or capacitive depending on how the bunch spectrum overlaps with $\mathrm{Im}\mathcal{Z}$. Note also the role of the positive and negative lobes in the bunch spectrum distribution (see Fig. 2.3b) that may change as well the value of the effective impedance $\mathcal{Z}_1$.

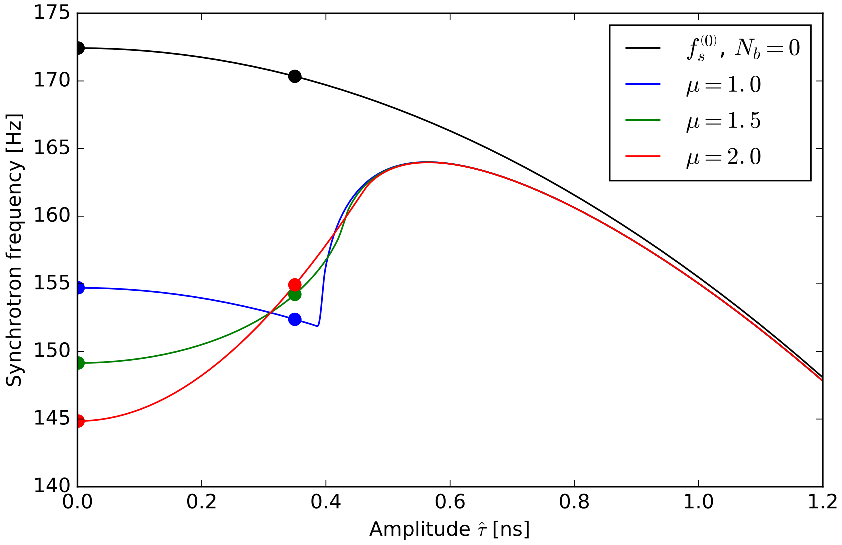

Figure 2.4 – The synchrotron frequency distribution $f_{s,\rm inc}^{(0)}(\hat{\tau})$ for different values of μ with the same $\tau_{4\sigma} = 0.7$ ns, using a pure reactive impedance $\mathrm{Im}\mathcal{Z}/n = 3\,\Omega$ and $N_b = 5\times10^{10}$ ppb for the Q26 optics parameters in Table 2.1. The dots represents the values at $\hat{\tau} = 0$ and $\hat{\tau} = \tau_{4\sigma}/2$.

The non-linear incoherent synchrotron frequency shift can be calculated in the general case using the action-angle variables together with:

$$f_{s,\rm inc}^{(0)}(\hat{\tau}) = \frac{1}{2\pi}\frac{d\mathcal{H}}{d\mathcal{J}}, \tag{2.18}$$

where $\mathcal{H}$ is the Hamiltonian and $\mathcal{J}$ is the action for a particle performing synchrotron oscillations with the amplitude $\hat{\tau}$. The non-linear synchrotron frequency $f_{s,\rm inc}^{(0)}$ was calculated numerically using Eq. (2.18) for different bunch profiles (μ) and bunch lengths $\tau_{4\sigma}$ taking into account the induced voltage. The SPS parameters for the Q26 optics in Table 2.1 were used, together with a simplified impedance model using $\mathrm{Im}\mathcal{Z}/n = 3\,\Omega$. An example is shown in Fig. 2.4 for $\tau_{4\sigma} = 0.7$ ns.

The relative incoherent synchrotron frequency shift $\Delta f_{\rm inc}/f_s^{(0)}$ is presented in Fig. 2.5 as a function of bunch length for small and large amplitude of particle oscillations (below, small amplitudes of particle oscillations correspond to $\hat{\tau} = 0$ and large amplitudes to $\hat{\tau} = \tau_{4\sigma}/2$). The

Table 2.1 – The SPS beam and machine parameters for the two different SPS optics.

Optics	γ_t	V_{RF} [MV]	f_{s0} [Hz]	$\mathcal{A}_b$ [eVs]	$\left(\frac{\mathrm{Im}\mathcal{Z}}{n}\right)_{\mathrm{SC}}$ [Ω]
Q20	17.95	2.8	517.7	0.473	-1.0
Q26	22.77	0.9	172.4	0.456	-1.27

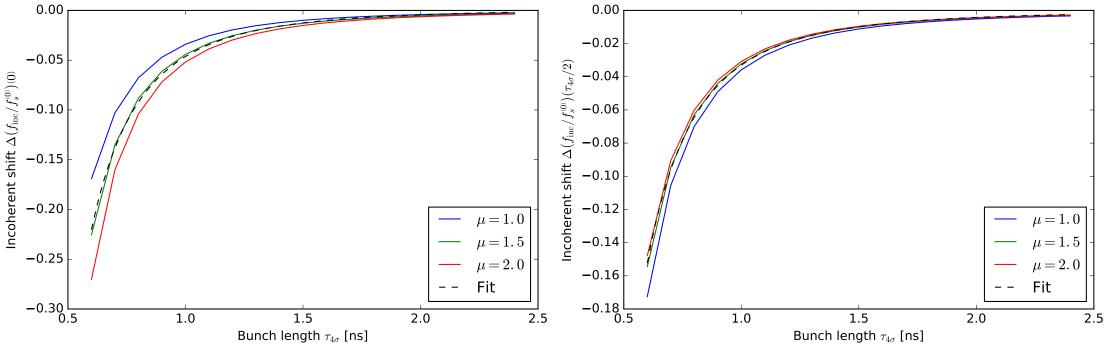

(a) Freq. shift for $\hat{\tau} = 0$

(b) Freq. shift for $\hat{\tau} = \tau_{4\sigma}/2$

Figure 2.5 – The relative incoherent synchrotron frequency shift as a function of bunch length for particles with $\hat{\tau} \approx 0$ (left) and $\hat{\tau} = \tau_{4\sigma}/2$ (right), using a pure reactive impedance $\mathrm{Im}\mathcal{Z}/n = 3\,\Omega$ and $N_b = 5 \times 10^{10}$ ppb for the Q26 optics parameters in Table 2.1.

expected scaling $\Delta f_{\mathrm{inc}} \propto 1/\tau_L^3$ is in good agreement with the numerical results for both small and large amplitude of oscillations. The Eq. (2.17) can be extended to any $\hat{\tau}$:

$$\frac{\Delta f_{\mathrm{inc}}}{f_s^{(0)}}(\hat{\tau}) \approx -\frac{6q}{hV_{\mathrm{RF}}\omega_{\mathrm{rev}}^2}\frac{\mathrm{Im}\mathcal{Z}/n}{\tau_L^3}N_b. \tag{2.19}$$

An interesting result is that the dependence on μ of the incoherent synchrotron frequency shift is bigger for $\hat{\tau} = 0$ than for $\hat{\tau} = \tau_{4\sigma}/2$. This is fortunate for the measurements since it implies that the measured quadrupole frequency f_{s2} should not depend too much on variations in the injected bunch profiles.

The same calculations were done using the full SPS impedance model, and results are shown in Fig. 2.6a and 2.6b. In this case the scaling $\propto 1/\tau_L^3$ does not work for the whole range of bunch length and the dependence of the incoherent synchrotron frequency shift on bunch length is non-monotonic. To evaluate how much the SPS impedance deviates from a constant reactive impedance, the equivalent impedance $(\mathrm{Im}\mathcal{Z}/n)_{\mathrm{eq}}$ is defined, based on Eq. (2.19), as:

$$(\mathrm{Im}\mathcal{Z}/n)_{\mathrm{eq}} \overset{\mathrm{def}}{=} \frac{\omega_{\mathrm{rev}}^2 V_{\mathrm{RF}} h}{6q}\frac{\Delta f_{\mathrm{inc}}}{f_s^{(0)}}\frac{\tau_{4\sigma}^3}{N_b}. \tag{2.20}$$

This impedance corresponds to the reactive impedance required to get the incoherent synchrotron frequency shift Δf_{inc}, assuming a parabolic bunch. Note the use of the bunch length

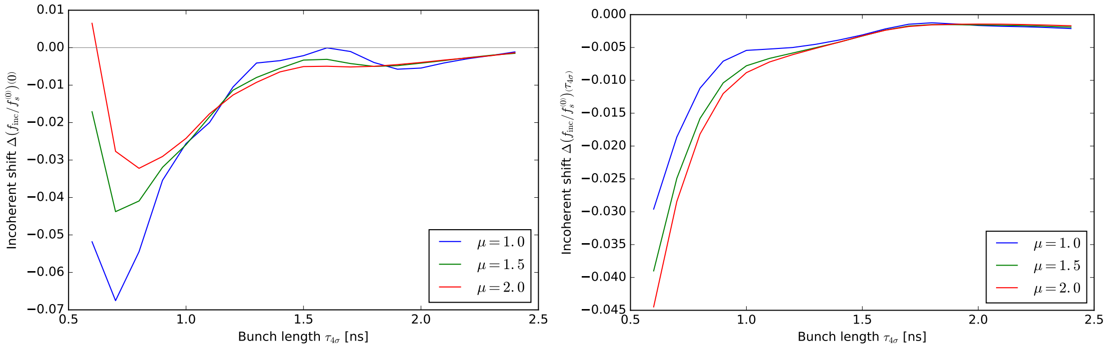

(a) Freq. shift for $\hat{\tau} = 0$ (b) Freq. shift for $\hat{\tau} = \tau_{4\sigma}/2$

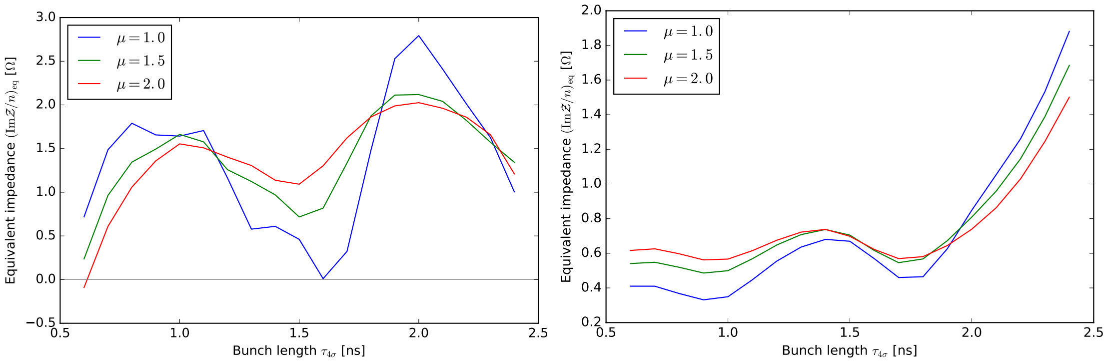

(c) Equivalent impedance - $\hat{\tau} = 0$ (d) Equivalent impedance - $\hat{\tau} = \tau_{4\sigma}/2$

Figure 2.6 – The incoherent synchrotron frequency shift calculated for particle distributions with different μ as a function of the bunch length $\tau_{4\sigma}$, for the Q26 optics parameters and $N_b = 5 \times 10^{10}$ ppb using the full SPS impedance model. The upper plots correspond to the incoherent frequency shift for small (left) and large (right) particle oscillation amplitudes $\hat{\tau}$. The bottom plots (c) and (d) are the equivalent reactive impedances $(\mathrm{Im}\mathcal{Z}/n)_{\mathrm{eq}}$ corresponding to cases (a) and (b).

$\tau_{4\sigma}$ rather than τ_L, which is more convenient for the comparison with measurements in Section 2.3.

The equivalent impedance $(\mathrm{Im}\mathcal{Z}/n)_{\mathrm{eq}}$ of the SPS for both small and large particle oscillation amplitudes $\hat{\tau}$ is shown in Fig. 2.6c and 2.6d. For small $\hat{\tau}$, the deviation with respect to the expected scaling $\propto 1/\tau_L^3$ is significant and it is different in amplitude depending on the particle distribution μ. For instance, the equivalent impedance is $(\mathrm{Im}\mathcal{Z}/n)_{\mathrm{eq}} \approx 0$ for $\mu = 1$ and $\tau_{4\sigma} \approx 1.6$ ns, so that the synchrotron frequency shift is the same as if there are no intensity effects at all in the centre of the bunch! For large $\hat{\tau}$, the shift also deviates from the expected scaling but with a different dependence on bunch length, indicating that the usual approximation of small particle oscillation amplitude $\hat{\tau} \to 0$ is not accurate. Additionally, a small variation of the average bunch length in measurements could lead to very different results meaning that the usual approximation of an impedance model with constant $\mathrm{Im}\mathcal{Z}/n$ is also not an accurate representation. For example, measuring the quadrupole frequency shift for bunches with an average bunch length of $\tau_{\mathrm{av}} \approx 1.4$ ns would give a bigger equivalent impedance than for $\tau_{\mathrm{av}} \approx 1.7$ ns by ≈ 30%, as shown in Fig. 2.6d.

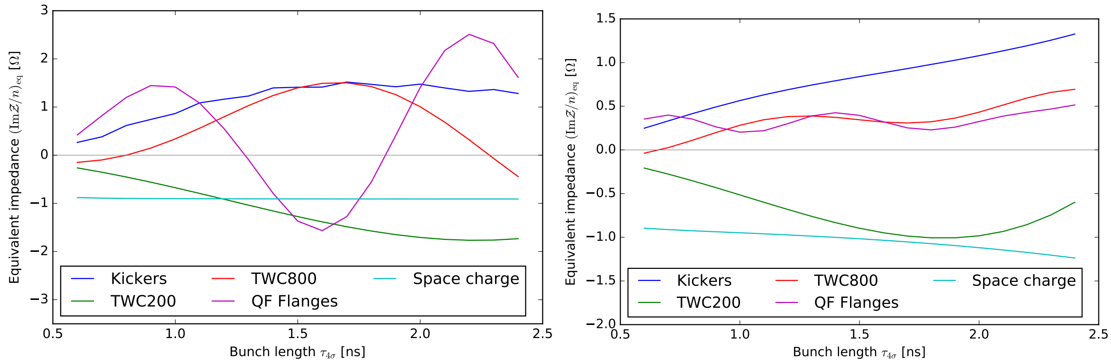

(a) Equivalent impedance - $\hat{\tau} = 0$

(b) Equivalent impedance - $\hat{\tau} = \tau_{4\sigma}/2$

Figure 2.7 – The equivalent impedance $(\mathrm{Im}\mathcal{Z}/n)_{\mathrm{eq}}$ of the main SPS impedance sources (shown in Fig. I.3), taken separately for a bunch distribution with $\mu = 1$, and for small (left) and large (right) particle oscillation amplitudes $\hat{\tau}$.

Finally, the independent contributions of the main impedance sources in the SPS (shown in Fig. I.3) on the synchrotron frequency shift was calculated. Their equivalent impedances $(\mathrm{Im}\mathcal{Z}/n)_{\mathrm{eq}}$ are shown in Fig. 2.7. These results are not directly comparable to the results obtained using the full impedance model since the contributions are not adding up linearly, but they give a rough estimation of what kind of shift can be expected from the various SPS impedance sources. For example, the space charge effect is a constant capacitive impedance and as expected its equivalent impedance is constant with a negative sign in Fig. 2.4. Broadband impedance sources (e.g. the kickers) give for both small and high amplitude $\hat{\tau}$ a contribution which is not strictly comparable to a constant impedance $\mathrm{Im}\mathcal{Z}/n$, but which is weakly dependant on bunch length. The contribution from the TWC at 200 MHz in this bunch length range is capacitive. Finally, resonant impedances located at high frequencies (the TWC at 800 MHz and the vacuum flanges) give a more particular behaviour with an important dependence on bunch length and particle oscillation amplitudes. For small amplitudes of oscillations they can either act as inductive or capacitive, depending on the bunch length, for small $\hat{\tau}$, while for large $\hat{\tau}$ they mainly act as an inductive impedance. They are the source of the variations in Fig. 2.6c and the peaks at $\tau_{4\sigma} \approx 0.7$ ns and $\tau_{4\sigma} \approx 1.4$ ns in Fig. 2.6d.

2.2.3 Coherent synchrotron frequency shift

In addition to the incoherent shift due to the stationary bunch distribution, the synchrotron frequency is also shifted due to the bunch spectrum appearing from oscillations of mode m (coherent shift $\Delta f_{\mathrm{coh},m}$). Like for the incoherent shift, the actual effect of the impedance depends on the overlapping of the perturbed bunch spectrum with the impedance and can be described by the effective impedance for coherent oscillations $\mathcal{Z}_{\mathrm{coh},m}$. The coherent synchrotron frequency shift can be evaluated by solving the linearised Vlasov equation for small amplitudes of particle oscillation $\hat{\tau} \to 0$. Following these assumptions and for quadrupole oscillations $m = 2$, $\Delta f_{\mathrm{coh},2}$ can be expressed as [19]:

$$\Delta f_{\mathrm{coh},2} = \frac{3\Gamma\left(5/2\right)}{8\pi^{5/2}} \frac{q^2\eta}{\beta^2 E f_{s0,\mathrm{inc}} \tau_L^3} \mathcal{Z}_{\mathrm{coh},2} N_b, \tag{2.21}$$

where the effective impedance $\mathcal{Z}_{\mathrm{coh},2}$ is:

$$\mathcal{Z}_{\mathrm{coh},2} = \frac{\sum_{n=-\infty}^{\infty} \mathcal{S}_2\left(n\right)\left(\mathrm{Im}\mathcal{Z}/n\right)}{\sum_{n=-\infty}^{\infty} \mathcal{S}_2\left(n\right)}. \tag{2.22}$$

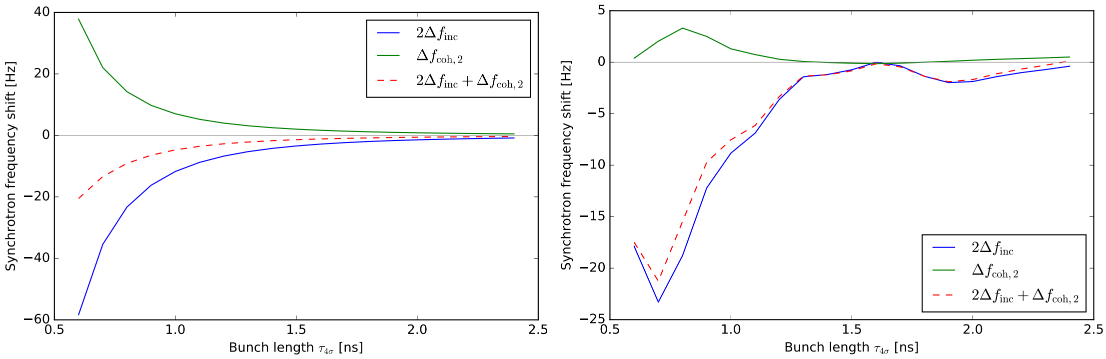

(a) Const. $\mathrm{Im}\mathcal{Z}/n$ - Shift $\hat{\tau} \to 0$

(b) SPS impedance - Shift $\hat{\tau} \to 0$

Figure 2.8 – Contribution of the incoherent shift $2\Delta f_{\mathrm{inc}}$ and the coherent shift $\Delta f_{\mathrm{coh},2}$ to the total synchrotron frequency shift $2\Delta f_{\mathrm{inc}} + \Delta f_{\mathrm{coh},2}$ as a function of bunch length, for a pure inductive impedance $\mathrm{Im}\mathcal{Z}/n = 3\ \Omega$ (left) and the full SPS impedance (right). The Q26 optics parameters in Table 2.1 were used with $N_b = 5 \times 10^{10}$ ppb.

For a parabolic bunch distribution with $\mu = 1$, the perturbed spectrum of quadrupole oscillations can be described by [19]:

$$\mathcal{S}_2\left(f\right) = \frac{\left[J_{5/2}\left(2\pi f \tau_L\right)\right]}{2\pi f \tau_L}. \tag{2.23}$$

A first approximation consists in considering a constant $\mathrm{Im}\mathcal{Z}/n$ in Eq. (2.22), giving $\mathcal{Z}_{\mathrm{coh},2} = \mathrm{Im}\mathcal{Z}/n$. Since the coherent shift $\Delta f_{\mathrm{coh},2}$ scales $\propto 1/\tau_L^3$ like the incoherent shift Δf_{inc}, the ratio between the two does not depend on the bunch length and is:

$$\frac{\Delta f_{\mathrm{coh},2}}{2\Delta f_{\mathrm{inc}}} \underset{\hat{\tau}\to 0}{\approx} -\frac{3\pi}{16} \frac{1}{\left(1 + \frac{\Delta f_{\mathrm{inc}}}{f_{s0}}\right)} \approx -0.6. \tag{2.24}$$

The coherent synchrotron frequency shift has an opposite sign and is comparable in amplitude with respect to the incoherent one. The total shift $2\Delta f_{\mathrm{inc}} + \Delta f_{\mathrm{coh},2}$ is reduced by more than a half with respect to the incoherent shift alone, as shown in Fig. 2.8a. Next, the effective impedance $\mathcal{Z}_{\mathrm{coh},2}$ is computed numerically using the full SPS impedance model and the influence of the coherent shift $\Delta f_{\mathrm{coh},2}$ is shown in Fig. 2.8b. Results are significantly different from the case with constant $\mathrm{Im}\mathcal{Z}/n$ and the coherent shift is small in comparison to the incoherent one.

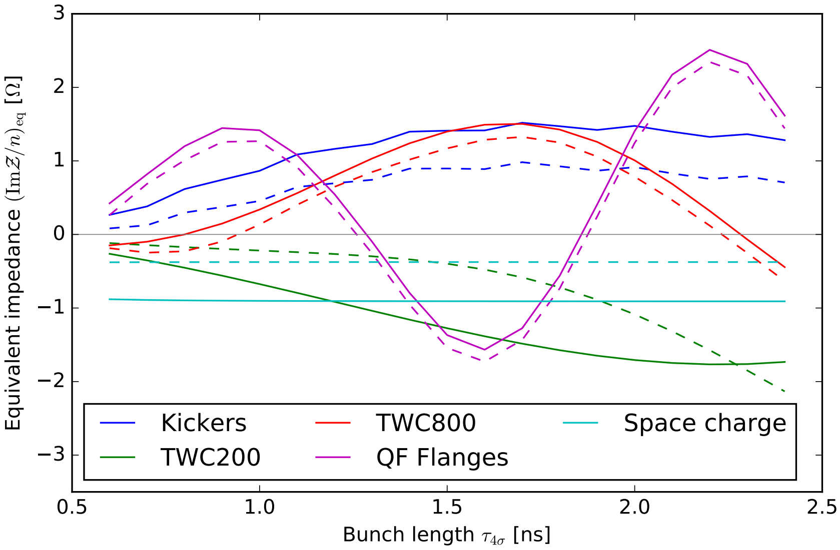

Figure 2.9 – The equivalent impedance $(\mathrm{Im}\mathcal{Z}/n)_{\mathrm{eq}}$ of the main SPS impedance sources in Fig. I.3 taken separately. The solid lines correspond to the equivalent impedances defined only from the incoherent shift Δf_{inc} as in Fig. 2.7, the dashed lines correspond to the equivalent impedances taking also into account the coherent shift $\Delta f_{\mathrm{coh},2}$.

The definition of the effective impedance in Eq. (2.20) can be extended to include the coherent frequency shift $\Delta f_{\mathrm{coh},2}$:

$$(\mathrm{Im}\mathcal{Z}/n)_{\mathrm{eq}} \overset{\mathrm{def}}{=} \frac{\omega_{\mathrm{rev}}^2 V_{\mathrm{RF}} h}{6q} \frac{\left(\Delta f_{\mathrm{inc}} + \Delta f_{\mathrm{coh},2}/2\right)}{f_{s0}} \frac{\tau_{4\sigma}^3}{N_b}. \tag{2.25}$$

To understand better the influence of the various SPS impedance sources shown in Fig. I.3, the equivalent impedance of each source was computed taking also into account the coherent shift $\Delta f_{\mathrm{coh},2}$. Results are shown in Fig. 2.9 (dashed lines). For broadband impedance sources (e.g. space charge, kickers) the equivalent impedance is reduced by the coherent shift by more than a half regardless of the bunch length, as expected for impedance sources close to a constant $\mathrm{Im}\mathcal{Z}/n$. Concerning the high frequency impedance sources (e.g. the TWC at 800 MHz, the vacuum flanges), the influence of the coherent shift is very small. Finally, for the TWC at 200 MHz the influence of the coherent shift $\Delta f_{\mathrm{coh},2}$ depends on the bunch length. For small bunch length $\tau_{4\sigma} < 1.5$ ns the influence of $\Delta f_{\mathrm{coh},2}$ is significant and reduces the equivalent impedance, while for large bunch length $\tau_{4\sigma} > 2.3$ ns the coherent shift even changes the sign and further increases the total shift.

To conclude, the quadrupole oscillation frequency f_{s2} is mainly determined by the particles oscillating with large oscillation amplitude $\hat{\tau}$. The observed shift with intensity is mainly defined by the incoherent synchrotron frequency shift Δf_{inc}, while for the SPS impedance the coherent shift $\Delta f_{\mathrm{coh},2}$ is assumed to be negligible. The dependence of f_{s2} on the bunch length is very strong, due to both the non linearities of the RF bucket and the frequency dependence of the SPS impedance.

2.3 Measurements of the quadrupole frequency shift

2.3.1 Setup

The quadrupole oscillation frequency f_{s2} was measured at injection in the SPS (kinetic energy $E_k = 25$ GeV) and its dependences, described in Section 2.2, were analysed by exploring a broad range of bunch intensities and lengths. The RF parameters in the SPS injectors were adjusted to scan the injected bunch properties [71]. In the SPS, the RF voltage was set for the injected bunch to be slightly mismatched hence initiating bunch length oscillations. The dipole oscillations were reduced thanks to the RF phase loop and this effect is considered negligible below. The longitudinal bunch profiles were acquired every turn using a Wall Current Monitor for an amount of turns covering approximately ten quadrupole oscillations periods. The bunch profile was corrected for the perturbation coming from the transfer function of the measurement line in order to get the correct bunch length [72]. The profiles were fitted with the binomial function (2.10) with $\mu = 3/2$ and the bunch length was defined as $\tau_{4\sigma} = 4\sigma_{\mathrm{rms}}$, where σ_{rms} is the rms bunch length of the fitting profile. The average bunch length of the oscillations are noted τ_{av} and the peak-to-peak amplitude $\Delta\tau$. The frequency of the bunch length oscillations f_{s2} was obtained from the maximum component of the Fast Fourier Transform. The bunch intensity N_b was measured using a DC Beam Current Transformer and an averaged value was taken. Finally, each acquired SPS cycle associates the quadrupole frequency f_{s2} with an average bunch length τ_{av}, a peak-to-peak amplitude of oscillations $\Delta\tau$ and a bunch intensity N_b. Examples of these acquisitions were shown in Fig. 2.1.

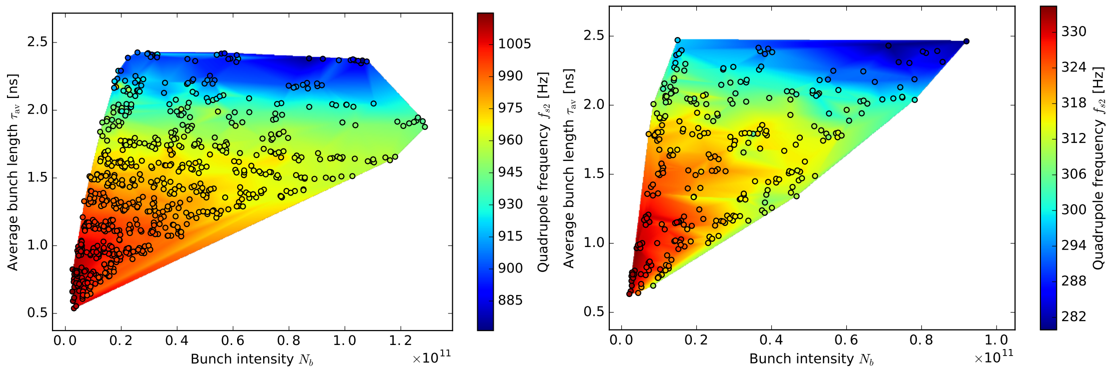

(a) Q20 optics

(b) Q26 optics

Figure 2.10 – Measured quadrupole frequency f_{s2} as a function of bunch length and intensity in both Q20 (left) and Q26 (right) optics. Each point corresponds to a single acquisition.

Two different optics are available in the SPS, named after the transverse tune: Q20 and Q26. The main difference is the different γ_t and therefore a different synchrotron frequency for the same bucket area $\mathcal{A}_b$. Another difference is the longitudinal space charge effect which is larger in the Q26 optics with respect to the Q20 optics. This is due to the different dispersion function which gives a smaller horizontal bunch size in the Q26 optics for the same transverse emittance [37]. Measurements were performed in both optics, and the raw data of the quadrupole frequency as a function of intensity and the average bunch length is shown in Fig. 2.10. The corresponding beam and machine parameters are shown in Table 2.1.

2.3.2 Data analysis and results

The dependence of the quadrupole frequency f_{s2} on intensity was studied by selecting the data with the same average bunch length τ_{av} (within ±50 ps). For each set, the dependence on intensity is obtained from the fit by a linear function $f_{s2} = a + b\,N_b$, as expected from Eq. (2.19). The origin of the fit a corresponds to the quadrupole frequency without intensity effects, while the slope b contains the information about the reactive impedance. Examples of measured quadrupole frequency f_{s2} as a function of intensity for different sets of average bunch length τ_{av} together with fits are shown in Fig. 2.11.

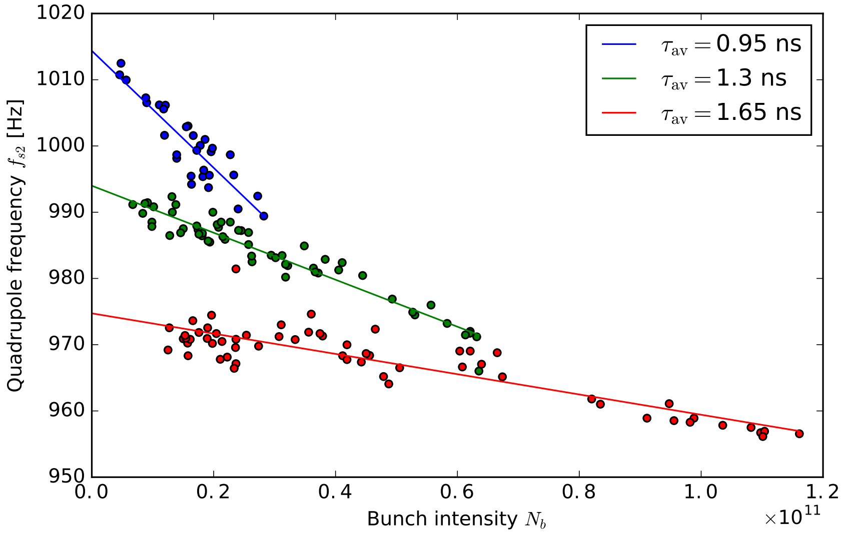

Figure 2.11 – Examples of measured quadrupole frequency f_{s2} as a function of intensity for selected average bunch lengths τ_{av} (within ±50 ps) in the Q20 optics. The lines correspond to a linear fit.

The dependence of the quadrupole frequency on bunch length can be studied from the fitted parameters a and b obtained for each set of τ_{av}. As discussed in Section 2.2, the measured quadrupole oscillations are mainly performed by the mismatched particles from the outer part of the distribution. The first consequence is that the quadrupole frequency without intensity effects $a\,(\tau_{\mathrm{av}})$ should follow Eq. (2.4). The comparison of measurements with the expected analytical formula is shown in Figs. 2.12a and 2.12b for both optics. They are in good agreement, confirming that the measured quadrupole frequency is dominated by contributions from particles with large synchrotron oscillation amplitudes. The small discrepancy between measurements and the expected scaling comes from the fact that Eq. (2.4) is valid for particles with maximum oscillation amplitude, while in measurements the frequency is determined by the sum of all the particles defining the mismatch.

It is possible to extrapolate the value of $2f_{s0}$ from the measured $a\,(\tau_{\mathrm{av}} \to 0)$ which gives the actual amplitude of the RF voltage during measurements (this parameter has an uncertainty of $\approx 5\%$). For both Q20 and Q26 optics the obtained values are in good agreement with the expected values from Table 2.1 ($2f_{s0} \approx 1035$ Hz in the Q20 optics and $2f_{s0} \approx 342$ Hz in the Q26 optics). The measured slope b is shown in Figs. 2.12c and 2.12d and it scales approximately as $\propto 1/\tau_{\mathrm{av}}^3$, in accordance to the expected scaling of the synchrotron frequency shift for large particle oscillation amplitudes $\hat{\tau}$ (see Fig. 2.6b).

The analysed parameters $a = 2f_s^{(0)}$ and $b = 2\Delta f_{\mathrm{inc}}/N_b$ can be recombined to obtain the equivalent reactive impedance as:

$$(\mathrm{Im}\mathcal{Z}/n)_{\mathrm{eq}} = \frac{\omega_{\mathrm{rev}}^2 V_{\mathrm{RF}} h}{6q} \frac{b}{a} \tau_{\mathrm{av}}^3, \tag{2.26}$$

following the same assumptions as used to derive Eq. (2.19). The results are shown in Figs. 2.12e and 2.12f. A remarkable observation is that measured pattern matches very well the results obtained semi-analytically and shown in Fig. 2.6d. The values of $(\mathrm{Im}\mathcal{Z}/n)_{\mathrm{eq}}$ are also very close, although the two quantities are not directly comparable as Eq. (2.19) is derived for a single particle. Moreover, a parabolic bunch profile was assumed in calculations while in measurements it varies a lot. Nevertheless, the relative agreement shows that in measurements the incoherent frequency shift for particles with large oscillation amplitudes $\hat{\tau}$ is indeed the dominant effect (assuming also that the impedance model is close enough to reality). Further details will be studied below from the comparison with macroparticle simulations. Note that the equivalent impedances $(\mathrm{Im}\mathcal{Z}/n)_{\mathrm{eq}}$ are very similar for the Q20 and Q26 optics since the dependence on the machine parameters V_{RF} and η was removed.

For the measured equivalent impedance $(\mathrm{Im}\mathcal{Z}/n)_{\mathrm{eq}}$ three different bunch length intervals can be distinguished. For $\tau_{\mathrm{av}} < 1.7$ ns, the results are similar in pattern and value between the Q20 and Q26 optics and correspond to the ideal bunch length range for these measurements. At $\tau_{\mathrm{av}} \approx 1.7$ ns, the measured equivalent impedance $(\mathrm{Im}\mathcal{Z}/n)_{\mathrm{eq}}$ in the Q20 and Q26 optics starts to be different. For the Q20 optics,the measured values keeps decreasing whilst the equivalent impedance grows in the case of the Q26 optics. For $\tau_{\mathrm{av}} > 2$ ns the measured equivalent impedance $(\mathrm{Im}\mathcal{Z}/n)_{\mathrm{eq}}$ in Q20 is completely unusable. This is explained by the motion of a mismatched bunch in phase space which is heavily affected by the non-linearities of the RF bucket for large bunch lengths. As shown in Fig. 2.1, the consequence is that the bunch profile changes with time and bunch length oscillations are quickly damped due to filamentation. In addition, the bunch is shortened in the SPS injector (PS) by a fast RF voltage increase (bunch rotation in phase space). For large bunch lengths, the distribution in phase

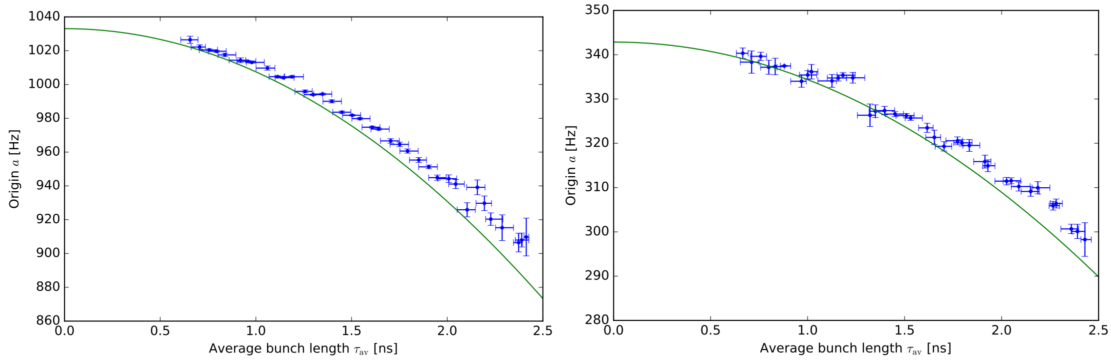

(a) Q20 optics - Origin a

(b) Q26 optics - Origin a

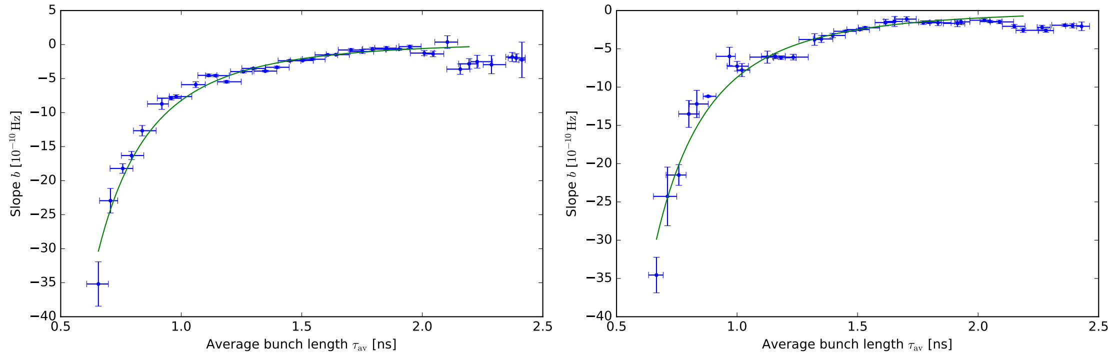

(c) Q20 optics - Slope b

(d) Q26 optics - Slope b

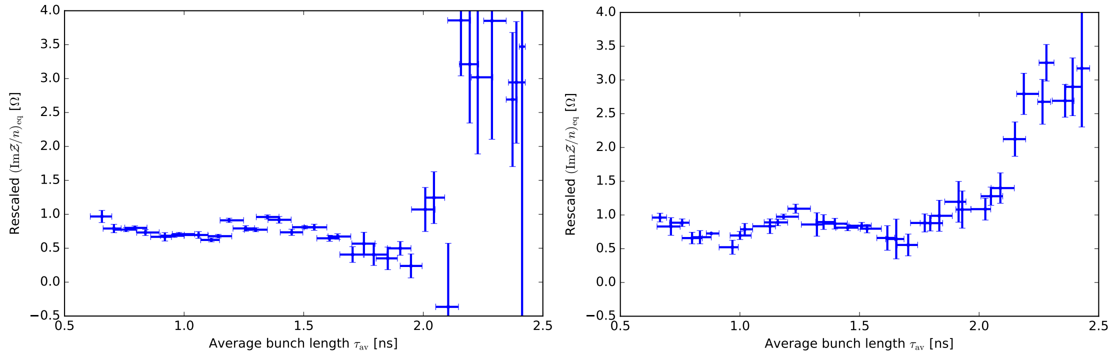

(e) Q20 optics - Equivalent impedance $(\mathrm{Im}\mathcal{Z}/n)_{\mathrm{eq}}$

(f) Q26 optics - Equivalent impedance $(\mathrm{Im}\mathcal{Z}/n)_{\mathrm{eq}}$

Figure 2.12 – The fitted origin a (top), slope b (middle) and the corresponding equivalent impedance $(\mathrm{Im}\mathcal{Z}/n)_{\mathrm{eq}}$ (bottom) of the quadrupole frequency shift with intensity, as a function of the average bunch length τ_{av}, in the Q20 (left) and Q26 (right) optics.

space is distorted during the bunch rotation in the longitudinal phase space and has an "S-shape" [73], making the filamentation effects even more difficult to reproduce. Moreover, the spectrum of a filamenting bunch has components at high frequency, which could affect the synchrotron frequency shift. In those conditions the results are varying from one acquisition to another. Nevertheless, the main observation is that for large bunch lengths the equivalent impedance $(\mathrm{Im}\mathcal{Z}/n)_{\mathrm{eq}}$ for $\tau_{\mathrm{av}} > 2$ ns is increasing, implying that long bunches are mainly sampling inductive impedance as expected from Fig. 2.6d.

2.4 Particle simulations

2.4.1 BLonD simulations

The dependence of the quadrupole frequency shift on the SPS impedance can be studied more precisely by macroparticle simulations that include the RF non-linearities and induced voltage. The simulation code BLonD was written at CERN to simulate longitudinal beam dynamics in synchrotrons and was successfully benchmarked with measurements in various accelerators and physics cases, including the synchrotron frequency shift with intensity [45]. All simulations were done using the SPS impedance model presented in Fig. I.3 (both resistive and reactive parts).

The SPS machine parameters were set in simulations to be the same as in measurements (for both optics in Table 2.1). To cover the same range of longitudinal emittances and bunch intensities obtained in measurements, each acquisition was reproduced in simulations by taking the injected bunch profile and reconstructing the bunch distribution in phase space using the Abel transform [51]. To get in simulations a mismatch close to the one in measurements, the bunch distribution in phase space was generated and the energy spread was iteratively adjusted so that the peak-to-peak bunch length oscillations $\Delta\tau$ are similar to the corresponding acquisition. For small bunch lengths, this approach is good enough to get input distributions close to the ones extracted from the PS without having to simulate the bunch rotation in the PS. Simulation results analysed applying exactly the same method as used for measurements are presented in Fig. 2.13.

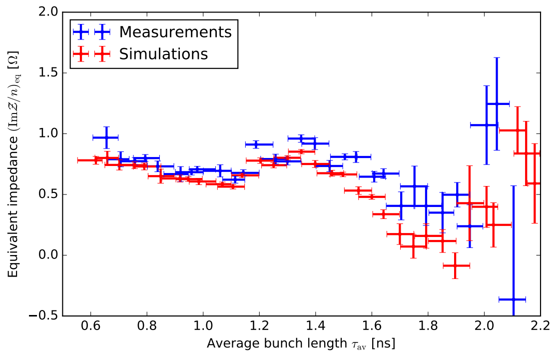

(a) Q20 optics

(b) Q26 optics

Figure 2.13 – Equivalent impedance $(\mathrm{Im}\mathcal{Z}/n)_{\mathrm{eq}}$ as a function of bunch length obtained from measurements (blue) and simulations (red) using the full SPS impedance model in the Q20 (left) and Q26 (right) optics.

Overall, simulations using the present SPS impedance model are in good agreement with measurements and the non-trivial dependence of the equivalent impedance $(\mathrm{Im}\mathcal{Z}/n)_{\mathrm{eq}}$ on bunch length is well reproduced in both optics. Nevertheless, some systematic deviations can be noticed. First, the equivalent impedance $(\mathrm{Im}\mathcal{Z}/n)_{\mathrm{eq}}$ is in general lower in simulations than in measurements, suggesting that some impedance is still missing in the SPS impedance model. Next, the discrepancy is higher for $\tau_{\mathrm{av}} \approx 1.6$ ns, indicating that the missing impedance has a particular frequency dependence. The results for $\tau_{\mathrm{av}} > 1.7$ ns are less accurate due to the limitations described above and may not be suitable to draw reliable assumptions on possible missing impedance.

2.4.2 Evaluation of the missing impedance

To define possible missing impedance sources, the simulations were reiterated by adding a variable amount of constant inductive impedance $\mathrm{Im}\mathcal{Z}/n$. Results are shown in Fig. 2.14. The present SPS impedance including space charge is represented in blue and the deviations between measurements and simulations could be explained by an additional inductive impedance in the order of $\mathrm{Im}\mathcal{Z}/n \approx (0-1.5)\ \Omega$ depending on the bunch length. This is comparable to the longitudinal space charge impedance of $(\mathrm{Im}\mathcal{Z}/n)_{\mathrm{SC}} \approx -1\ \Omega$. Omitting the longitudinal space charge impedance in simulations would correspond to the red line. In this case, the interpretation would have been opposite, since the conclusion would have been that the inductive impedance in the present model is in excess. Therefore, the longitudinal space charge effects are indeed not negligible and should be included in simulations at flat bottom in the SPS. An accurate evaluation of the longitudinal space charge impedance was done in Chapter 3 [37], leading to the values shown in Table 2.1 for both optics.

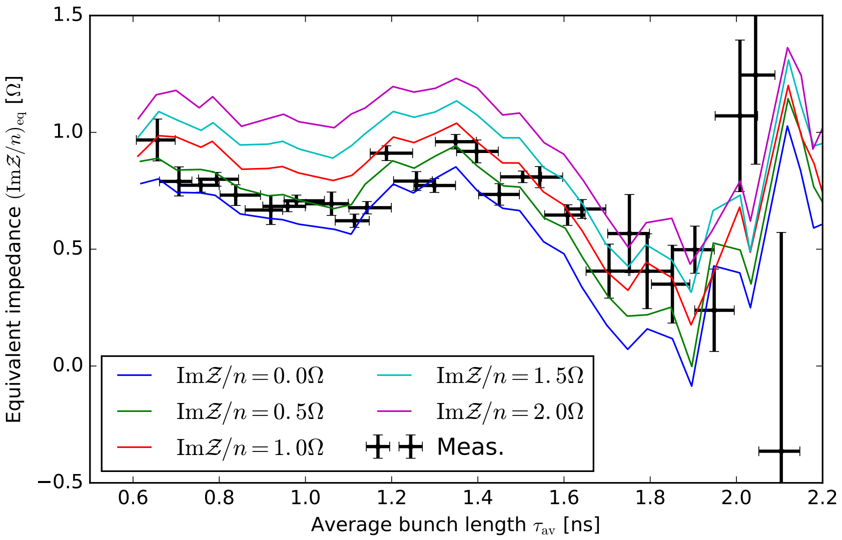

Figure 2.14 – Measured equivalent impedance $(\mathrm{Im}\mathcal{Z}/n)_{\mathrm{eq}}$ (black) in the Q20 optics compared with simulations (coloured lines) adding a variable amount of inductive impedance in the range $\mathrm{Im}\mathcal{Z}/n = (0-2)\ \Omega$ to the full SPS impedance model.

By using the previous scan in simulations adding a variable amount of constant inductive impedance $\mathrm{Im}\mathcal{Z}/n$, it is possible to determine for each bunch length the necessary impedance value to reach a perfect agreement between simulations and measurements. Results are shown in Fig. 2.15 for both optics.

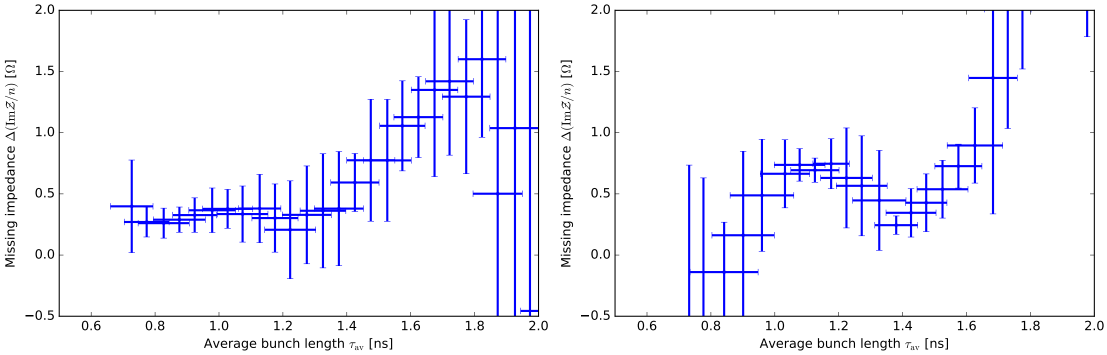

(a) Q20 optics

(b) Q26 optics

Figure 2.15 – Missing inductive impedance $\mathrm{Im}\mathcal{Z}/n$ as a function of bunch length needed to get a perfect agreement between measurements and simulations shown in Fig. 2.13 for both Q20 (left) and Q26 (right) optics.

For $\tau_{\mathrm{av}} < 1.4$ ns, the missing impedance is almost constant and it is necessary to add $\Delta\,(\mathrm{Im}\mathcal{Z}/n) \approx 0.3\,\Omega$ in the Q20 optics and $\Delta\,(\mathrm{Im}\mathcal{Z}/n) \approx 0.5\,\Omega$ in the Q26 optics to remove the deviations. For this large range of bunch lengths, a broadband impedance source could be the missing contribution, as determined in the previous section. Whilst non negligible, this missing contribution is still small in comparison with the full impedance budget and could be explained by an underestimation of a source in the model or some contributions that were not included.

For τ_{av} in the range $(1.4-1.7)$ ns, the missing impedance is increasing linearly, suggesting that an impedance source as a resonator could also be missing, as shown in Section 2.2. Simulations were done with an additional resonator where its resonant frequency f_r and impedance R_s/Q were scanned to further reduce the discrepancy. The best agreement was found for a resonator with $f_r \approx (350 \pm 50)$ MHz and $R/Q \approx (3 \pm 1)$ kΩ, leading to an almost perfect agreement in the Q20 optics as shown in Fig. 2.16a. While in the Q26 optics the agreement is also improved, some small deviations are still present at $\tau_{\mathrm{av}} \approx 1.0$ ns and $\tau_{\mathrm{av}} \approx 1.5$ ns (see Fig. 2.16b). Adding a single resonator is most probably not enough to correct all the deviations between measurements and simulations. A perfect description of the missing impedance is a multi-parametric task which requires a very large amount of measured data with small error-bars. Moreover, the realistic frequency dependence of a device contributing to the machine impedance could be more complex than that of a single resonator. Nevertheless, clear indications for the missing effective impedance as a function of bunch length can be exploited to get hint and direction for further searches. The missing contribution, depending on its frequency, could also be critical to have a reliable SPS impedance model for the bunch stability studies required for the SPS upgrade.

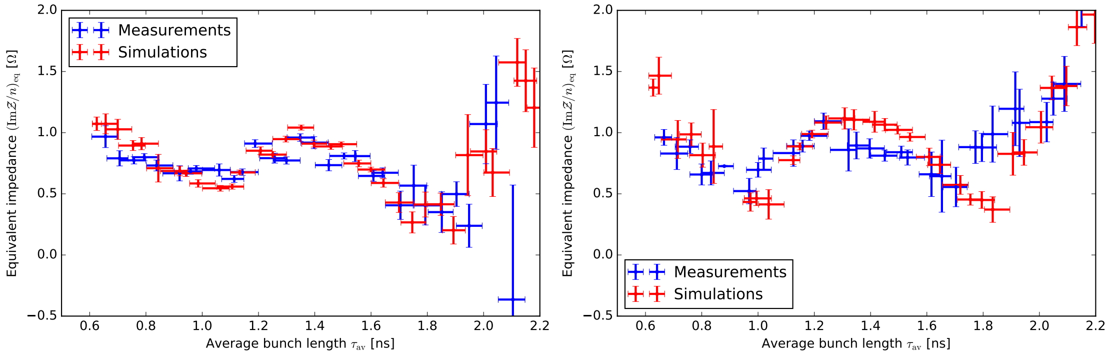

(a) Q20 optics

(b) Q26 optics

Figure 2.16 – Equivalent impedance $(\mathrm{Im}\mathcal{Z}/n)_{\mathrm{eq}}$ in measurements and simulations after adding an extra resonator with f_r = 350 MHz and R_s/Q = 3 kΩ to the SPS impedance model to compensate for deviations from measurements in both Q20 (left) and Q26 (right) optics.

2.5 Conclusions

The measured quadrupole frequency shift with intensity has been used to probe the reactive part of the SPS machine impedance. Being very sensitive to the average bunch length because of the non-linearities of the RF bucket and the induced voltage, this method can nevertheless be used to have an estimate of the missing impedance and its frequency dependence. Measurements were done in the SPS in two different optics and allowed, from good agreement with particle simulations, to show that the present SPS impedance model is satisfactory to reproduce the measured synchrotron frequency shift. The agreement can be further increased by adding a resonant impedance at $f_r \approx$ 350 MHz with $R/Q \approx 3\,\mathrm{k}\Omega$, the real source to be investigated. As the studies for the HL-LHC project rely on the accurate reproduction of beam instabilities, any missing impedance could be crucial and this method is an effective way to test the existing impedance model. Beyond the evaluation of the longitudinal impedance model, the study of the synchrotron frequency shift is also important as it is a key component to determine the instability mechanisms related to the loss of Landau damping.

3 Longitudinal Space Charge in the SPS

3.1 Introduction

Longitudinal space charge is one of the main collective effects in low energy machines, in particular at CERN in the PS Booster and PS (at injection energy). In the SPS, the longitudinal space charge effects are not negligible at low energy, and rapidly decrease during the acceleration ramp. The longitudinal space charge can be be modelled by a reactive impedance Im$\mathcal{Z}/n$, and a rapid evaluation gives as order of magnitude Im$\mathcal{Z}/n \approx -1\ \Omega$ in the SPS at injection (kinetic energy $E_k = 25$ GeV). This may seem to be small in comparison to the PS Booster and the PS, for which the longitudinal space charge impedance has the order of magnitude Im$\mathcal{Z}/n \propto -10^2\ \Omega$. Nevertheless, it was proven in Chapter 2 to be important in the SPS at low energy and even comparable to the other impedance sources. The effective impedance for the various contributions in the SPS is shown together with the longitudinal space charge impedance in Fig. 2.9.

A precise evaluation of the longitudinal space charge is necessary, or the deviations between the beam measurement of the impedance and the macroparticle simulations could be wrongly interpreted as a missing inductive impedance. A proper evaluation of space charge is also needed in macroparticle simulations done to study instabilities through the ramp (see Chapter 5 [74]. For a fixed longitudinal emittance, the bunch length τ_L and momentum spread δ_{rms} are affected by intensity effects due to potential-well distortion as described in the Chapter 1. If space charge is not implemented correctly in simulations, the initial bunch distribution may not be accurate, which could change the instability threshold in simulations.

The longitudinal space charge impedance integrated over one turn in the machine can be modelled by a constant reactive impedance Im$\mathcal{Z}/n$ with the following expression [75]:

$$\left(\frac{\mathrm{Im}\mathcal{Z}}{n}\right)_{\mathrm{SC}} = -\frac{\mathcal{Z}_0}{\beta\gamma^2}\, g, \tag{3.1}$$

where $\mathcal{Z}_0$ is the free space impedance, β and γ are the relativistic factors corresponding to the total beam energy E, $n = f/f_{\mathrm{rev}}$ with f being the frequency and f_{rev} the revolution frequency.

The geometrical factor g depends on the vacuum chamber size and geometry (aperture) with respect to the transverse bunch size. This formula is only valid in the long-wavelength limit, implying that the bunch spectrum is in the frequency region $f \ll \beta c \gamma / (2\pi a)$, c being the speed of light and a being the bunch radius. For a typical case at flat bottom in the SPS (kinetic energy $E_k = 25$ GeV and for the values of a in Table 3.1), the Eq. (3.1) is valid for $f \ll 300$ GHz. Bunches in the SPS have a bunch length $\tau_L \approx (1.5-3)$ ns, so the range of the bunch spectrum $\mathcal{S}(f)$ in frequency is typically < 1 GHz which validates the approximation.

The induced voltage due to an impedance $\mathcal{Z}$ is:

$$V_{\text{ind}}(\tau) = -qN_b \int_{-\infty}^{\infty} \mathcal{S}(f)\, \mathcal{Z}(f)\, e^{j2\pi f\tau}\, df, \tag{3.2}$$

where q is the charge of the particles and N_b is the bunch intensity (in particle per bunch ppb). Considering the longitudinal space charge impedance for which $\text{Im}\mathcal{Z}/n$ is constant, the Eq. (3.2) leads to:

$$V_{\text{SC}}(\tau) = -\frac{qN_b}{2\pi f_{\text{rev}}} \frac{\text{Im}\mathcal{Z}}{n} \frac{d\lambda}{d\tau}, \tag{3.3}$$

where λ is the bunch profile normalised to 1 and τ is the longitudinal coordinate in time.

The geometrical factor g can be expressed analytically under some assumptions. In the SPS, it changes depending on the location in the ring. The first relevant case is to consider a bunch with a round and uniform transverse distribution travelling through a rectangular chamber [75]:

$$g = C_{\text{SC}} + \ln\left[\frac{2h}{\pi a} \tanh\left(\frac{\pi w}{2h}\right)\right], \frac{w}{h} > 1, \tag{3.4}$$

where w is the full width and h is the full height of a rectangular vacuum chamber. A second case is to consider a bunch with a round and uniform transverse distribution in a circular vacuum chamber:

$$g = C_{\text{SC}} + \ln\left(\frac{r}{a}\right), \tag{3.5}$$

where r is the radius of the circular chamber. In both (3.4) and (3.5), C_{SC} is a value depending on the radial position of a given particle. Since a single particle does many betatron oscillations during one revolution in the machine, it will alternatively feel high longitudinal space charge effects while in the centre of the bunch (transversally), and weaker effect while in the tails. To represent that, the space charge impedance is averaged over the transverse bunch distribution leading to $C_{\text{SC}} = 1/4$ [75], this value is taken for the rest of the development.

The longitudinal space charge impedance can be estimated using Eq. (3.1) by taking an average bunch and aperture size. A more accurate approach consists in computing g at each position s in the ring taking into account the change in aperture and bunch size, and then integrating over one turn. This can be done either by using the Eqs. (3.4) and (3.5), or computing the geometrical factor g numerically for an arbitrary bunch distributions and aperture (e.g. Gaussian distribution, elliptical aperture). The different methods are compared in Section 3.2. The variation of the longitudinal space charge effects is evaluated depending on the energy and the bunch distribution in Section 3.3.

3.2 Evaluation of the space charge at all positions in the ring

3.2.1 Aperture geometry along the ring and bunch distribution

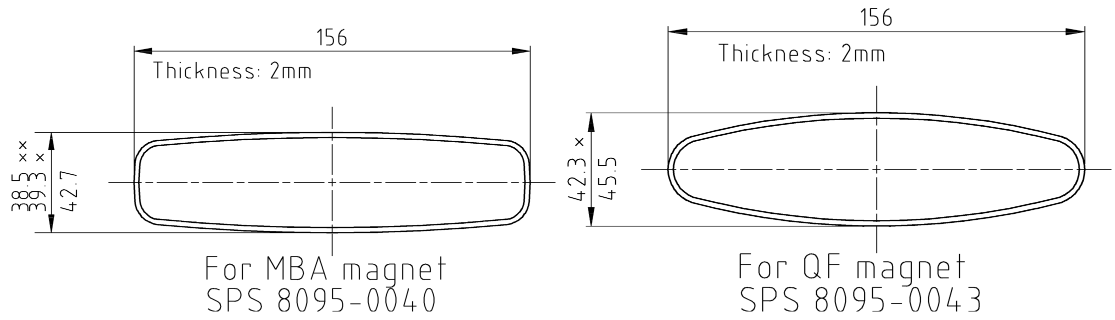

(a) (b)

Figure 3.1 – Examples of vacuum chamber geometries in the SPS for dipole magnet MBA (left) and quadrupole magnet QF (right).

To evaluate longitudinal space charge, the information about the SPS aperture and the corresponding transverse bunch size was obtained from the MAD output file based on the layout database [76]. The great majority of the ring ($\approx$ 70%) is composed of dipole magnets. Its geometry is very close to a rectangular shape, an example is shown for the MBA-type bending magnet in Fig. 3.1a. The rest of the ring is mainly composed of other magnets (quadrupole, sextupole, octupole, kickers) or junctions between them (vacuum flanges, pumping ports) which have different geometries depending on their function and location. Not all the information about the aperture was available (about 85%) but the known information can be considered to be a good representation of the whole ring. The missing aperture was interpolated linearly between known elements. A second example is shown in Fig. 3.1b for the QF-type quadrupole that can be considered as elliptical.

The transverse bunch distribution is assumed to be Gaussian and the beam size is computed from the Twiss functions as:

$$\begin{aligned} \sigma_x(s) &= \sqrt{\frac{\varepsilon_x}{\beta\gamma}\beta_x(s) + [D_x(s)\,\delta_{\mathrm{rms}}]^2}, \\ \sigma_y(s) &= \sqrt{\frac{\varepsilon_y}{\beta\gamma}\beta_y(s)}, \end{aligned} \tag{3.6}$$

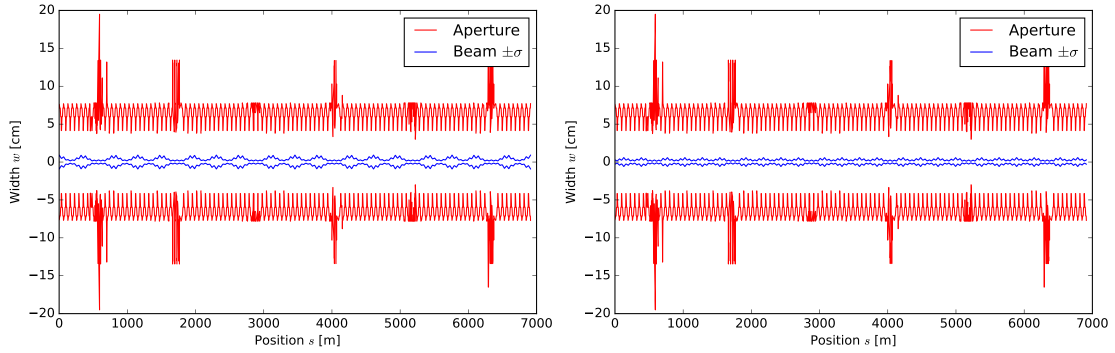

(a) Q20 optics - Horizontal

(b) Q26 optics - Horizontal

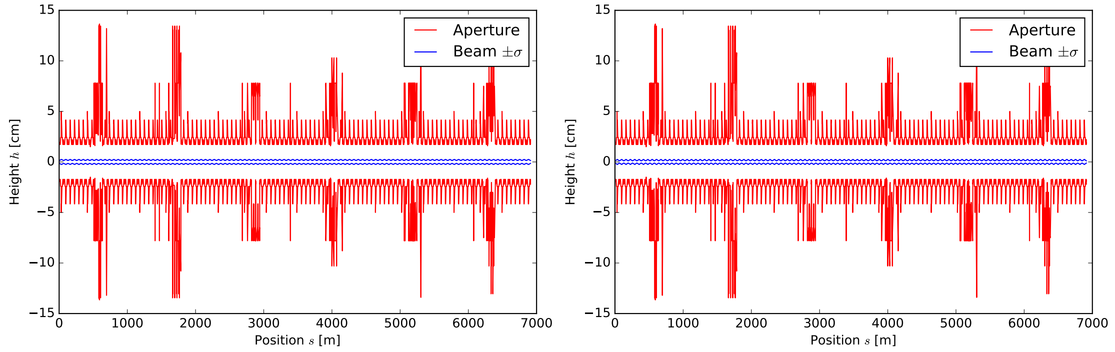

(c) Q20 optics - Vertical

(d) Q26 optics - Vertical

Figure 3.2 – Aperture and beam size along the ring in the Q20 (left) and Q26 (right) optics, in the horizontal (top) and vertical (bottom) planes for the normalised transverse emittance $\varepsilon_{x,y} = 1.7\,\mu$m and the momentum spread $\delta_{\text{rms}} = 1.1 \times 10^{-3}$.

where $\sigma_{x,y}$ is the rms beam size, $\varepsilon_{x,y}$ is the normalised transverse emittance, $\beta_{x,y}$ is the Twiss beta function along the ring, D_x is the horizontal dispersion function and δ_{rms} is the rms momentum spread of the bunch. Two optics parameters are available in the SPS: Q20 and Q26 named after the transverse tune and for which the $\beta_{x,y}$ and D_x functions are different. The horizontal and vertical size of the aperture along the ring is shown in red in Fig. 3.2 together with the beam size in blue using $\varepsilon_{x,y} = 1.7$ μm and $\delta_{\text{rms}} = 1.1 \times 10^{-3}$ for the two optics. For the same transverse emittance $\varepsilon_{x,y}$, the horizontal beam size in the Q20 optics is bigger than in the Q26 optics because of the higher $\beta_{x,y}$ and D_x functions (compare Fig. 3.2a with Fig. 3.2b). Consequently, for the same transverse emittance and momentum spread the longitudinal space charge in the Q20 optics is expected to be smaller than in the Q26 optics. The vertical beam size is almost identical.

3.2.2 Evaluation of the space charge using averaged beam and aperture parameters

First, a coarse estimation of the longitudinal space charge impedance is done by using Eq. (3.1) and considering only a rectangular aperture as in Eq. (3.4). The average horizontal and vertical bunch sizes $\langle \sigma_{x,y} \rangle$ are computed using Eq. (3.6) and by using averaged $\langle \beta_{x,y} \rangle$ and $\langle D_x \rangle$ functions over one turn. The average bunch radius is defined as $\langle a \rangle = \sqrt{2} \left(\langle \sigma_x \rangle + \langle \sigma_y \rangle \right)/2$, and the aperture has an average height $\langle h \rangle$, and width $\langle w \rangle$. The results are shown in Table 3.1 for the same example of bunch parameters $\varepsilon_{x,y} = 1.7\,\mu$m and $\delta_{\mathrm{rms}} = 1.1 \times 10^{-3}$.

With this method, the values $(\mathrm{Im}\mathcal{Z}/n)_{\mathrm{Q20}} = -1.32\ \Omega$ and $(\mathrm{Im}\mathcal{Z}/n)_{\mathrm{Q26}} = -1.43\ \Omega$ are obtained. Note that as expected the longitudinal space charge is higher in the Q26 optics than in the Q20 ones.

Table 3.1 – Longitudinal space charge impedance found using averaged beam and aperture sizes over one turn for a normalised transverse emittance $\varepsilon_{x,y} = 1.7\,\mu$m and a momentum spread $\delta_{\mathrm{rms}} = 1.1 \times 10^{-3}$, using the geometrical factor g for a uniform bunch distribution in a rectangular aperture as in Eq. (3.4).

	Q20	**Q26**
$\langle \beta_x \rangle$ [m]	63.03	54.80
$\langle \beta_y \rangle$ [m]	62.54	54.32
$\langle D_x \rangle$ [m]	2.96	1.88
$\langle \sigma_x \rangle$ [mm]	3.80	2.76
$\langle \sigma_y \rangle$ [mm]	1.96	1.83
$\langle a \rangle$ [mm]	4.07	3.24
$\langle w \rangle$ [cm]	12.94	12.94
$\langle h \rangle$ [cm]	4.74	4.74
$\mathrm{Im}\mathcal{Z}/n$ [Ω]	-1.32	-1.43

3.2.3 Evaluation of the space charge along the ring using a simplified geometry

For a more accurate calculation, the longitudinal space charge impedance is decomposed into smaller elements:

$$\left(\frac{\mathrm{Im}\mathcal{Z}}{n} \right)_{\mathrm{SC},i} = -\frac{\mathcal{Z}_0}{\beta\gamma^2} \frac{g_i l_i}{C}, \tag{3.7}$$

where g_i is the geometrical factor at a given position s in the ring, l_i is the length of section corresponding to g_i and C is the full length of the machine. The geometrical factor g_i is computed at each location in the ring taking into account the variations of the aperture size and geometry and the corresponding bunch size. The Eqs. (3.4) and (3.5) are used where relevant (elliptical shapes are approximated by rectangular shapes here). Concerning the bunch radius a, it is approximated again as $a = \sqrt{2} \left(\sigma_x + \sigma_y \right)/2$. Finally, all the contributions of $(\mathrm{Im}\mathcal{Z}/n)_{\mathrm{SC},i}$ are summed to get the total longitudinal space charge impedance for one turn. The values of $(\mathrm{Im}\mathcal{Z}/n)_{\mathrm{SC},i}$ at each position in the ring are represented for both Q20 and Q26 optics in Fig. 3.3a and 3.3b. The sum is shown in Fig. 3.3c and 3.3d.

With this refined method, the values $(\mathrm{Im}\mathcal{Z}/n)_{\mathrm{Q20}} = -1.05\ \Omega$ and $(\mathrm{Im}\mathcal{Z}/n)_{\mathrm{Q26}} = -1.17\ \Omega$ are obtained. These values are lower than the coarse estimation done in Section 3.2.2 using average bunch and vacuum chamber sizes, which overestimates the longitudinal space charge impedance.

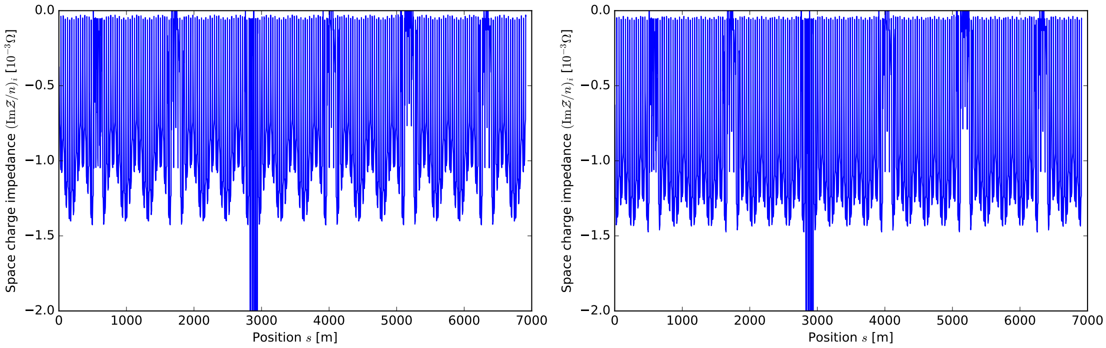

(a) Q20 optics - $(\mathrm{Im}\mathcal{Z}/n)_{\mathrm{SC},i}$ (b) Q26 - $(\mathrm{Im}\mathcal{Z}/n)_{\mathrm{SC},i}$

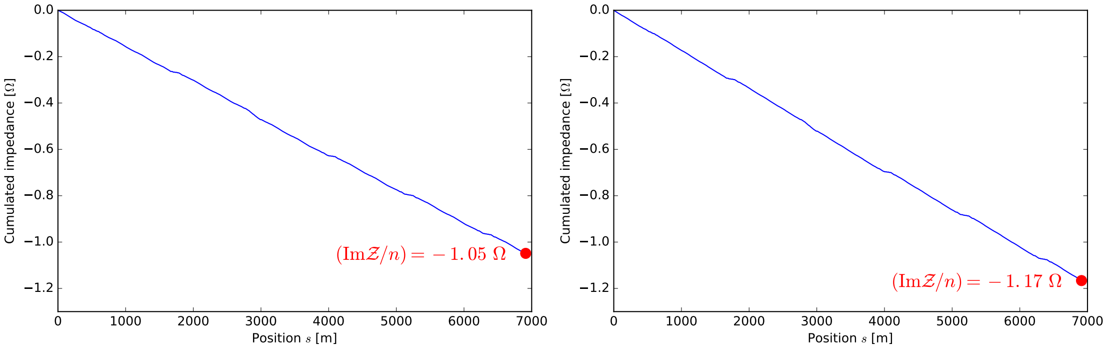

(c) Q20 optics - Cumulated (d) Q26 optics - Cumulated

Figure 3.3 – Longitudinal space charge impedance $(\mathrm{Im}\mathcal{Z}/n)_{\mathrm{SC},i}$ at each position in the ring (top) and cumulated impedance over the ring for one turn (bottom) in both Q20 (left) and Q26 (right) optics for a normalised transverse emittance $\varepsilon_{x,y} = 1.7\,\mu$m and a momentum spread $\delta_{\mathrm{rms}} = 1.1 \times 10^{-3}$.

3.2.4 Evaluation of the space charge along the ring with the LSC code

Another method consists in computing the longitudinal space charge impedance numerically for an arbitrary bunch distribution and aperture. For instance, the bunch size is larger in the horizontal than in the vertical plane (compare top with bottom plots in Fig. 3.2 and values in Table 3.1) and has a Gaussian bunch distribution, unlike in Eqs. (3.4) and (3.5), where the bunch is assumed to be uniform and circular. Additionally some special aperture geometries (e.g. elliptical) are not approximated anymore. The numerical calculation was done using the

Longitudinal Space Charge (LSC) code [75, 77]. The code is based on Finite Elements Methods and requires as an input a meshed model of the aperture as shown in Fig. 3.4. The various apertures available in the SPS described above were meshed and combined with the relevant bunch distribution to get the elementary space charge impedance $(\mathrm{Im}\mathcal{Z}/n)_{\mathrm{SC},i}$ at each point in the ring. The total impedance is finally summed over one turn, following the same steps as in section 3.2.3.

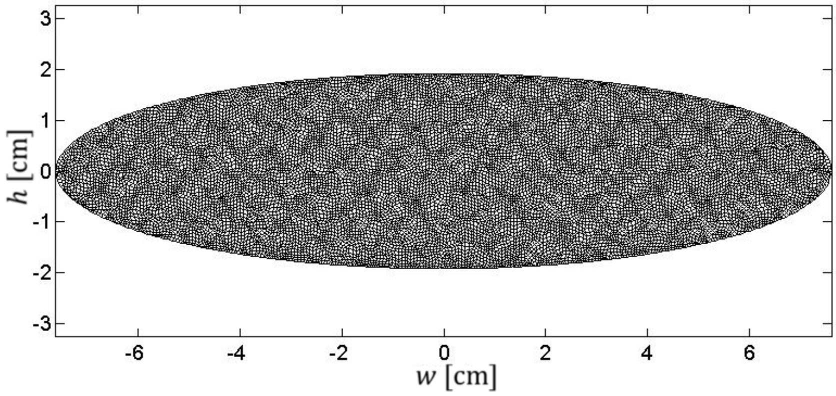

Figure 3.4 – Meshed aperture for the QF vacuum chamber in Fig. 3.1b used in the LSC code. The geometry is assumed to be elliptical.

The final values obtained taking into account the detailed information of the aperture and bunch distribution, are $(\mathrm{Im}\mathcal{Z}/n)_{\mathrm{Q20}} = -1.03\ \Omega$ and $(\mathrm{Im}\mathcal{Z}/n)_{\mathrm{Q26}} = -1.14\ \Omega$, which are very close to the results obtained in section 3.2.3.

3.2.5 Summary of the methods to compute the geometrical factor

The results obtained using the different methods in sections 3.2.2, 3.2.3 and 3.2.4 are summarised in Table 3.2. The coarse method using a single average bunch size and aperture overestimates the space charge impedance by ≈ 30% with respect to the computation of the space charge impedance by integrating the elementary contributions. Using the analytical geometrical factors and the LSC code gives similar results for the SPS (within 2%). Computing the longitudinal space charge impedance from the analytical geometrical factors is fast and can be used in a tracking code to have a self-consistent space charge model in simulations. This could be done by iteratively updating the space charge impedance at each turn taking into account the variations in energy, momentum spread, etc...

3.3 Longitudinal space charge during the cycle

The longitudinal space charge effect can change within the same cycle or from the beam variations from one cycle to another, but some parameters are more dominant than the others. The parameters affecting the longitudinal space charge effects are the Lorentz factor γ, the normalised transverse emittance $\varepsilon_{x,y}$, the bunch length τ_L and the momentum spread δ_{rms}.

Table 3.2 – Longitudinal space charge impedance calculated with the different methods presented in this paper for $\varepsilon_{x,y} = 1.7\,\mu$m and $\delta_{\mathrm{rms}} = 1.1 \times 10^{-3}$.

Im$\mathcal{Z}/n$ [Ω] **Method**	**Q20**	**Q26**
Section 3.2.2 - Averaged	-1.32	-1.43
Section 3.2.3 - Detailed (from Eq. (3.4), (3.5))	-1.05	-1.17
Section 3.2.4 - Detailed (from LSC code)	-1.03	-1.14

Concerning the momentum spread, it is determined by the longitudinal emittance ε_L and the RF bucket shape, which depends on the RF voltage V_{RF} and the slippage factor η (different for the Q20 and Q26 optics).

3.3.1 Dependence on energy and bunch length

In the SPS, the beam is accelerated in the SPS from $E_k = 25$ GeV to $E_k = 450$ GeV. For those energies $\beta \approx 1$, so it is γ which changes the most along the acceleration ramp. The longitudinal space charge impedance scales as $\mathrm{Im}\mathcal{Z}/n \propto 1/\gamma^2$ and its amplitude largely decreases during acceleration, as shown in Fig. 3.5. It is reduced by a factor ≈ 10 in the first second when the energy increases from $E_k = 26$ GeV to $E_k = 80$ GeV. Above this energy, the longitudinal space charge is negligible in the SPS. The factor γ is also present in the geometrical factor g, and more specifically in the expression of the transverse bunch size $\sigma_{x,y}$ in Eq. (3.6). The transverse bunch size shrinks during acceleration and the longitudinal space charge impedance slightly increases. Since the transverse bunch size is under the logarithmic function in g its contribution is less effective (see Fig. 3.5).

Concerning the bunch length τ_L, it is not contributing to the space charge impedance but to the induced voltage. Assuming a parabolic line density in the SPS:

$$\begin{aligned} &\lambda = \frac{3}{2\tau_L}\left[1-4\left(\frac{\tau}{\tau_L}\right)^2\right], \\ &\lambda\left(|\tau| > \tau_L/2\right) = 0, \end{aligned} \tag{3.8}$$

then Eq. (3.3) gives:

$$V_{\mathrm{SC}} = \frac{-6qN_b}{\pi f_{\mathrm{rev}}}\frac{\mathrm{Im}\mathcal{Z}}{n}\frac{1}{\tau_L^3}\tau. \tag{3.9}$$

The space charge voltage scales as $V_{\mathrm{SC}} \propto 1/\tau_L^3$, which is another strong dependence on beam parameters. The amplitude of the longitudinal space charge induced voltage can be defined as $|V_{\mathrm{SC}}| = V_{\mathrm{SC}}/\left(2\pi h f_{\mathrm{rev}}\tau\right)$ (with $h = 4620$) to compare with the amplitude of the RF voltage at 200 MHz (linear approximation). It is represented in Fig. 3.6 for a large range of bunch lengths.

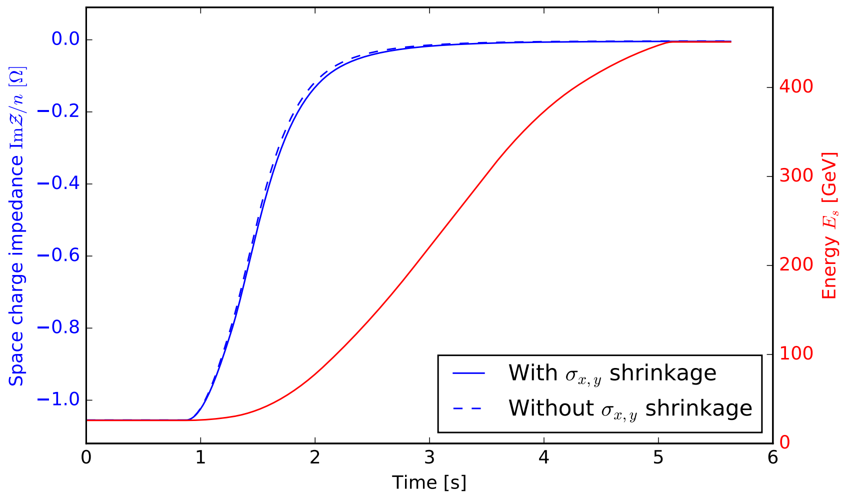

Figure 3.5 – The longitudinal space charge impedance $\mathrm{Im}\mathcal{Z}/n$ (blue), along the energy ramp in the SPS (red). The calculations were done in the Q20 optics, with a normalised transverse emittance $\varepsilon_{x,y} = 1.7\,\mu$m and a momentum spread $\delta_{\mathrm{rms}} = 1.1 \times 10^{-3}$. The solid line corresponds to the calculation with the transverse bunch size shrinkage along the ramp and the dashed line is without this effect.

The dependence on bunch length is significant and the longitudinal space charge induced voltage is not negligible for small bunch lengths. Moreover, high frequency modulations that would be typical for filamenting or unstable bunches would also see high space charge effect, making a dynamic evaluation of space charge effect important in simulations.

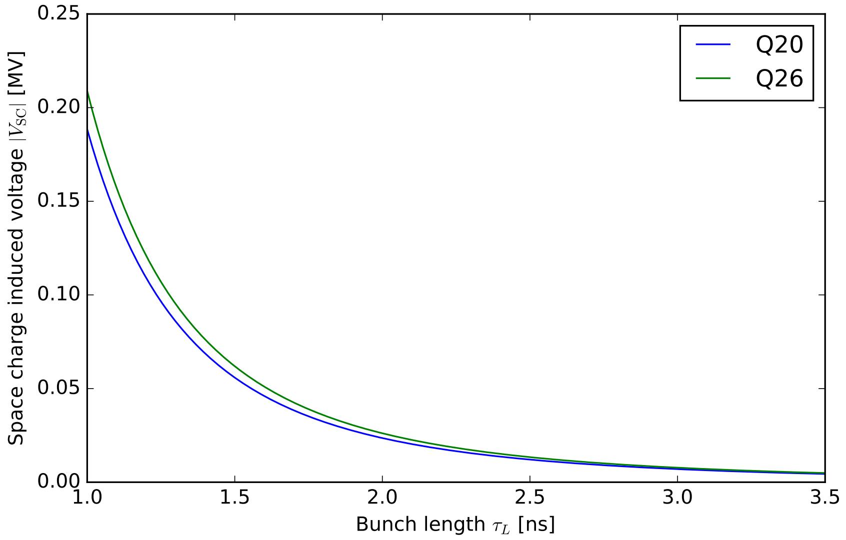

Figure 3.6 – Space charge voltage amplitude $|V_{\mathrm{SC}}|$ as a function of the bunch length τ_L in Q20 (blue) and Q26 (green) optics, calculated using the bunch parameters $N_b = 10^{11}$ ppb, $\varepsilon_{x,y} = 1.7\,\mu$m and $\delta_{\mathrm{rms}} = 1.1 \times 10^{-3}$.

3.3.2 Dependence on the geometrical factor

The changes in the transverse beam parameters affect the geometrical factor g. They are assumed to give small variations because of the logarithmic function. The normalised transverse emittance $\varepsilon_{x,y}$ determines the bunch size $\sigma_{x,y}$. For a stable beam, $\varepsilon_{x,y}$ can be assumed to be constant along the cycle. However, the transverse emittance changes with the beam intensity (see brightness curve in [78]) and may change from one beam type to the other, or due to the beam parameters variation from one cycle to another. The effect of the transverse emittance is shown in Fig. 3.7. For a broad range of ±50% around $\varepsilon_{x,y} = 2\ \mu$m (larger range than the operational one in the SPS), there is a small variation in $\mathrm{Im}\mathcal{Z}/n$ of ±7%.

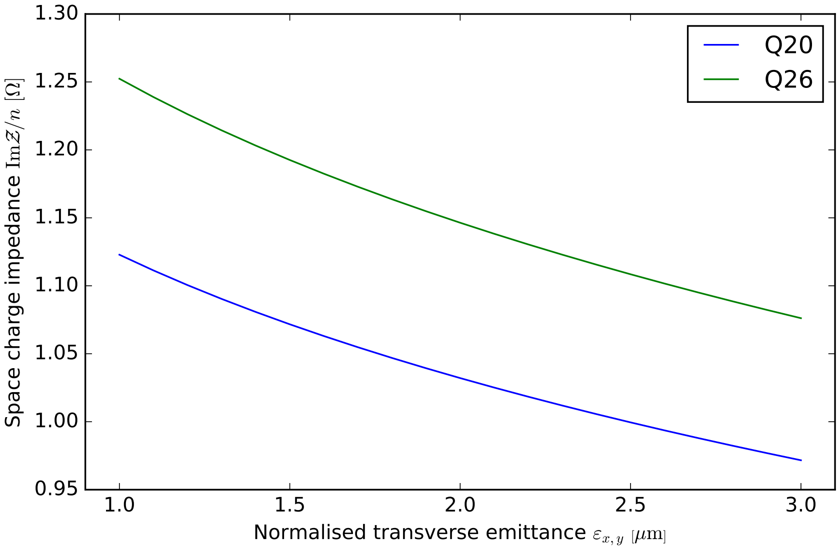

Figure 3.7 – Dependence of the longitudinal space charge impedance $\mathrm{Im}\mathcal{Z}/n$ on the normalised transverse emittance $\varepsilon_{x,y}$, for $\delta_{\mathrm{rms}} = 1.1 \times 10^{-3}$ in both Q20 (blue) and Q26 (green) optics.

The momentum spread δ_{rms} affects the space charge impedance since it increases the bunch size through dispersion. The momentum spread depends on the longitudinal emittance ε_L, and $\delta_{\mathrm{rms}} \propto \sqrt{\varepsilon_L}$ for a fixed RF voltage. The influence of the longitudinal emittance on the longitudinal space charge impedance is shown in Fig. 3.8a. For a large range of longitudinal emittance of ±70% around $\varepsilon_L = 0.21$ eVs (larger range than in the SPS operation), there is a small variation in $\mathrm{Im}\mathcal{Z}/n$ of ±9%. This is small in comparison to the corresponding variation in the space charge induced voltage due to the corresponding change in the bunch length ($V_{\mathrm{ind}} \propto \varepsilon_L^{-3/2}$).

Another parameter that could change the momentum spread is the RF bucket size. For a fixed longitudinal emittance, a change of V_{RF} modifies the momentum spread as $\delta_{\mathrm{rms}} \propto V_{\mathrm{RF}}^{1/4}$. The impact of the RF voltage on the space charge impedance for a fixed longitudinal emittance is shown in Fig. 3.8b. A variation of the RF voltage from 2 MV to 7 MV gives a minor variation of ±3% in the longitudinal impedance. This is small in comparison to the variation in the space charge induced voltage due to the corresponding reduction of the bunch length ($V_{\text{ind}} \propto V_{\text{RF}}^{3/4}$, almost linear with the RF voltage).

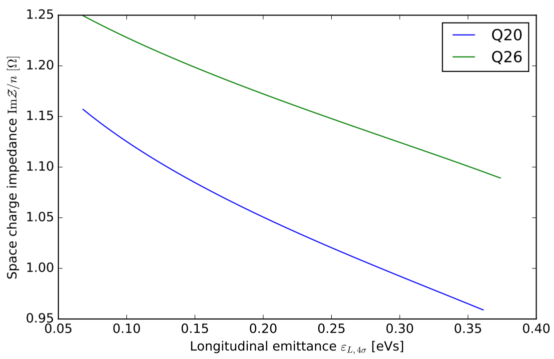

(a) Fixed RF voltage

(b) Fixed longitudinal emittance

Figure 3.8 – Dependence of the longitudinal space charge impedance Im$\mathcal{Z}/n$ on the longitudinal emittance (left), and the RF voltage with a fixed longitudinal emittance (right) at flat bottom.

To have a self-consistent representation of space charge, one should take into account the variations of the geometrical factor g along the cycle iteratively. However, since the dependence of the longitudinal space charge impedance on the beam and RF parameters changing g is small, this effect can be neglected in first approximation.

3.4 Conclusions

The longitudinal space charge impedance Im$\mathcal{Z}/n$ on the SPS flat bottom was computed by taking into account detailed aperture and bunch distribution to compute the geometrical factor g. The space charge impedance in the SPS is Im$\mathcal{Z}/n \approx -1\ \Omega$, and it is ≈ 10% bigger in the Q26 optics than with the Q20 optics.

To precisely simulate the longitudinal space charge effect in tracking codes (such as BLonD), one needs to take into account the changes in γ due to the ramp, and the changes in the bunch profile (τ_L). Concerning g, it can be computed once for a given $\varepsilon_{x,y}$ and δ_{rms}. Any change in the bunch parameters should have a small impact on this initial value and could be neglected. Nevertheless, since g can be computed fast and with a good accuracy from analytical expressions, it can be evaluated at every turn to get a more precise and self-consistent evaluation of the longitudinal space charge effect.

4 Measurement of High Frequency Impedance Sources

4.1 Introduction

One of the instabilities which are critical in the SPS is the "microwave instability" that manifests in the SPS as a fast, uncontrolled longitudinal emittance blow-up above a certain intensity threshold, as shown in Fig. 4.1. This instability is driven by high frequency impedance sources for which:

$$f_r \tau_L \gg 1, \tag{4.1}$$

where f_r is the resonant frequency of the impedance and τ_L is the full bunch length ($4\sigma_{\mathrm{rms}}$ is the case of a Gaussian bunch profile). The 200 MHz Travelling Wave Cavities (TWC) is the main RF system in the SPS used for acceleration, so a typical bunch length in the SPS is $\tau_L \approx (1.5-3.5)$ ns. Then microwave instability could be driven by impedance sources with a resonant frequency above $f_r > 1$ GHz. A fourth-harmonic RF system is available in the SPS and used in bunch-shortening mode to stabilise the LHC beam (by increased Landau damping). However, using this second RF system cannot cure completely this kind of instability [15, 74] which remains a significant limitation for both LHC and AWAKE beams.

The method presented in this chapter consists of measuring the density modulation of long bunches by high frequency impedances, with the RF voltage switched off. This method was used in the past to identify the main impedance sources responsible for microwave instability on the SPS flat bottom. They were the ~ 800 inter-magnet pumping ports [67] which were shielded during the 2000-2001 shutdown, allowing the SPS to reach a higher beam intensity [39]. More recently, investigations were done to identify the new impedance sources limiting the future projects.

First, the high frequency modulation of long bunches with RF off is described. Next, measurement results are presented (for two different SPS optics configurations) which allowed the most important impedance contributions to be identified. Finally, the present SPS impedance model is evaluated by comparison of macroparticle simulations with measurements.

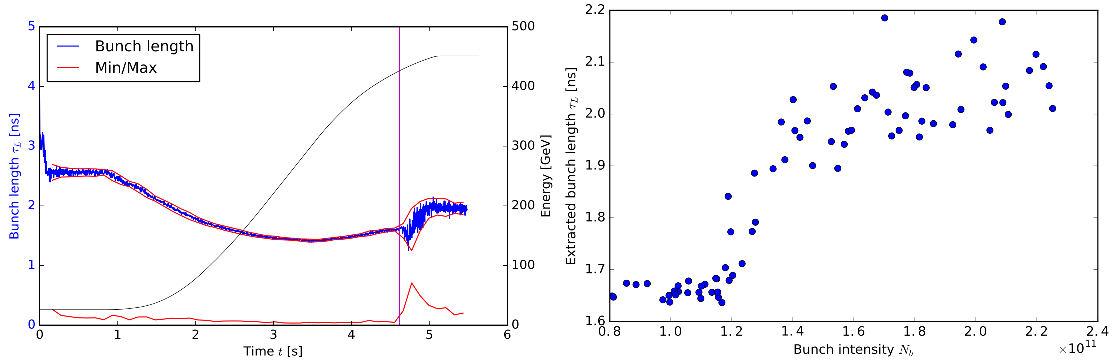

(a) $N_b \approx 1.4 \times 10^{11}$ ppb

(b) Several acquisitions

Figure 4.1 – Longitudinal instability of a single bunch along the accelerating ramp in double RF operation: (a) Example of bunch length during the ramp (the starting time of the instability is represented with the magenta vertical line). (b) The bunch length at the end of the cycle as a function of the bunch intensity N_b for the same injected longitudinal emittance ($\varepsilon_L \approx 0.25$ eVs).

4.2 Microwave instability with RF off

Measurements of the high frequency bunch profile were done on the SPS flat bottom (momentum $p = 26$ GeV/c) with the RF voltage switched off. An example of a measured bunch profile modulation by high frequency impedance sources is shown in Fig. 4.2. To achieve this result, a long bunch was required for which debunching is slow in comparison with the instability. The evolution of the bunch length τ_L during debunching with RF off is given by [79]:

$$\tau_L(t) = \tau_{L0} \left[1 + \left(\frac{t}{t_d}\right)^2\right]^{\frac{1}{2}}, \tag{4.2}$$

where τ_{L0} is the initial bunch length t_d is the debunching time corresponding to:

$$\frac{1}{t_d^2} = \left(\frac{2|\eta|}{\tau_{L0}}\frac{\Delta p_m}{p}\right)^2 + \left(\frac{6N_b q^2 |\eta| \,\mathrm{Im}\mathcal{Z}/n}{\pi E \tau_L}\right)^2, \tag{4.3}$$

where $\eta = \gamma_t^{-2} - \gamma^{-2}$ is the slippage factor (γ_t is the transition Lorenz factor, the SPS is above transition energy for all measurements presented below), $\Delta p_m/p$ is the maximum momentum spread of the bunch, N_b is the bunch intensity, q is the particle charge, $\mathrm{Im}\mathcal{Z}/n$ is the reactive impedance of the machine ($n = f/f_{\mathrm{rev}}$, f is the frequency and f_{rev} is the revolution frequency) and E is the total beam energy. To minimise the debunching, a small momentum spread is required. Note that the dependence on $\mathrm{Im}\mathcal{Z}/n$ of the debunching time with RF off can be used to evaluate the reactive part of the machine impedance [79].

To get a convenient bunch distribution, the RF voltage was adiabatically decreased before extraction in the SPS injector (PS), which gave a bunch length of $\tau_L \approx (25-30)$ ns (more than ten times longer than the usual bunch length in the SPS $\tau_L \approx (1-3)$ ns) together with a small momentum spread $\Delta p_m/p$. In this case, the frequency range of the stable bunch spectrum at injection is low ($f < 100$ MHz) as shown in Fig. 4.2d. Therefore, all the impedance sources in the SPS are located at high frequencies ($f > 100$ MHz) in comparison with the bunch spectrum and lead to microwave-like instability.

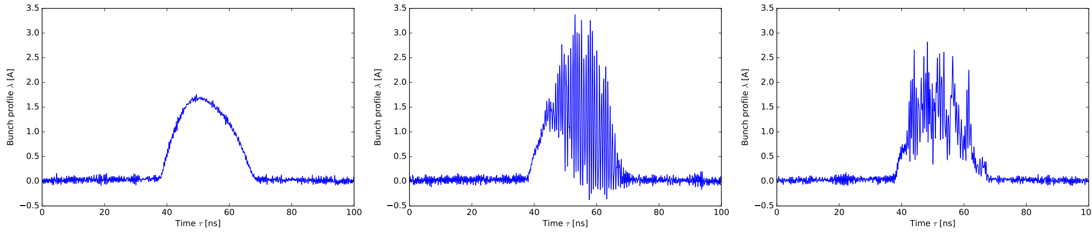

(a) Profile at $t = 0$ ms (b) Profile at $t = 6.23$ ms (c) Profile at $t = 9.24$ ms

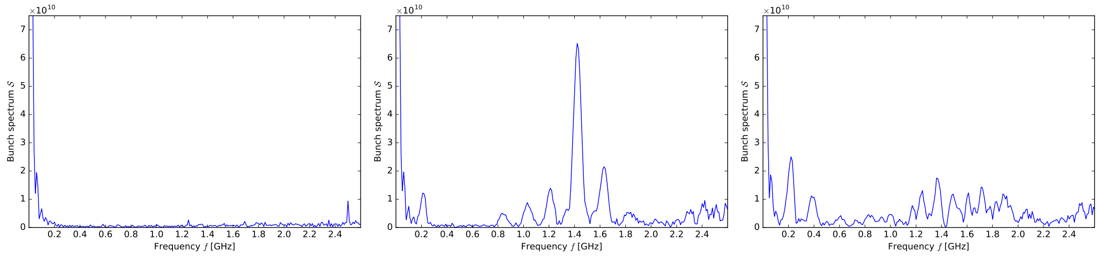

(d) Spectrum at $t = 0$ ms (e) Spectrum at $t = 6.23$ ms (f) Spectrum at $t = 9.24$ ms

Figure 4.2 – Examples of a density modulation of a long bunch at injection in the SPS ($p =$ 26 GeV/c) with the RF voltage switched off in the Q26 optics. The bunch profile (top), together with the corresponding bunch spectrum (bottom) at three different times after injection demonstrating the evolution of the instability.

The fast microwave instability is described by solving the linearised Vlasov equation using the perturbation theory [67]. A distribution ψ in the longitudinal phase space $(\theta, \Delta E)$ is considered, where $\theta = \omega_{\mathrm{rev}}\tau$ is the azimuthal coordinate of a particle in the ring, $\omega_{\mathrm{rev}} = 2\pi f_{\mathrm{rev}}$ is the revolution angular frequency, τ is the longitudinal coordinate of the particle in time and ΔE the relative energy of a given particle with respect to the total beam energy E. The bunch profile for the bunch distribution ψ is noted $\lambda(\theta)$ and the corresponding bunch spectrum $\mathcal{S}(f)$. The bunch distribution is composed of an unperturbed part ψ_0 and a perturbation ψ_1, for which the spectra are respectively:

$$\mathcal{S}_0(n) = \frac{1}{2\pi}\int_{-\pi}^{\pi}\left[\int_{-\infty}^{\infty}\psi_0(\theta, \Delta E)\, d(\Delta E)\right] e^{-jn\theta}\, d\theta, \tag{4.4}$$

$$\mathcal{S}_1(n) = \frac{1}{2\pi} e^{-j\Omega t}\int_{-\pi}^{\pi}\left[\int_{-\infty}^{\infty}\psi_1(\theta, \Delta E)\, d(\Delta E)\right] e^{-jn\theta}\, d\theta, \tag{4.5}$$

where Ω is the oscillation frequency of the perturbation, of which the imaginary part gives the growth rate of the instability, and the terms in square brackets are the unperturbed/perturbed bunch profiles $\lambda_{0,1}(\theta)$. Since the momentum spread is small, the debunching is slow and the unperturbed bunch spectrum can be considered stationary. The stationary bunch spectrum corresponds to the contribution at low frequencies ($f < 100$ MHz), while the perturbation corresponds to the time dependent modulations at high frequencies ($f > 100$ MHz).

With the RF voltage switched off, the particle motion is only affected by the induced voltage:

$$V_{\text{ind}}(\theta) = -qN_b\,\omega_{\text{rev}}\sum_n \left[\mathcal{S}_0(n) + \mathcal{S}_1(n)\right]\mathcal{Z}(n)\,e^{jn\theta}. \tag{4.6}$$

The bunch interacts with impedance sources, which in most of the cases can be described by the resonator model:

$$\mathcal{Z}(f) = \frac{R_s}{1 + jQ\left(\frac{f}{f_r} - \frac{f_r}{f}\right)}, \tag{4.7}$$

where R_s is the shunt impedance and Q the quality factor determining the decay time of the wake. For the high frequencies under consideration $f_r\tau_L \gg 1$, the induced voltage coming from the stationary bunch spectrum $\mathcal{S}_0$ in Eq. (4.6) is negligible. Therefore, the linearised Vlasov equation can be expressed as:

$$\frac{\partial\psi_1}{\partial t} + \frac{\left(q\omega_{\text{rev}}\right)^2}{2\pi}N_b\left[\sum_n \mathcal{S}_1(n)\,\mathcal{Z}(n)\,e^{jn\theta}\right]\frac{\partial\psi_0}{\partial(\Delta E)} + \frac{\eta\omega_{\text{rev}}}{\beta^2 E}\Delta E\frac{\partial\psi_1}{\partial\theta} = 0. \tag{4.8}$$

For bunches with small energy spread, during the linear stage of the instability, the injected bunch distribution can be treated as mono-energetic with $\psi_0(\theta, \Delta E) = \lambda(\theta)\,\delta(\Delta E)$, where δ is the Dirac function. Solving the linearised Vlasov equation with this assumption leads to the matrix equation:

$$\mathcal{S}_1(n) = -j\frac{\eta\omega_{\text{rev}}}{2\pi E}\left(\frac{q\omega_{\text{rev}}}{\Omega}\right)^2 n\sum_{n'}\mathcal{S}_0\left(n - n'\right)\mathcal{Z}\left(n'\right)\mathcal{S}_1\left(n'\right). \tag{4.9}$$

For narrow-band impedance sources (with the bandwidth $\Delta\omega_r = \omega_r/(2Q) \ll 1/\tau_L$), the bunch spectrum is assumed constant over the impedance width with $\mathcal{S}_0\left(n - n'\right) \approx \mathcal{S}_0(n - n_r)$ where $n_r = f_r/f_{\text{rev}}$. In this case the spectrum of the unstable mode is:

$$\mathcal{S}_1 \sim n\mathcal{S}_0(n - n_r) \sim ne^{-\frac{\sigma_{\text{rms}}^2(n-n_r)^2}{2}}, \tag{4.10}$$

where $1/\sigma_{\text{rms}}$ is the bandwidth of the stationary spectrum $\mathcal{S}_0$. This also defines the bandwidth of the unstable mode, which implies that a longer bunch gives a better resolution to the measured modulation. Note that the peak is shifted by $1/\left(n_r\sigma_{\text{rms}}^2\right)$ with respect to n_r, which will be shown in Section 4.4.

Finally, the growth rate of the instability is:

$$\mathrm{Im}\Omega \approx 2\pi f_r \left(\frac{q^2 N_b \omega_{\mathrm{rev}} \eta}{16\pi E} \frac{R_s}{Q} \right)^{\frac{1}{2}} . \tag{4.11}$$

The bunch profile modulation is mainly driven by impedance sources with high R_s/Q and high resonant frequency f_r. Note also the dependence on the slippage factor η that is relevant in the following discussion of results for the Q20 and Q26 optics.

4.3 Measurements

4.3.1 Setup

To measure the time dependence of the high frequency modulation, the bunch profile $\lambda(\tau)$ was measured at regular time interval using a Wall Current Monitor (WCM) and the corresponding bunch spectrum $\mathcal{S}(f)$ was obtained using a Fast Fourier Transform (below the bunch spectrum is normalised to the bunch intensity). The perturbations of the measured bunch spectrum due to the various elements in the measurement line (e.g. cables) were corrected [72]. This correction is effective up to ≈ 2.0 GHz. Above this frequency, the amplitude of the corrected bunch spectrum may be overestimated. Below, the frequency range $0.1\ \mathrm{GHz} < f < 2.0\ \mathrm{GHz}$ is considered.

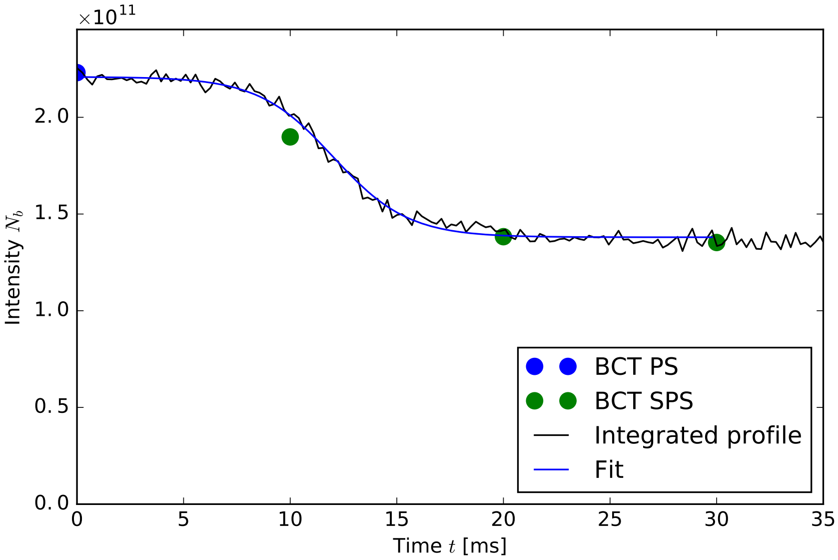

Figure 4.3 – The bunch intensity N_b during the acquisition corresponding to Fig. 4.2 (Q26 optics). The bunch intensity was measured with a BCT at extraction from the PS (blue dot) and during acquisition in the SPS (green dots). The intensity is evaluated from the measured bunch profile and scaled to the measured intensity from PS (black), and fitted with a sigmoid function to be used in macroparticle simulations (blue).

Measurements were done for a broad range of bunch intensities N_b, which was measured using a DC Beam Current Transformer (BCT) at the extraction time in the PS and during the acquisition in the SPS. Since the integration time of the BCT is long (10 ms) with respect to the measurement time scale (30 ms), the remaining information about the bunch intensity was obtained by integrating the measured bunch profiles, as shown in Fig. 4.3.

Two optics parameters are available in the SPS named Q20 and Q26 after the transverse tune. These are characterised by different transition Lorentz factors ($\gamma_{t,\mathrm{Q20}} \approx 18$ and $\gamma_{t,\mathrm{Q26}} \approx 22.8$), resulting in a slippage factor η that is 2.9 times higher for the Q20 optics than in the Q26 optics. Therefore, the debunching is also faster for the Q20 optics (see Eq. (4.3)) and measurements were done on a different time scale: over 600 turns in the machine for the Q20 optics and 1000 turns for the Q26 optics (the revolution period is $T_{\mathrm{rev}} \approx 23.1\ \mu\mathrm{s}$). On these time scales, the debunching is considered small.

According to Eq. (4.11), the growth rate of the bunch profile modulation is faster in the Q20 optics with respect to the Q26 optics. This was also observed in measurements where the bunch modulation is happening at a time scale $\sqrt{\eta_{\mathrm{Q20}}/\eta_{\mathrm{Q26}}} \approx 1.7$ faster in the Q20 optics, as shown in the upper plots of Fig. 4.4 (for same bunch intensity $N_b \approx 2.1 \times 10^{11}$ ppb). However, a higher slippage factor also implies a faster debunching which smears the modulation. Therefore, the intensity threshold was higher in the Q20 optics and measurements were done in a different intensity range, $N_b \approx (1.3-3.5) \times 10^{11}$ ppb in the Q20 optics and $N_b \approx (0.4-2.5) \times 10^{11}$ ppb in the Q26 optics.

Note that fast losses (within less than 1000 turns) were observed for high bunch intensities, as shown in Fig. 4.3, and at a lower intensity threshold in the Q26 optics. This may be the sign of possible transverse instabilities. Most of the modulations are taking place in a time scale smaller than the one of the intensity loss. Additionally, it is assumed for this study that there is no coupling of the transverse particle motion onto the longitudinal one.

4.3.2 Data analysis

For each acquisition, the projected spectrum $\mathcal{S}_{\mathrm{proj}}(f)$ corresponding to the maximum value of the mode amplitude of $\mathcal{S}(f)$ along the time axis was used. Examples are shown in Fig. 4.4, where the evolution of the spectrum with time is represented in the upper plot and the corresponding projection is shown below. In these examples the dominant modulations (peaks) are those at 1.4 GHz and 200 MHz. Smaller peaks at 1.2 GHz and 1.6 GHz are also visible.

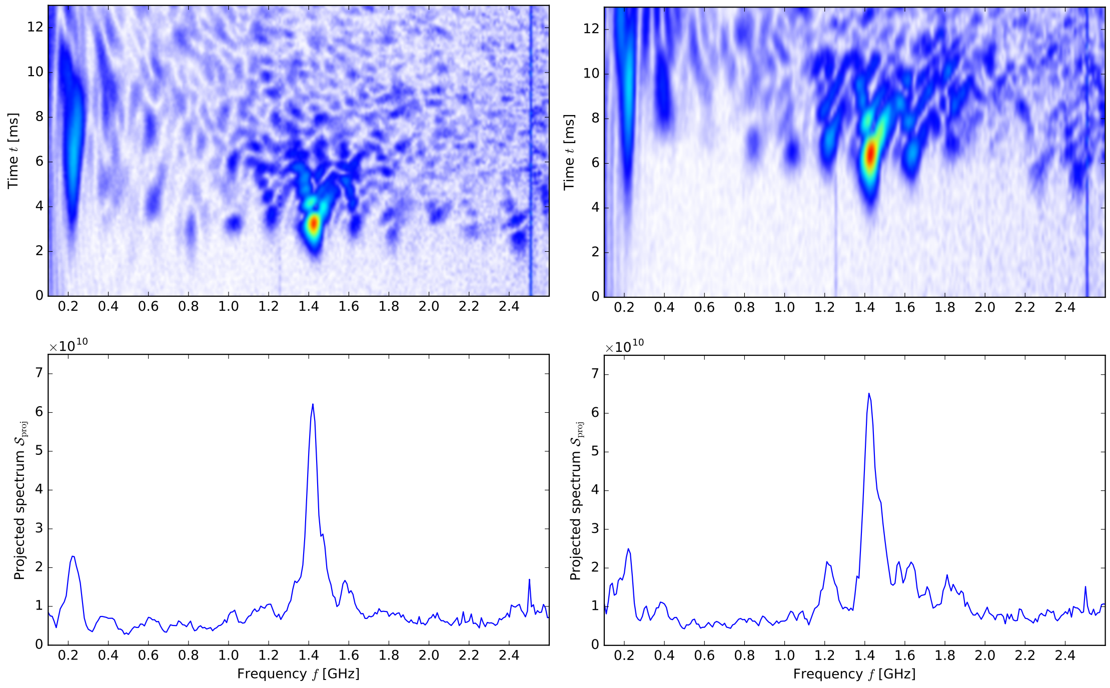

(a) Q20 optics

(b) Q26 optics

Figure 4.4 – Examples of the evolution of the bunch spectrum with time after injection (top) and the corresponding projected spectrum (bottom) in the Q20 (left) and Q26 (right) optics, for an injected bunch intensity $N_b \approx 2.1 \times 10^{11}$ ppb. The acquisition in the Q26 optics corresponds to the example shown in Fig. 4.2.

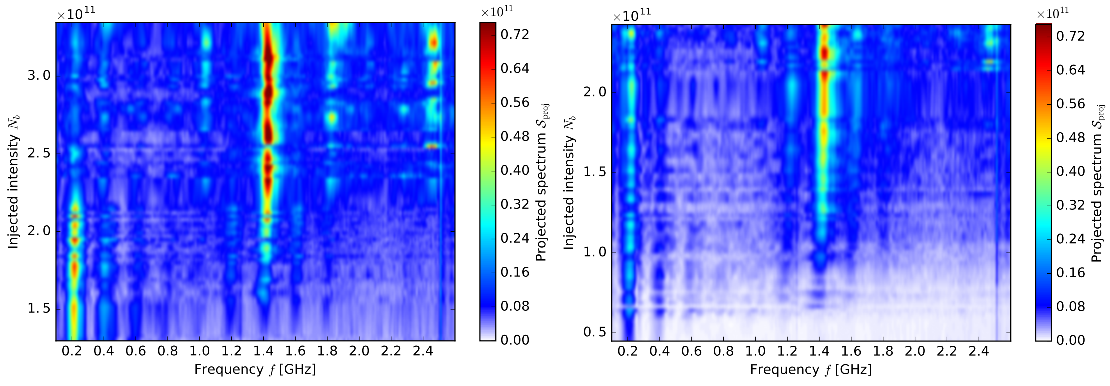

(a) Q20 optics

(b) Q26 optics

Figure 4.5 – Projected spectra as a function of intensity in Q20 (left) and Q26 (right) optics. The colour scale corresponds to the amplitude of the projected spectrum.

In Fig. 4.5, the measured maximum spectra are presented as a function of the injected bunch intensity. All the vertical lines correspond to modulations that may be associated to a possible impedance source. The most straightforward for identification is the modulation at 200 MHz corresponding to the main impedance of the TWC RF system, which has the highest resistive impedance in the machine. However, the most significant modulation is the one at 1.4 GHz both in the Q20 and Q26 optics. When these measurements were done, the responsible impedance source was still unknown. It was identified later, after a thorough survey of the SPS elements [40] to be the QF-type vacuum flanges. The vacuum flanges are indeed the biggest impedance source in terms of R_s/Q at high frequencies in the present SPS impedance model and are expected to be the main source of microwave instability. Another peak, present in both optics, is located at 2.45 GHz and can be associated with the impedance of the QD-type vacuum flanges. They do not have the highest impedance in terms of R_s/Q, but still can generate a significant modulation due to their high resonant frequency f_r, according to Eq. (4.11). However, as discussed in the Section 4.3.1, the correction of the measurement line transfer function may give an overestimation of the spectrum above 2 GHz. Therefore, although this peak is present its absolute amplitude may not be accurate.

Close to the peak at 1.4 GHz, other lines are present at multiples of main RF frequency ($f \approx 200$ MHz): at 1.2 GHz and 1.6 GHz in the bunch intensity range $(1.5-2.0)\times 10^{11}$ ppb, and at 1.0 GHz and 1.8 GHz for bunch intensities above 2.3×10^{11} ppb. All these peaks can be associated with various resonant frequencies of the QF-type and QD-type vacuum flanges impedance, except the one at 1.0 GHz where no major contribution was identified. However, these peaks are correlated to the main ones at 200 MHz, 1.4 GHz and 2.45 GHz. For instance, the lines at 1.2 GHz and 1.6 GHz are correlated with both peaks at 200 MHz and 1.4 GHz. Concerning the lines at 1.0 GHz and 1.8 GHz, they are correlated with the peaks at 1.4 GHz and 2.45 GHz. Therefore, these smaller peaks can be non-linear products of the main modulations and may not be caused by any impedance source. Another feature is the absence of peak corresponding to the TWC at 800 MHz. Despite its high R_s/Q, it appears to be located at the resonant frequency f_r that is too small to drive a modulation in competition with other impedances. This implies that some significant impedance sources may not be identified with this method.

It is possible to estimate the values of R_s/Q using Eq. (4.11) from the instability growth rate measured well above the instability threshold. An example is shown in Fig. 4.6 for an acquisition made in the Q20 optics for a bunch intensity $N_b \approx 2.7\times 10^{11}$ ppb and for the signal growing at 1.4 GHz. The initial phase of the instability can be described by the linear theory with the exponential signal growth. With the increase of the momentum spread the instability saturates due to non-linearities. The calculated growth rate depends on the time scale taken for the fit, and due to the quadratic dependence of the calculated R_s/Q on $\mathrm{Im}\Omega$, results may change with a variation of approximately ±20% (see Fig. 4.6). In addition, the shot-to-shot variation (from one acquisition to another) leads to significant error-bars. The calculated values of the impedance from the growth rate are $R_s/Q \approx (5\pm 3)$ kΩ for the Q20 optics and $R_s/Q \approx (7\pm 3)$ kΩ for the Q26 data. On average these values are in good agreement with the ones obtained from electromagnetic simulations and measurements for the QF-type vacuum flanges which have two main resonances: $R_s/Q \approx 6$ kΩ at 1.415 GHz and $R_s/Q \approx 1.8$ kΩ at 1.395 GHz [33].

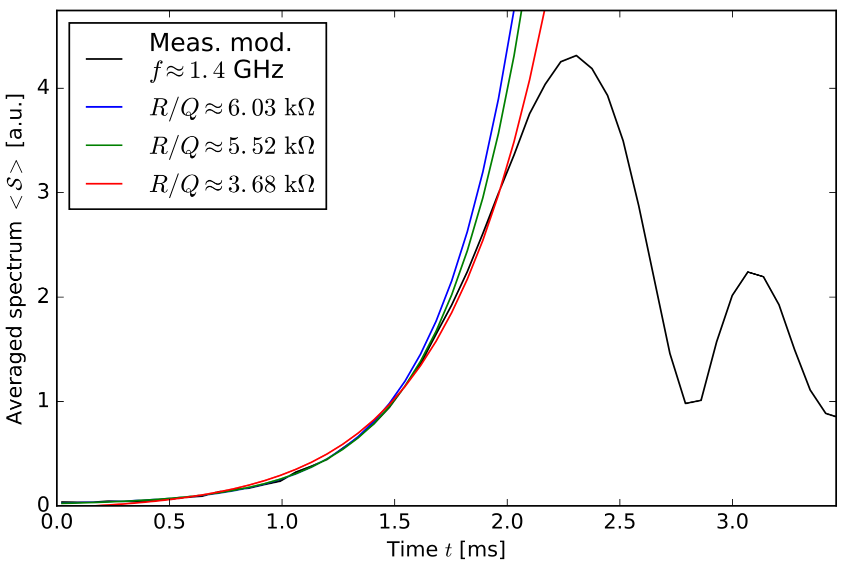

Figure 4.6 – The measured spectrum amplitude $<\mathcal{S}>$ averaged over a bandwidth of ±50 MHz around 1.4 GHz during the initial phase of the instability in the Q20 optics for $N_b \approx 2.7 \times 10^{11}$ ppb (black). The growth of the instability on the early stage was fitted using an exponential function for a time: $t_{\rm fit}$ = 1.4 ms (blue), $t_{\rm fit}$ = 1.6 ms (green) and $t_{\rm fit}$ = 2.0 ms (red). The corresponding value of R_s/Q is computed using using Eq. (4.11).

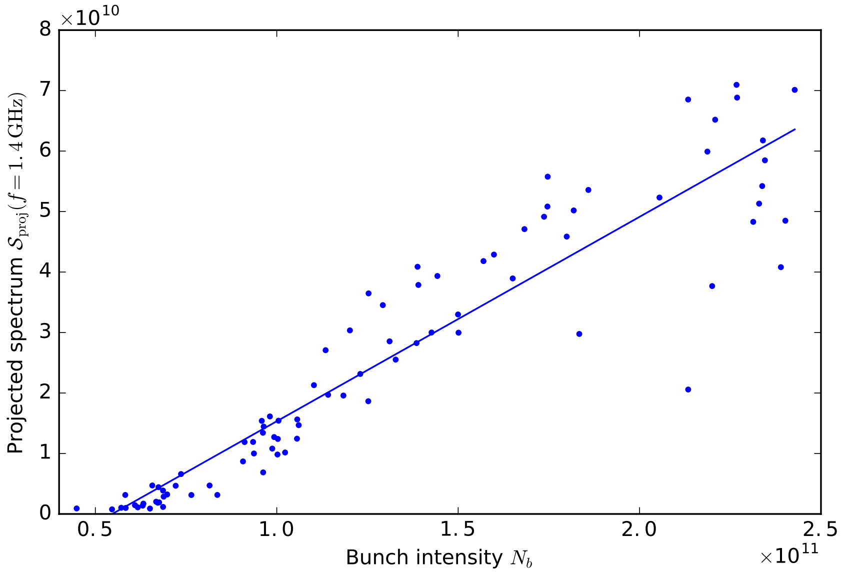

Figure 4.7 – Maximum spectrum at 1.4 GHz as a function of the bunch intensity N_b in the Q26 optics. Measurements are fitted linearly and $b_{\rm peak}$ is the slope of the fit.

The measured maximum amplitude of the projected spectrum $\mathcal{S}_{\rm proj}$ is a more convenient parameter for comparison with results of macroparticle simulations. The results shown in Fig. 4.5 are simplified by fitting the peaks as a function of the bunch intensity N_b (comparisons of 2D plots are easier than 3D plots). An example is shown in Fig. 4.7, where the peak at

1.4 GHz for the results in the Q26 optics are fitted linearly as a function of intensity. The slope of the linear fit is noted b_{peak} (shortened to slope b_{peak} below). This is done for each frequency, and the results are shown in Fig. 4.8. All the peaks discussed above at multiples of 200 MHz are visible in Fig. 4.8. Note that the slope b_{peak} at 200 MHz is negative in the Q20 optics, due to the fact that this peak is present only for small bunch intensities (see Fig. 4.5a). This definition will be used for comparison with macroparticle simulations in Section 4.4.

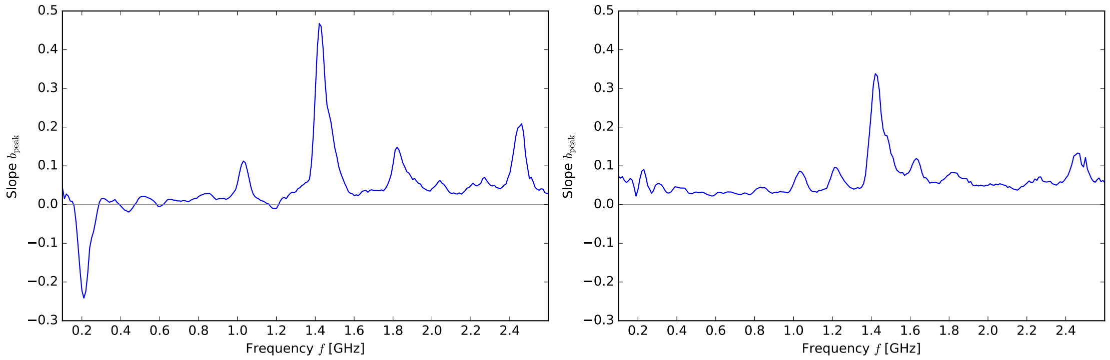

(a) Q20 optics

(b) Q26 optics

Figure 4.8 – The slope b_{peak} as a function of frequency for the Q20 (left) and Q26 (right) optics. The value of the slope at 1.4 GHz in the plot (b) correspond to the example shown in Fig. 4.7 with $b_{\mathrm{peak}} \approx 0.34$.

A by-product that can be extracted from these measurements is the bunch energy loss in the absence of RF voltage. The bunch energy loss due to the resistive machine impedance is given by [18]:

$$\delta E_b = -\frac{\left(qN_b\right)^2 \omega_{\mathrm{rev}}}{\pi} \sum_{n=0}^{\infty} \mathrm{Re}\mathcal{Z}\left(n\right) \left|\mathcal{S}\left(n\right)\right|^2. \tag{4.12}$$

In the present configuration, the loss rate also depends on the unstable bunch spectrum, which is sampling the high frequency impedance sources driving the instability. The bunch profile is measured by the Wall Current Monitor with a regular time interval corresponding to a fixed number of turns in the ring. Assuming that the acquisition frequency stays constant and is initially well adjusted to the revolution frequency f_{rev}, the position of the bunch centre of mass μ_{rms} stays constant (μ_{rms} is obtained here from the rms bunch position calculated from the line density). With the RF voltage switched off, the energy loss manifests through a drift in time of the bunch position μ_{rms}. Since measurements are done above transition energy in the SPS, the revolution frequency of the bunch gradually increases while the bunch loses energy. Therefore the bunch position μ_{rms} decreases with time as shown in Fig. 4.9.

To analyse the bunch energy loss as a function of the bunch intensity, the bunch position drift $\Delta\mu_{\mathrm{rms}}$ during the time acquisition time Δt (600 turns in the Q20 optics and 1000 turns in the Q26 optics) is taken. The measured bunch position drift as a function of the bunch intensity is shown in Fig. 4.10. For zero bunch intensity, the bunch position drift should be zero since the bunch would not lose energy and its revolution period would remain constant. Due to the momentum spread, only a slow debunching would be observed. For the measurements in the Q20 optics in Fig. 4.10a, there is an offset in $\Delta\mu_{\mathrm{rms}}$ for small intensities, which can be explained by a small mismatch in the initial bunch energy with respect to the expected one at injection. In Section 4.4, these results will be compared with macroparticle simulations to test the energy loss due to the effective resistive impedance of the machine.

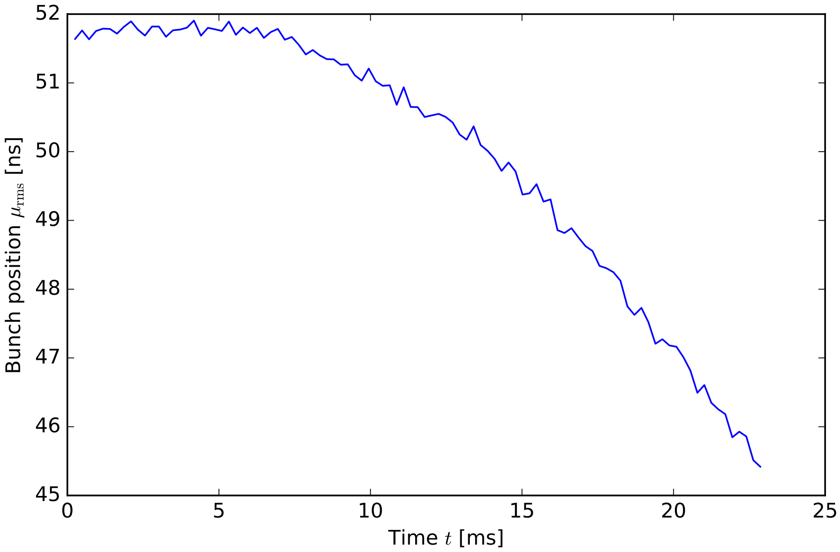

Figure 4.9 – Bunch position μ_{rms} drift with time during the acquisition due to the energy loss corresponding to the acquisition in Fig. 4.2 in the Q26 optics and a bunch intensity $N_b \approx 2.1 \times 10^{11}$ ppb.

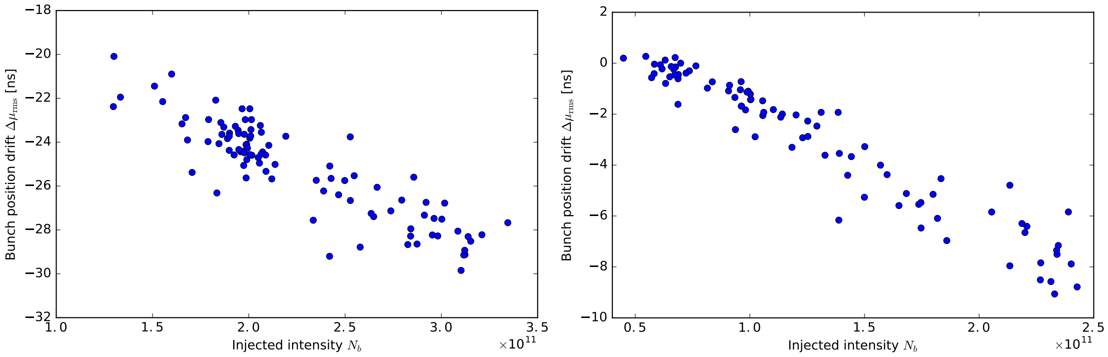

(a) Q20 optics (b) Q26 optics

Figure 4.10 – The measured bunch position drift $\Delta\mu_{\mathrm{rms}}$ as a function of the injected bunch intensity N_b in the Q20 (left) and Q26 (right) optics, respectively after 600 and 1000 turns.

4.4 Particle simulations

4.4.1 BLonD simulations

To be able to extract more accurate information from the measurements presented above, macroparticle simulations were done taking into account the non-linear effects and a more realistic bunch distribution in energy. The simulation code BLonD [45] was used including the present impedance model shown in Fig. I.3. The SPS machine parameters were set in the simulations to match the ones in measurements. To cover the same range in bunch intensity and injected bunch length, each acquisition was reproduced in simulations. The initial macroparticle distribution was generated along the longitudinal and the momentum coordinates independently. This was done in order to generate exactly the same bunch profiles as in measurements since the instability growth depends on the overlap of the bunch spectrum and the high frequency impedance. As discussed in Section 4.3.1, the correction of the measurement line transfer function includes some un-physical noise above 2 GHz. Therefore, the input bunch profile was smoothed using a Chebyshev filter (type 2) with the cut-off frequency set at 2.0 GHz.

The particle distribution in momentum was generated using a parabolic function with the expected rms momentum spread $\Delta p_m / p$ (corresponding to the bunch length τ_L) and assuming that in the PS before extraction the bunch was matched to the RF bucket with intensity effects. To take into account the effect of the potential-well distortion in the PS, a constant reactive impedance with $\mathrm{Im}\mathcal{Z}/n = 18.4\ \Omega$ [63] was assumed. In each simulation, the bunch intensity was set taking into account the realistic losses estimated by using a fit to the measured intensity as shown in Fig. 4.3.

The analysis of simulation results was done using the same method as for measurements and results are shown in Fig. 4.11. The peak at 1.4 GHz due to the impedance of the QF-type vacuum flanges is reproduced both in the Q20 and Q26 optics. The intensity threshold of this instability is in excellent agreement with the measurements ($N_{\mathrm{th,Q20}} \approx 2.2 \times 10^{11}$ ppb and $N_{\mathrm{th,Q26}} \approx 1.0 \times 10^{11}$ ppb), as well as the slopes b_{peak} for the Q26 optics. Note the absence of modulation at 800 MHz from the TWC RF system at this frequency, like in measurements. An interesting observation is that the position of the peaks are not exactly centred in 200 MHz and 1.4 GHz, but slightly off-setted at higher frequencies (about 20 MHz). However, the input parameters of the impedance sources of the main RF system and the QF-type vacuum flanges are well centred at 200 MHz and 1.4 MHz. This was expected from Eq. (4.10), where it was shown that the centre of the unstable spectrum should be shifted by $1/\left(n_r \sigma_{\mathrm{rms}}^2\right)$. This shift is also present in measurements (see Fig. 4.5).

Deviations between measurements and simulations in the slope b_{peak} can be noticed. The slope b_{peak} at 1.4 GHz for the Q20 optics is lower in amplitude than in measurements. Moreover, the various peaks are in competition with each other. A side-effect of the too low peak at 1.4 GHz is that the peak at 200 MHz is not reduced at high intensities in simulations. Concern-

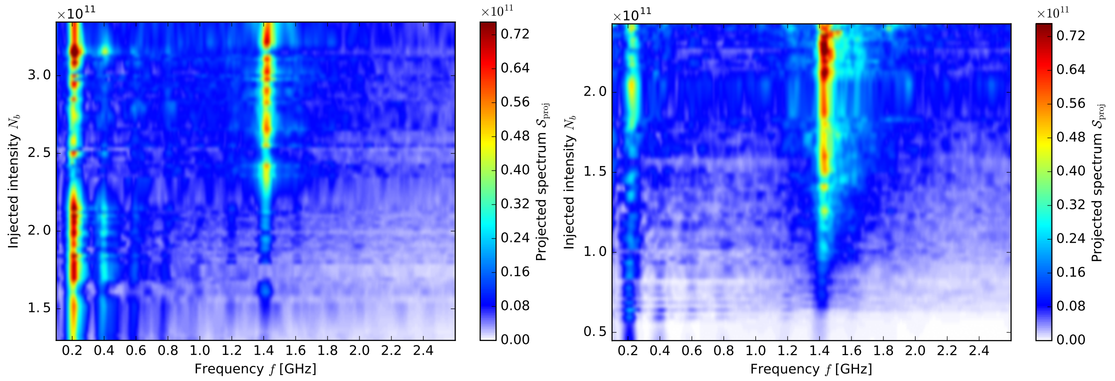

(a) Q20 optics (b) Q26 optics

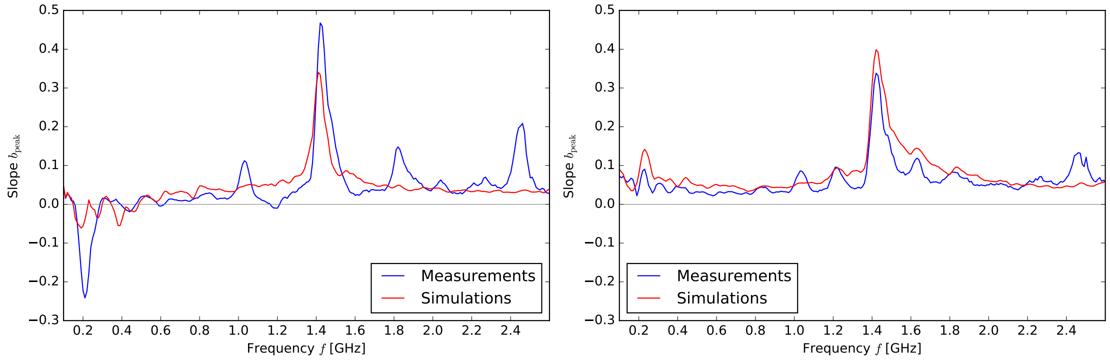

(c) Q20 optics (d) Q26 optics

Figure 4.11 – Projected spectra $\mathcal{S}_{\text{proj}}$ from simulations as a function of intensity (top), and the corresponding slope b_{peak} as a function of frequency (bottom) for both Q20 (left) and Q26 (right) optics. The simulated slopes b_{peak} in red are compared with the measured ones in blue.

ing the peaks at multiples of 200 MHz around 1.4 GHz, they are barely visible in the Q26 optics simulations since they are below the noise background and are absent in simulations for the Q20 optics.

The bunch position drift due to the energy loss discussed above was also calculated in simulations and results are shown in Fig. 4.12. For the Q26 optics, the bunch position drift in simulations is in excellent agreement with the measurements. For the Q20 optics, an energy mismatch of −20 MeV is required in simulations to get the same offset as in the measured bunch position drift $\Delta\mu_{\text{rms}}$ for low intensities. Above the intensity threshold for the peak at 1.4 GHz ($N_{\text{th,Q20}} \approx 2.2 \times 10^{11}$ ppb), the bunch position drift deviates from the measured one.

The main goal of these measurements was to identify impedance sources that could drive microwave instabilities, which has been achieved. Indeed, the measured modulation at 1.4 GHz was identified to be driven by the impedance of the QF-type vacuum flanges and the effect was reproduced in simulations, implying that the evaluation of the impedance in terms of R_s/Q is reasonable. This is further supported by the good agreement in the measured

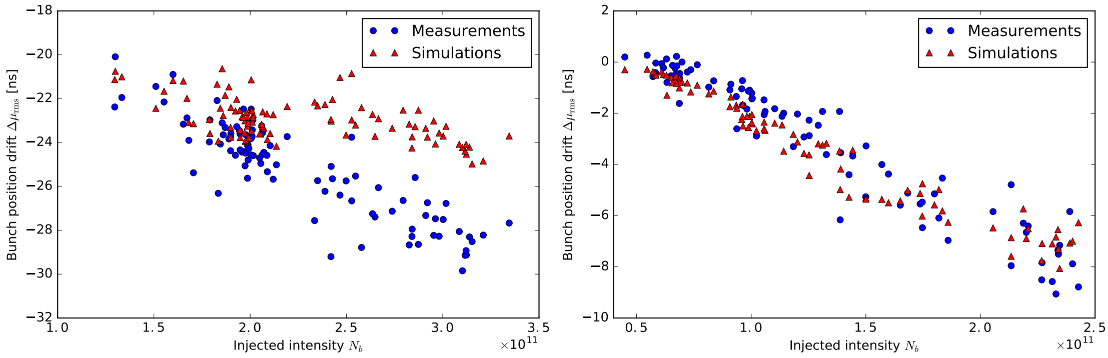

(a) Q20 optics (b) Q26 optics

Figure 4.12 – The simulated (red) bunch position drift $\Delta\mu_{\rm rms}$ compared with the measured one (blue) in the Q20 (left) and the Q26 (right) optics.

and simulated bunch position drifts in the Q26 optics. Concerning the Q20 optics, the main peaks are also reproduced but with some non-negligible deviations. Since the time scale of the development of the instability and of debunching is very short, small differences in the initial particle distribution between measurements and simulations could lead to a significant discrepancy in results. Therefore, the initial bunch distribution was varied to investigate the origin of the deviations.

4.4.2 Effect of the initial bunch distribution

In simulations, to generate the distribution in momentum, the bunch was assumed to be matched to a PS non accelerating RF bucket modified by the induced voltage from a constant reactive impedance $\mathrm{Im}\mathcal{Z}/n$. However, some beam manipulations done in the PS just before extraction may change the shape of the RF bucket (e.g. extraction bump). This implies that the momentum spread may be lower than the previous estimation. Additionally, the resistive part of the PS impedance was neglected, although it should also reduce the previous estimation of the momentum spread for a given bunch length. With these assumptions, the momentum spread was reduced by ≈ 10% to evaluate what would be the effect on the instability, and results are shown in Fig 4.13. A better agreement with measurements is reached in the Q20 optics for the peak at 1.4 GHz with this condition, without affecting the results in the Q26 optics.

For the simulations presented above, the bunch profile was smoothed above 2 GHz to remove the un-physical noise added from the correction of the measurement line transfer function (see Section 4.4.1). Therefore, the effect of the impedance sources above $f > 2$ GHz was significantly reduced in simulations and could not be reproduced the peak in measurements at 2.45 GHz. To evaluate the impact of high frequency impedance sources, simulations were done keeping the high frequency noise and with the reduction of the momentum spread. Results are shown in Fig. 4.14. A peak driven in simulations by the impedance of the QD-

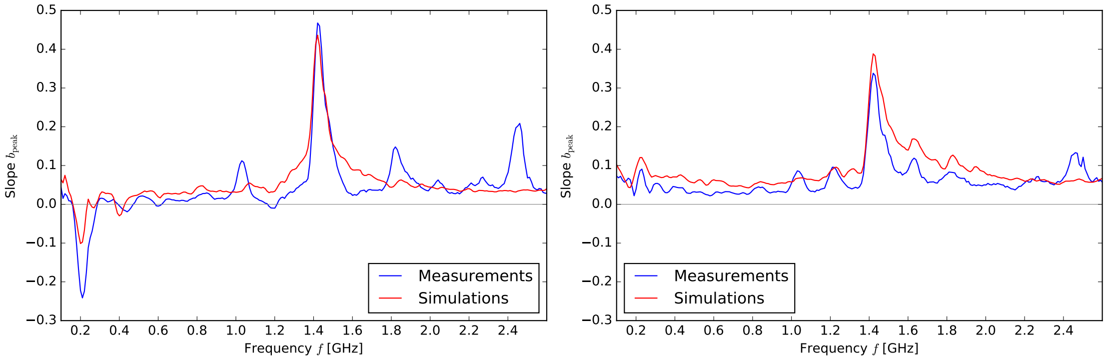

(a) Q20 optics (b) Q26 optics

Figure 4.13 – The simulated slope b_{peak} (red) compared to the measured one (blue) in the Q20 (left) and the Q26 (right) optics, with a reduction of the initial bunch momentum spread $\Delta p_m / p$ by ≈ 10% with respect to the spread used in simulations shown in Fig. 4.8.

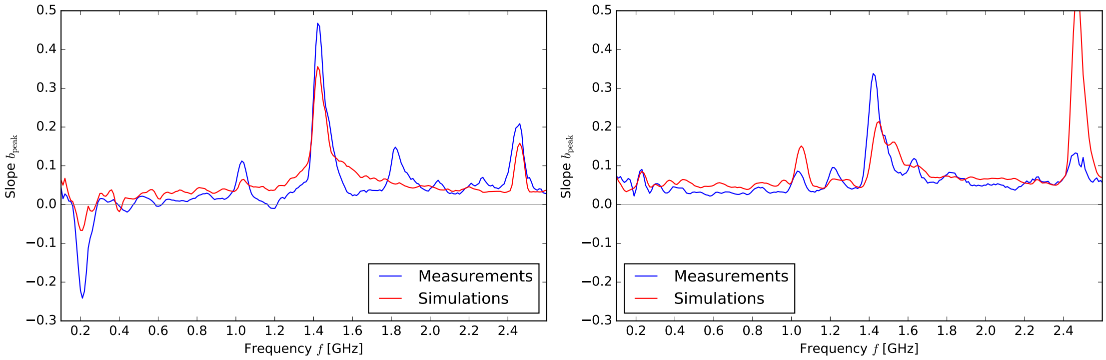

(a) Q20 optics (b) Q26 optics

Figure 4.14 – The simulated slopes b_{peak} (red) using an initial bunch profile with non-filtered noise above 2 GHz and a reduced momentum spread $\Delta p_m / p$ with respect to the simulations shown in Fig. 4.11, compared to the measured one (blue) in the Q20 (left) and Q26 (right) optics.

type vacuum flanges at 2.45 GHz like in measurements. However, the amplitude of the slope b_{peak} at 2.45 GHz is much higher in simulations than in measurements, implying that the initial high frequency noise in the bunch spectrum is indeed overestimated. Nevertheless, the peak at 2.45 GHz can still be associated to the impedance of the QD-type vacuum flanges. Moreover, an interesting result is the peak at 1.0 GHz appearing in simulations only with the presence of the modulation at 2.45 GHz for the Q26 optics. The same result was obtained in the Q20 optics simulations by further reducing the momentum spread $\Delta p_m / p$ of the initial distribution by 10%. There is no major impedance source at 1 GHz in the SPS impedance model used in macroparticle simulations. Therefore this peak in the bunch spectrum is the non-linear product of the modulation of the bunch profile at several different frequencies. This implies that not all peaks measured with this method are driven by impedance sources, and this may be applicable to the other peaks at multiples of 200 MHz around 1.4 GHz. Finally, the peak at 1.8 GHz in the Q20 optics (see Fig. 4.14a) was also never reproduced in simulations regardless of the initial bunch distribution. This may indicate that some additional impedance source may still not be identified or the present one (from the QD-type vacuum flanges) is underestimated in the present SPS impedance model. The impedance R_s/Q of the impedance at 1.8 GHz is nonetheless expected to be a small contribution in comparison to the QF-type vacuum flanges main resonance at 1.4 GHz.

The bunch position drift $\Delta\mu_{\mathrm{rms}}$ was calculated again from simulations done with a smaller momentum spread and the un-filtered noise in the bunch profile above 2 GHz, and results are shown in Fig 4.15. A better agreement with measurements is reached for the Q20 optics, due to the larger energy loss caused by the stronger overlap between the unstable bunch spectrum and the resistive impedance during the instability. Some deviations between measurements and simulations are still present above 2.3×10^{11} ppb and indicate that the modulation at 1.8 GHz missing in simulations and driven by an impedance source yet to be identified may contribute to the energy loss. A further reduction of the momentum spread by 10% also improves the simulated bunch position drift with respect to measurements. It implies that a better knowledge of the initial bunch distribution is necessary to draw conclusions on potential impedance missing in the model.

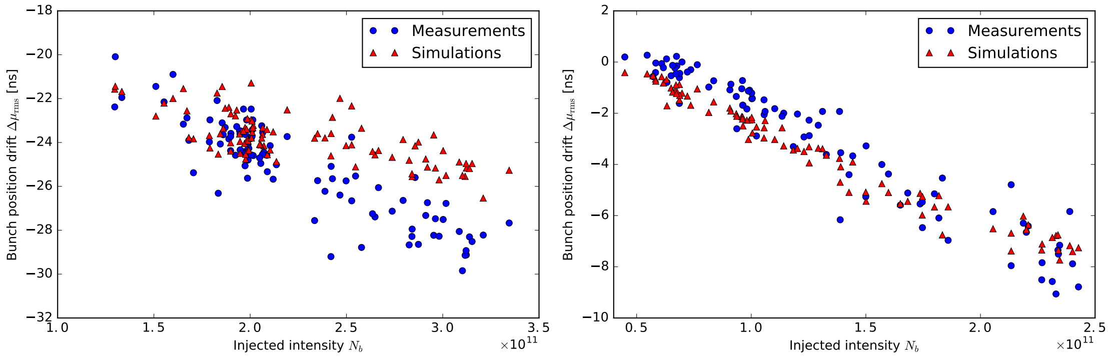

(a) Q20 optics (b) Q26 optics

Figure 4.15 – The simulated bunch position drift $\Delta\mu_{\mathrm{rms}}$ (red) using an initial bunch profile with non-filtered noise above 2 GHz and a reduced momentum spread $\Delta p_m/p$ with respect to the simulations shown in Fig. 4.12, compared to the measured one (blue) in the Q20 (left) and Q26 (right) optics.

4.5 Conclusions

The measurements of the bunch profile modulation by high frequency impedance sources with the RF voltage switched off allowed the identification of the main contributions driving microwave instabilities in the SPS. Measurements were performed in two optics available in the SPS, and a large bunch profile modulation was measured at 1.4 GHz. The QF-type vacuum flanges were then identified to be the source of this instability. They are also expected to be the main source of microwave instabilities in the SPS with RF on [74]. Peaks in the spectrum at other frequencies were also studied, and allowed the identification of the QD-type vacuum flanges to be the source of a bunch modulation at 2.45 GHz. Measurements were compared with macroparticle simulations to evaluate the accuracy of the present impedance model, and the reasonable agreement between measurements and simulations led to the conclusion that the main contributions of the vacuum flanges impedance are well represented. This method is very sensitive to the initial bunch distribution and a better agreement between measurements and simulations can be achieved with reduced momentum spread and depending on the initial high frequency noise in the bunch spectrum. The most important contributions to microwave instability have been identified and an impedance reduction of the impedance sources is foreseen in the frame of the LIU project.

5 Single bunch instabilities during the SPS ramp

5.1 Introduction

Studies of the longitudinal instabilities during the SPS cycle were used to test the present SPS impedance model. Measurements were done for both proton and ions bunches. The instability thresholds were found by scanning the bunch intensity. Measurement results are compared with macroparticle simulations done with the BLonD code using the present SPS impedance model. The comparison of measured and simulated instability thresholds allowed the benchmarking of the SPS impedance model as a whole.

The instability measurements for proton bunches are presented for various RF configurations: two different RF voltage programs during the cycle, in single and double RF operation. In the stable regime, the bunch is lengthened due to the potential-well distortion, as described in the Introduction. The bunch lengthening was compared with the analytical formula to evaluate the reactive impedance of the SPS. A good knowledge of the real machine parameters during measurements is also important. The influence of the parameters of the fourth harmonic RF system used in double RF operation on the instability thresholds will be shown.

The instability of ion bunches is presented in the second part. In this study, the ion species was the lead $^{208}\mathrm{Pb}^{82+}$. Due to the ion mass, the ion cycle in the SPS is different from the proton one, and the transition energy is crossed. The study presented here is focused on the effects on the flat top energy, where the instability threshold is compared with the threshold for loss of Landau damping. The result allows to have another evaluation of the reactive impedance of the SPS.

5.2 Proton bunches

In this section, the SPS impedance model is tested by comparing the instability thresholds for proton bunches found in measurements and macroparticle simulations. A single proton bunch was accelerated from a momentum of 26 GeV/c to 450 GeV/c, using two different

RF programs. The first RF program is the Constant Bucket Area (CBA), and in this case the bucket area was $\mathcal{A}_b = 0.5$ eVs along the ramp. The minimum RF voltage of the 200 MHz RF system at the end of the ramp was kept to 2 MV. The second RF program used is the High Voltage (HV), which starts like the CBA program but stays at a high voltage of $V_{200\text{ MHz}} = 7$ MV from the middle of the cycle till the end of the ramp. In both cases, the RF voltage at the injection was put at $V_{200\text{ MHz}} = 1.5$ MV. The two RF programs are shown together with the energy ramp in Fig. 5.1. The bunch is generated in the PSB where the bunch intensity N_b was varied while keeping a constant longitudinal emittance $\varepsilon_{2\sigma} \approx 0.25$ eVs [71]. The bunch profiles were measured at regular time intervals using a Wall-Current Monitor, and the bunch intensity was measured using a DC Beam Current Transformer. Examples of acquisitions (bunch length and intensity) are shown in Fig. 5.2.

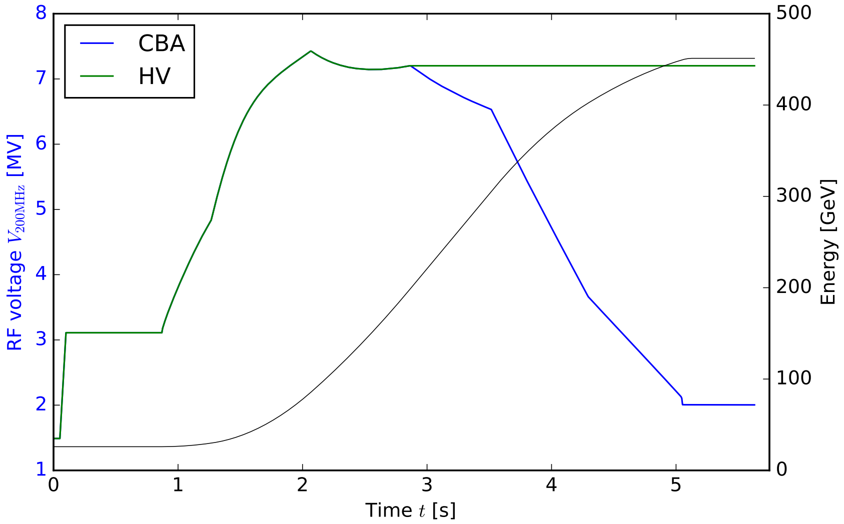

Figure 5.1 – Energy (black) and RF voltage programs used in the SPS for the protons instability study. The RF programs are shown in colour: Constant Bucket Area (CBA, blue) and High Voltage (HV, green).

5.2.1 Beam instabilities in single RF operation

For the measurements and simulations presented in this section, only the 200 MHz RF system was used (single RF operation). Examples of acquisitions for unstable cases in the CBA and HV RF programs are shown in Fig. 5.2. For each profile acquisition, the bunch length was calculated from the Full-Width-Half-Maximum value of the bunch profile, rescaled to $\tau_L = \left(2/\sqrt{2\ln 2}\right)\tau_{\text{FWHM}}$ and corresponding to the bunch length $4\sigma_{\text{rms}}$ for a Gaussian bunch length. This is the same as used in operation for the Beam Quality Monitor (BQM), which in operation determines the acceptable beams to be injected in the LHC [80]). Examples of bunch length measurements in single RF operation are shown in Fig. 5.2 together with the corresponding intensity measurements.

To determine whether the bunch is unstable and what is the starting time of the instability,

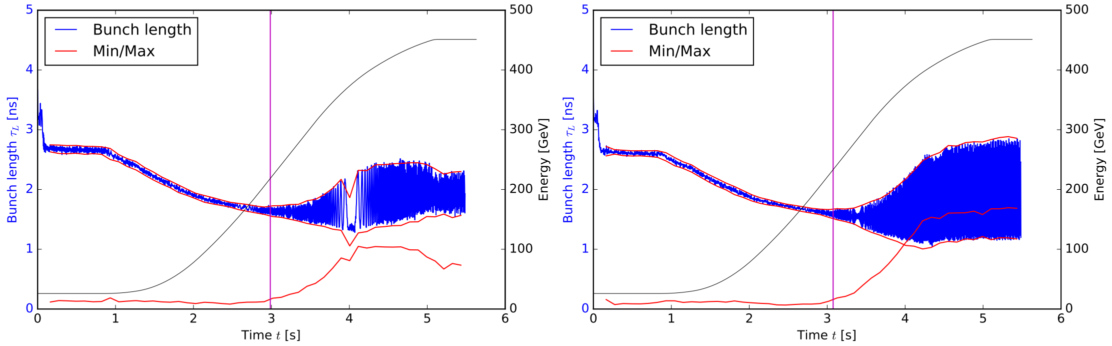

(a) CBA - Bunch length τ_L (b) HV - Bunch length τ_L

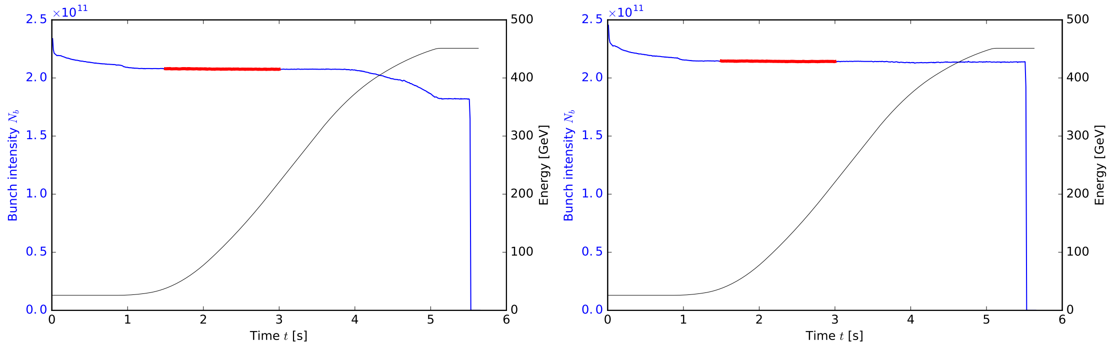

(c) CBA - Bunch intensity N_b (d) HV - Bunch intensity N_b

Figure 5.2 – Longitudinal instability observed during the acceleration ramp in single RF operation in the CBA (left) and the HV (right) RF voltage programs, for bunches with an intensity $N_b \approx (2.1-2.2)\times 10^{11}$ ppb. The top plots show the bunch length (blue) and the amplitude of oscillations (red) during the cycle used for the instability threshold criterion. The time of the start of the instability is represented with the magenta vertical line. The corresponding measured intensity is shown in the bottom plots, where the red line corresponds to the bunch intensity used for macroparticle simulations.

the amplitude of the bunch length oscillations $\Delta\tau_L$ was used (in red in Figs. 5.2a and 5.2b). The criterion to consider the bunch unstable was set to $\Delta\tau_L/\tau_L > 0.1$. The starting time of the instability is associated with the beam energy at the corresponding time during the cycle. The bunch intensity was scanned, and each acquisition like those presented in Fig. 5.2 corresponds to a point in the Fig. 5.3. The large spread in the results comes from the fact that the instability is slowly rising. Therefore this makes it difficult in data analysis to precisely identify the starting time of the instability.

The intensity threshold of the instability is shown in Fig. 5.3 as a vertical coloured column, corresponding to the intensity range where the stability is uncertain. The range for the intensity threshold is obtained by taking the minimum intensity for which a bunch was unstable, together with the maximum intensity for which a bunch was stable.

Simulations were done with the code BLonD using the present SPS impedance model to test the ability of the model to reproduce the parameters of the measured instabilities. The longitudinal space charge impedance was also included, using the calculations presented in Chapter 3. To cover the same range in bunch intensities and initial bunch profiles, each measurement was reproduced in simulations. An average bunch intensity was taken at the time scale of $(1-3)$ s (see Fig. 5.2). In order to get the actual bunch intensity, which should not contain the un-captured particles (due to the S-shape of the injected particle distribution [73]), and be affected by the losses at the end of the ramp due to the instability (see Fig. 5.2c). The initial particle distribution was reconstructed from the measured line density using the Abel transform (using Eq. (1.53)). This allowed the generation of a matched distribution in simulations taking into account the potential well distortion (assuming that the present SPS impedance model is close to reality). Simulations results are presented in Fig. 5.3, using the same analysis method as in measurements.

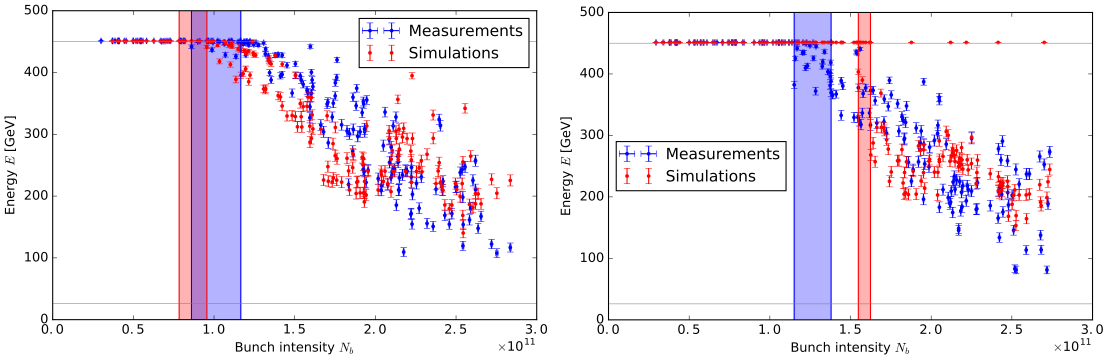

(a) CBA

(b) HV

Figure 5.3 – Energy E during the acceleration ramp at which the instability starts as a function of the bunch intensity for the CBA (left) and the HV (right) RF programs in single RF operation. Measurements are represented in blue and simulations in red. Each point corresponds to one measurement/simulation as shown in Fig. 5.2. The vertical coloured areas correspond to the instability threshold, where the limits are defined by the lowest unstable and the highest stable intensities. The grey horizontal lines correspond to the flat bottom and flat top energies.

For the CBA RF voltage program, measurements and simulations are in good agreement, both for the intensity (within 10%) and the energy thresholds. For the HV RF program, two regions in bunch intensities can be distinguished. The first one is above the intensity threshold $N_b > 1.6 \times 10^{11}$ ppb, where measurements and simulations are in good agreement. For the second region with $N_b < 1.6 \times 10^{11}$ ppb, bunches in measurements are more unstable than in simulations. To understand the source of the discrepancy, an example of measurements and the corresponding simulation for $N_b \approx 1.2 \times 10^{11}$ ppb is shown in Fig. 5.4. At this intensity, the growth rate of the instability in measurements is extremely small. The difference between measurements and simulations for slow instabilities can be explained in two ways. The first explanation is that some impedance is missing from the present SPS impedance model, as it was discussed in Chapters 2 and 4. A second explanation is that some perturbation of bunch motion is not damped on the long flat bottom, and can initiate an instability during the ramp at lower beam energy. In Chapter 4 the impact of the initial perturbations was discussed and it was shown that initial conditions play an important role. The bunch generated in simulations is matched to the RF bucket, and it may be necessary to add an initial perturbation to account for the small mismatch at flat bottom in the machine. In the Section 5.2.2, the bunch lengthening is used as another criterion for the intensity threshold of the instability.

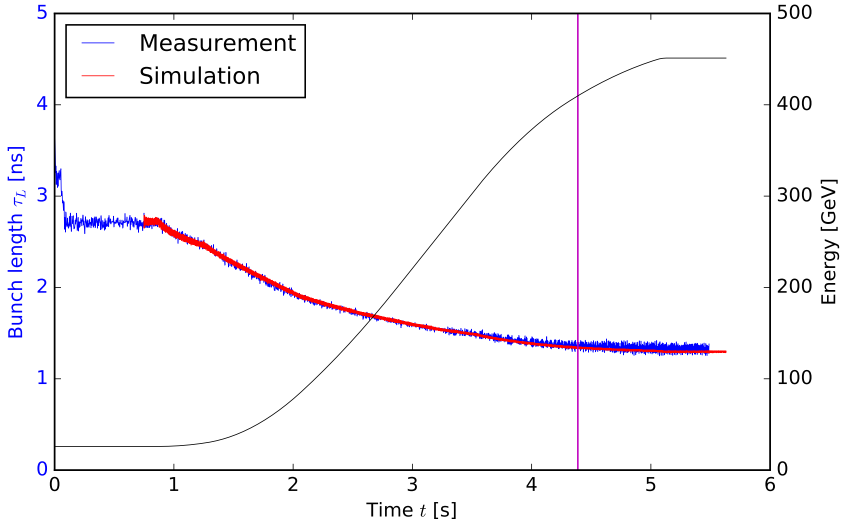

Figure 5.4 – Example of bunch length measurements (blue) and the corresponding simulation (red) along the cycle for the bunch intensity $N_b \approx 1.2 \times 10^{11}$ ppb. The measured bunch is considered unstable according to the $\Delta\tau_L/\tau_L > 0.1$ criterion, while the simulated bunch is stable.

For the the HV program another surprising result is the presence of stable points at high intensities $N_b > 1.9 \times 10^{11}$ ppb (which were not used to determine the instability threshold). The origin of these stable cases was investigated by running new macroparticle simulations, scanning both the bunch intensity and the initial bunch length, using the following particle distribution in phase space:

$$\psi(\mathcal{H}) = \psi_0 \left(1 - \frac{\mathcal{H}}{\mathcal{H}_0}\right)^{\frac{3}{2}}, \tag{5.1}$$

where ψ_0 is the normalisation factor of the distribution, $\mathcal{H}_0$ is the value of the Hamiltonian at the edge of the distribution, which is used as an input parameter related to the full bunch emittance. Note that this method is different from the one used previously and based on the Abel transform, where the measured bunch profiles were imposed. In the present case, the exponent $3/2$ in Eq. (5.1) was chosen to get bunch profile shapes comparable to the ones in measurements, but allowing a scan of the bunch length using the parameter $\mathcal{H}_0$. The initial bunch length at flat bottom τ_L in simulations was varied in the range $\approx (2.1-3.0)$ ns and the bunch intensity in the range $(0.6-3.0) \times 10^{11}$ ppb. Simulation results are shown together with measurements in Fig. 5.5.

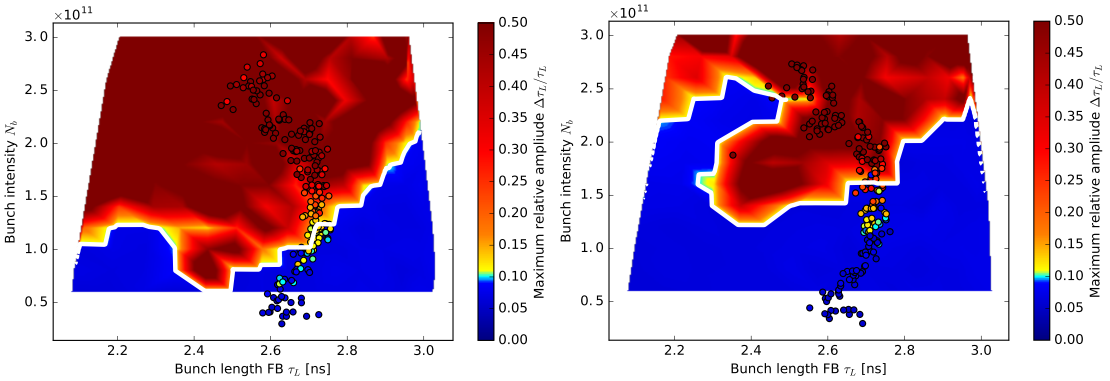

(a) CBA

(b) HV

Figure 5.5 – Stability maps obtained in simulations using the particle distribution (5.1) as an input for CBA (left) and HV (right) RF voltage programs. The measurements (dots) are shown on top of the simulations. The colour-scale corresponds to the maximum relative amplitude of oscillations $\Delta\tau_L/\tau_L$ during the cycle. The blue colour corresponds to stable regions and red unstable regions. The instability threshold in simulation is represented by the white contour.

Simulations done using the particle distribution (5.1) are also in reasonable agreement with measurements, with the same comments about results for the HV program close to the instability threshold. An interesting result is the non-linearity of the intensity threshold of the instability as a function of the injected bunch length. We can notice the presence of "islands" of stability, which consist of stable areas for smaller bunch lengths (emittance). For simulations using the CBA RF program a stability island is present around $\tau_L \approx 2.3$ ns and $N_b \approx 1.0 \times 10^{11}$ ppb, while for the HV RF program an island can be seen around $\tau_L \approx 2.4$ ns and $N_b \approx 2.3 \times 10^{11}$ ppb. The stable points in simulations in Fig. 5.3b correspond to cases where the initial particle distribution was generated with a slightly smaller bunch length with respect to measurements, had the initial bunch parameters located in the stability island and remained stable along the cycle. Islands of stability were also observed in simulations at flat top, and were partially explained by the increase of the synchrotron frequency spread, providing more Landau damping [81]. This is also related to the non-trivial synchrotron frequency shift behaviour analysed in Chapter 2.

The intensity threshold of instabilities has a non-monotonic dependence on intensity and bunch length. Nevertheless, the reasonable agreement between measurements and simulations for the RF configurations presented in this section shows that the present SPS impedance model includes the most important contributions.

5.2.2 Bunch lengthening from potential-well distortion

Another interesting result of the measurements presented in the previous section is the bunch lengthening with intensity for the stable cases (due to potential-well distortion). Measurements of the bunch lengthening at flat top for the HV RF program are shown in Fig. 5.6. As introduced in Chapter 1, the bunch lengthening assuming a constant longitudinal emittance is described by [65]:

$$\left(\frac{\tau_L}{\tau_{L0}}\right)^2 = \frac{\omega_{s0}}{\omega_s}\left[\frac{\cos\phi_s}{\cos\left(\phi_s+\Delta\phi_s\right)}\right]^{\frac{1}{2}}. \tag{5.2}$$

This equation together with the synchrotron frequency shift for a binomial bunch profile (2.16), and assuming that the synchronous phase shift $\Delta\phi_s$ is small, leads to:

$$\left(\frac{\tau_L}{\tau_{L0}}\right)^4 + \frac{16 N_b q \Gamma\left(3/2+\mu\right)\mathrm{Im}\mathcal{Z}/n}{\omega_{\mathrm{rev}}^2 V_{\mathrm{RF}} h \sqrt{\pi}\Gamma\left(\mu\right)\cos\phi_s \tau_{L0}^3}\left(\frac{\tau_L}{\tau_{L0}}\right) - 1 = 0. \tag{5.3}$$

For a parabolic bunch profile ($\mu = 1$), this equation gives the Eq. (1.67) presented in the Introduction.

The bunch length as a function of the bunch intensity at flat top in the HV RF program was fitted (below the intensity threshold) using Eq. (5.3), giving an evaluation of the reactive SPS impedance $\mathrm{Im}\mathcal{Z}/n$. Both in measurements and simulations the obtained value of the reactive impedance is $\mathrm{Im}\mathcal{Z}/n \approx 10\ \Omega$, which is much higher than the values obtained in Chapter 2. For instance, the equivalent impedance in Fig. 2.6c for bunch lengths of $\tau_L \approx (1.2-1.4)$ ns is in the order of $(\mathrm{Im}\mathcal{Z}/n)_{\mathrm{eq}} \approx (0.5-1.5)\ \Omega$. Note that the bunch lengthening in measurements and simulations are in good agreement in Fig. 5.6. A possible explanation is that either the longitudinal injected emittance was not constant in measurements, or that the bunch lengthening is not only determined by the potential-well distortion (e.g. uncontrolled emittance blow-up due to weak instabilities during the ramp).

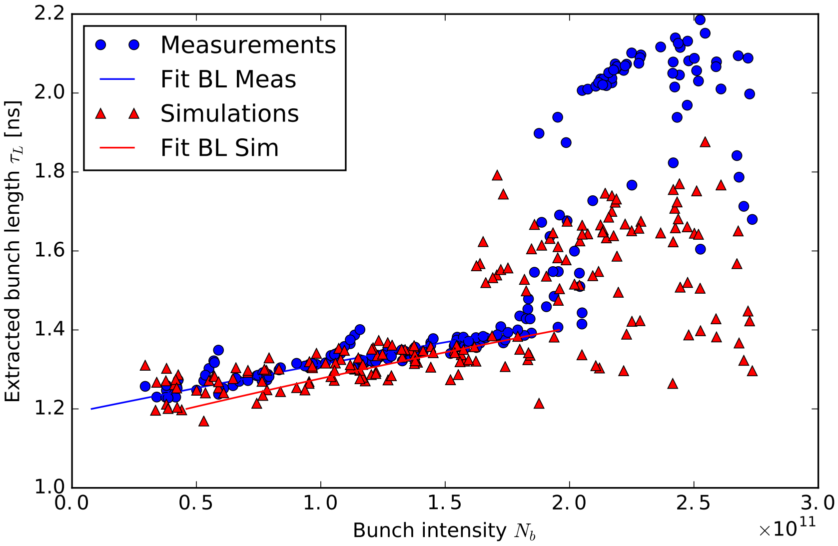

Figure 5.6 – Bunch length as a function ot the bunch intensity at flat top using the HV RF program in measurements (blue) and simulations (red). The bunch lengthening below the instability threshold was fitted using Eq. (5.2).

Several limitations make the measurements of the bunch lengthening due to potential-well distortion difficult in the SPS. There is no damping mechanism of the longitudinal emittance like in lepton accelerators with synchrotron radiation. Therefore, blow-up of the longitudinal emittance in the PSB up to the flat top energy in the SPS can occur, and affect the results presented above. We can give several examples of emittance blow-up: the longitudinal emittance shaving used in the PSB to adjust the bunch intensity and emittance which is affected by potential well distortion (large space charge impedance), the injection from one machine to another which can introduce some emittance blow-up due to the mismatch of the particle distributions to the capture RF bucket, etc. Finally, since our knowledge of the longitudinal emittance is based on the measurement of bunch profiles, it is difficult to ensure that the longitudinal emittance was kept constant for these measurements. Nevertheless, the measured bunch lengthening (including the variable injected longitudinal emittance) was well reproduced in simulations. This is due to the fact that the bunch profile was used to generate the initial particle distribution (applying the Abel transform), which allows accounting for the possible change in longitudinal emittance from one measurement to another.

Another remark is the identification of the intensity threshold from the bunch lengthening. For the HV RF program, all the unstable cases with bunch intensities $N_b < 1.8 \times 10^{11}$ ppb have a small growth rate, and the instability does not generate longitudinal emittance blow-up. Well above the intensity threshold, the growth rate of the instability is high leading to a large emittance blow-up, which is well reproduced in simulations. This is also the case for the results obtained in the CBA RF program which are not presented here.

5.2.3 Beam instabilities in double RF operation

Measurements of instability during the SPS ramp were also performed in double RF operation using the 800 MHz RF system in addition to the 200 MHz one. In this configuration, the total voltage seen by the particle is:

$$V_{\text{tot}}\left(\phi\right) = V_{200}\sin\phi + V_{800}\sin\left(4\phi + \phi_{800} + \phi_{\text{off}}\right), \tag{5.4}$$

where the RF voltage amplitude of the 800 MHz RF system is set to $V_{800} = 0.1V_{200}$ and the RF phase was adjusted to be in Bunch Shortening Mode (BSM) along the acceleration ramp with $\phi_{800} = \pi - 4\phi_s$, where ϕ_s is the synchronous phase taken from the single RF configurations. We introduce a phase offset ϕ_{off} which will be useful below.

Examples of measurements in double RF operation, for bunch intensities $N_b \approx (2.1-2.2) \times 10^{11}$ ppb are shown in Fig. 5.7. The difference from the single RF operation is that the instability is much faster and more violent. The use of a double RF system in BSM increases the synchrotron frequency spread and hence the Landau damping [13, 14]. The fast rate of the instability is a signature of microwave instability. According to the results presented in Chapter 4, the main impedance source responsible for this instability is the vacuum flanges (the QF-type).

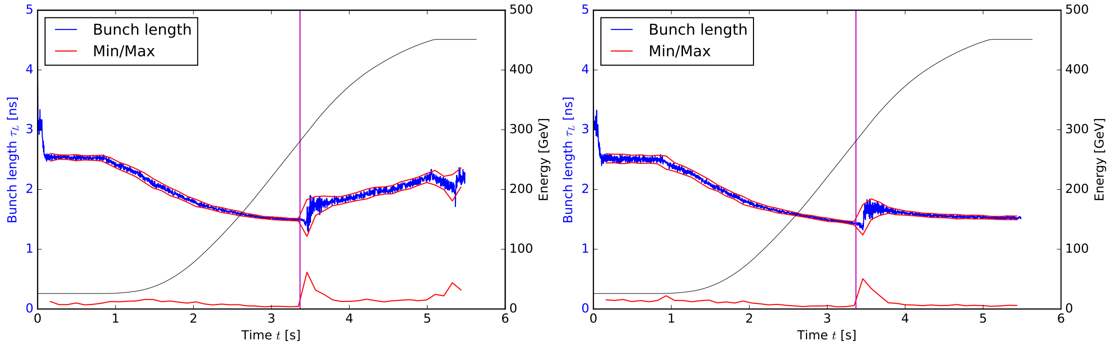

(a) CBA (b) HV

Figure 5.7 – Single bunch longitudinal instability. Bunch length measured during the acceleration ramp in double RF operation, in the CBA (left) and the HV (right) RF voltage programs for bunches with an intensity during the ramp of $N_b \approx (2.1 - 2.2) \times 10^{11}$ ppb.

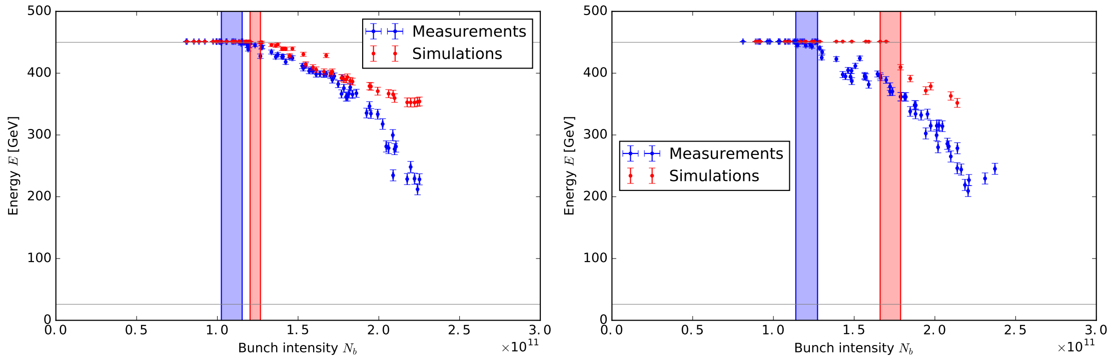

(a) CBA (b) HV

Figure 5.8 – Energy E during the ramp at which the instability starts, as a function of the bunch intensity N_b, for the CBA RF program (left) and the HV RF program (right) in double RF operation. Measurements are in blue and simulations in red. Each point corresponds to one measurement/simulation as shown in Fig. 5.7. The vertical coloured areas correspond to the instability threshold, where the limits are defined by the lowest unstable and the highest stable intensities. The grey horizontal lines are at the flat bottom and flat top energies.

Measurements were reproduced in simulations using the Abel transform for the generation of the input particle distribution, similar to the approach described in the previous section. Results are shown together with measurements in Fig. 5.8. First simulation results were not able to reproduce the measured instability threshold, especially for the HV RF program (50% deviation in the intensity threshold in simulations with respect to measurements). Therefore, investigations were started to understand this discrepancy. A probable cause could be related to the effective RF parameters of the 800 MHz RF system which were not accurately known during measurements. An indication is the inability to generate a particle distribution using the Abel transform in simulations. Indeed, if the potential well used in simulations is too different from the actual one in measurements, the Abel transform is not able to find a self-consistent solution providing in simulations a bunch profile similar to the measured one. Moreover, it is difficult in practice to know exactly the phase of the 800 MHz RF system, relatively to the main harmonic at 200 MHz since the calibration is based on beam measurements.

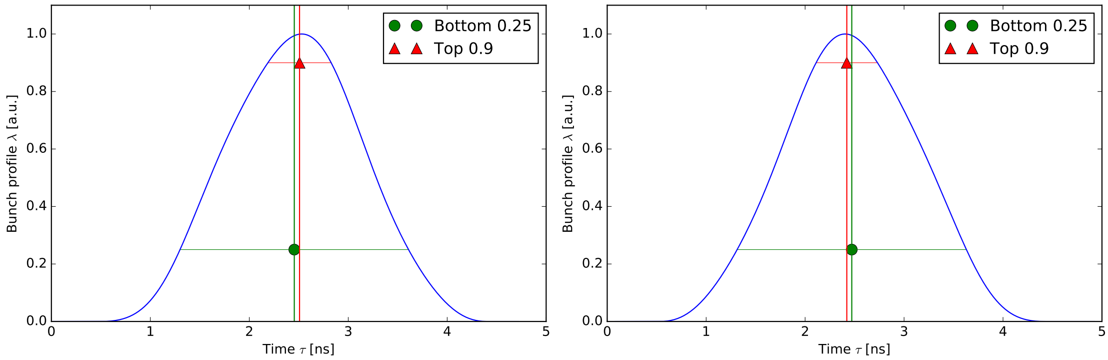

(a) $\phi_{\text{off}} = -70°$

(b) $\phi_{\text{off}} = +70°$

Figure 5.9 – Simulated tilt $\delta\tau$ of the bunch profile in double RF operation for a phase offset of $\phi_{\text{off}} = -70°$ (left) and $\phi_{\text{off}} = +70°$ (right) from BSM. The tilt was computed assuming $V_{800} = 0.1\,V_{200}$.

To determine the effective parameters of the 800 MHz RF system during the instability measurements, the bunch profile tilt was measured as a function of the phase offset of the 800 MHz RF system ϕ_{off} [14]. The tilt is determined by the shape of the potential well due to the voltage amplitude and phase ϕ_{off} of the 800 MHz RF system. Single bunches with a fixed longitudinal emittance and low bunch intensity ($N_b \approx 5 \times 10^{10}$ ppb) were used to measure the tilt at flat bottom energy and at flat top (to evaluate the possible change of ϕ_{off} with energy). The bunch profile tilt was obtained by comparing the centre of the top part of the profile (at 90%, τ_{top}) with the bottom part (at 25%, τ_{bottom}) and is defined as $\delta\tau = \tau_{\text{bottom}} - \tau_{\text{top}}$. Examples of simulations are shown in Fig. 5.9.

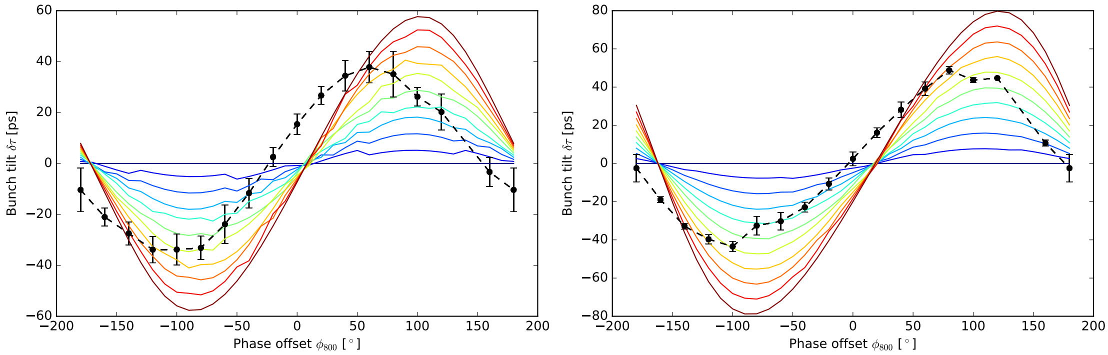

(a) Flat bottom energy

(b) Flat top energy

Figure 5.10 – Bunch profile tilt $\delta\tau$ as a function of the 800 MHz phase offset ϕ_{off}. Measurements (black) are compared with simulations (colour) where the voltage ratio V_{800}/V_{200} was scanned from 0 to 0.1 with steps of 0.01 (from blue to red), at flat bottom (left) and flat top (right).

Measurements of the bunch profile tilt as a function of the phase offset ϕ_{off} were compared with simulations. A bunch was generated in simulations matched to the RF bucket using the particle distribution in Eq. (5.1), with a value of $\mathcal{H}_0$ which was set to match the measured bunch lengths. The ϕ_{off} was scanned, but also the voltage ratio V_{800}/V_{200} to evaluate the effective RF voltage of the 800 MHz RF system. Measurements and simulations are shown together in Fig. 5.10. The phase error ϕ_{off} is determined by comparing the phase at which the tilt $\Delta\tau = 0$. The phase error was $\phi_{\text{off}} \approx 30°$ at flat bottom and $\phi_{\text{off}} \approx 20°$ at flat top. Moreover, the 800 MHz voltage in measurements seems to be lower than what was assumed. Simulations show that the voltage ratio V_{800}/V_{200} was 0.06 instead of 0.1, both for flat bottom and flat top.

The simulations performed with the corrected RF values gave the results shown in Fig. 5.11. For the CBA RF program, the results did not change significantly. However, for the HV RF program the agreement between measurements and simulations is now excellent, both for the intensity threshold and the dependence of the instability on energy. Therefore, it is likely that the effective RF parameters of the 800 MHz RF system were indeed different from those expected during the measurements. The remaining discrepancy may be related to a missing impedance source. The potential missing impedance at 1.8 GHz discussed in Chapter 4 may be a good candidate in the present RF configuration. Note that small changes in the parameters of the 800 MHz RF system can significantly change the instability threshold. Since the present SPS impedance model is able to reproduce the measurements in most of the RF configurations, macroparticle simulations could be used for optimisation of the operational cycles for a single bunch with very high intensity (e.g. AWAKE).

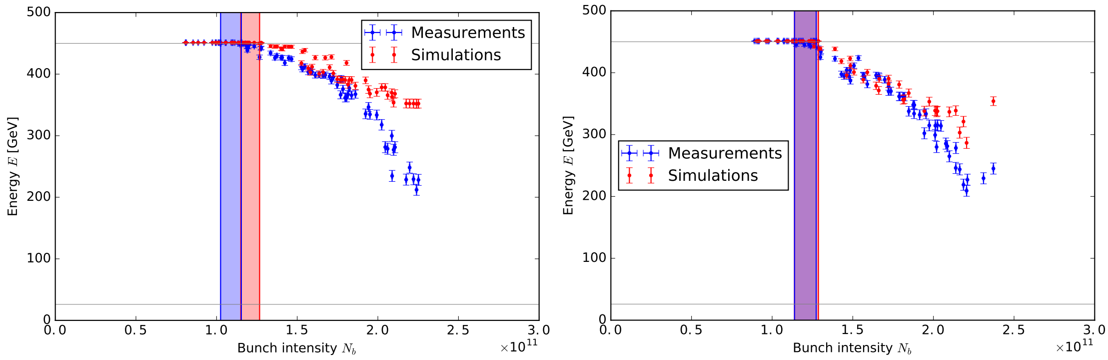

(a) CBA

(b) HV

Figure 5.11 – Energy E during the ramp at which the instability starts, as a function of the bunch intensity N_b, for the CBA RF program (left) and the HV RF program (right) in double RF operation and with the corrected RF parameters of the 800 MHz using results from Fig. 5.10.

5.3 Ion bunches

In this section, measurements and simulations of LHC-type ion beam instabilities are presented. The ion species is $^{208}\text{Pb}^{82+}$. The charge of the ion is noted Z below (Z=82), and the bunch intensity is now defined as the number of charges in the bunch N_q. The ion beam used in the measurements presented below was composed of 24 bunches, obtained from the consecutive injections of 12 batches of 2 bunches. Injections were done on a long flat bottom (40 s) as shown in Fig 5.12a. Batches are separated by 175 ns while the two bunches in one injection are separated by 100 ns (see Fig. 5.12b). For the analysis, the measured data was grouped depending on the bunch number along the batch with an index going from 1 to 24. After the long flat bottom, the beam is then accelerated from a proton equivalent momentum of 17 Z GeV/c to 450 Z GeV/c. The beam parameters presently achieved in the SPS are summarised in Table. 5.1. A particularity of the ion beam in the SPS is that the transition energy is crossed during the acceleration ramp (see Table I.2), at $t \approx 41$ s in the present cycle. Note that only the 200 MHz RF system is presently used for the ion cycles, thus all results presented below were done in single RF operation. The RF program during the cycle is shown in Fig. 5.13.

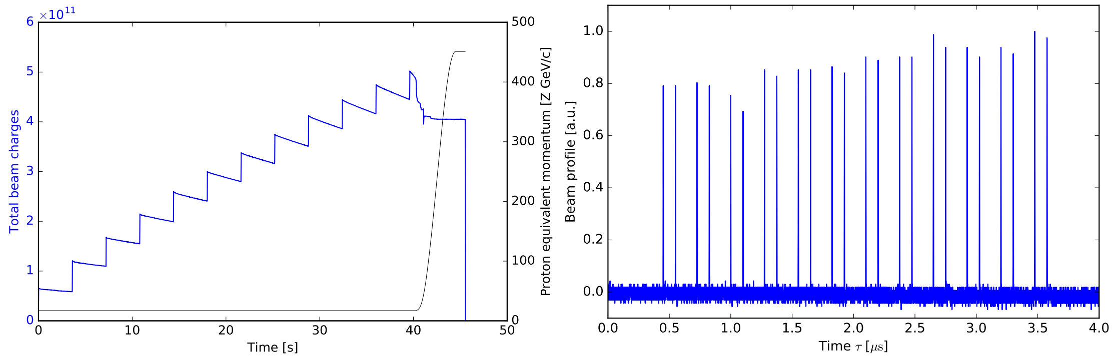

(a) Intensity during the ramp

(b) Bunch distribution

Figure 5.12 – The ion beam used for instability studies. The total beam intensity during the cycle (a), and a measured bunch distribution along the batch right before the acceleration ramp (b).

Table 5.1 – Achieved beam parameters in the SPS of the LHC ion type beam and goals of the LIU-IONS project [5]. Values separated with / correspond to (injection/extraction)

Parameter		**Achieved**	**LIU-IONS target**
Number of batch×bunches		12×2	6×8
Bunch spacing	[ns]	100	50
Batch spacing	[ns]	150	100
Bunch intensity N_b	$\times 10^8$	4.3/2.2	2.6/1.7
Longitudinal emittance ε_L	[eVs/u]	Variable (losses)	<0.24
Extracted bunch length $\tau_L = 4\sigma_{\mathrm{rms}}$	[ns]	Variable (losses)	<1.7
Transverse emittance $\varepsilon_{x,y}$	[μm]	1.0/1.5	1.0/1.3

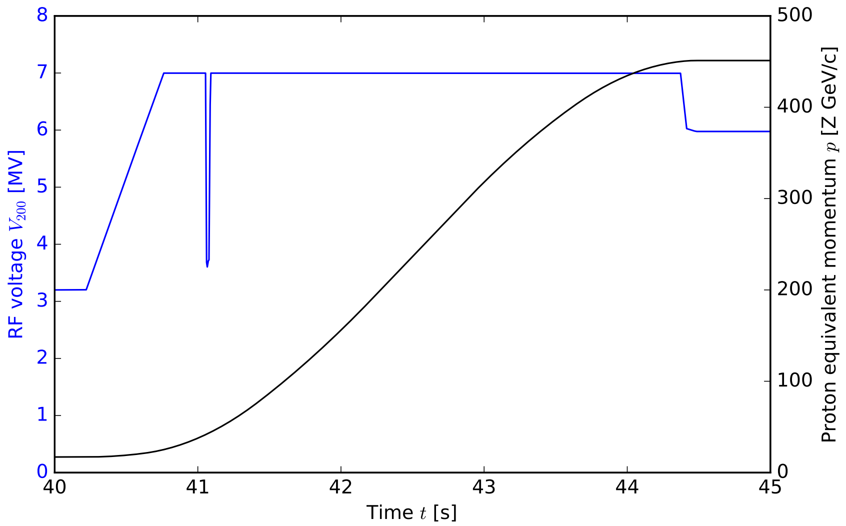

Figure 5.13 – The RF voltage program of the 200 MHz RF system (blue) during the energy ramp (black). The dip in RF voltage at $t \approx 41$ s corresponds to the transition crossing.

During the long flat bottom, the RF noise and intensity effects (space charge, Intra-Beam Scattering, Touschek effect) are responsible for continuous particle losses, reducing the bunch intensity and longitudinal emittance [82]. The first injected bunches lose more intensity than the last ones and their emittance is reduced more, as shown in Fig. 5.14. The large losses at flat bottom are responsible for a significant variation in the bunch lengths and intensities of $\approx \pm 20\%$. For this study of the ion beam stability, the losses were useful since the large range in intensity and emittance allows to find the instability threshold more easily. For the results presented below, it is assumed that due to the long distance between the bunches and their low intensity, no significant multi-bunch effects are present.

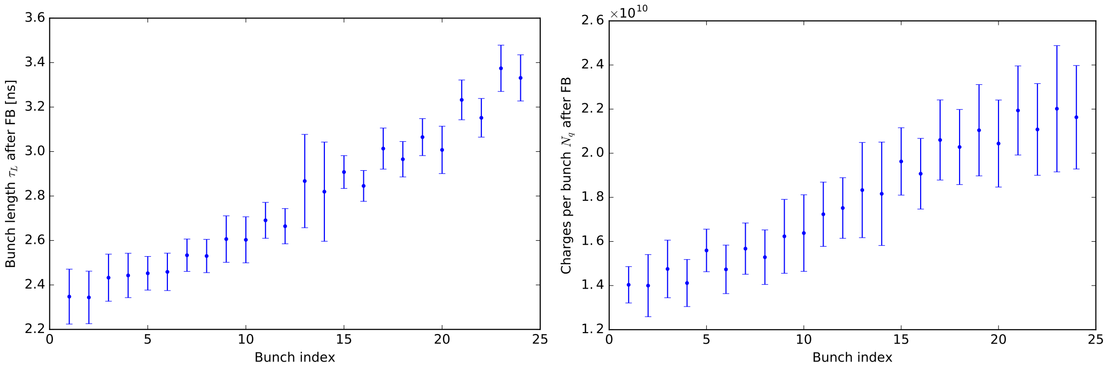

(a) Bunch length variation after FB

(b) Charges per bunch after FB

Figure 5.14 – Measured bunch lengths (left) and bunch intensities (right) depending on the bunch index in the batch. The error-bars correspond to the standard deviation $\pm 1\sigma$ in the measured data.

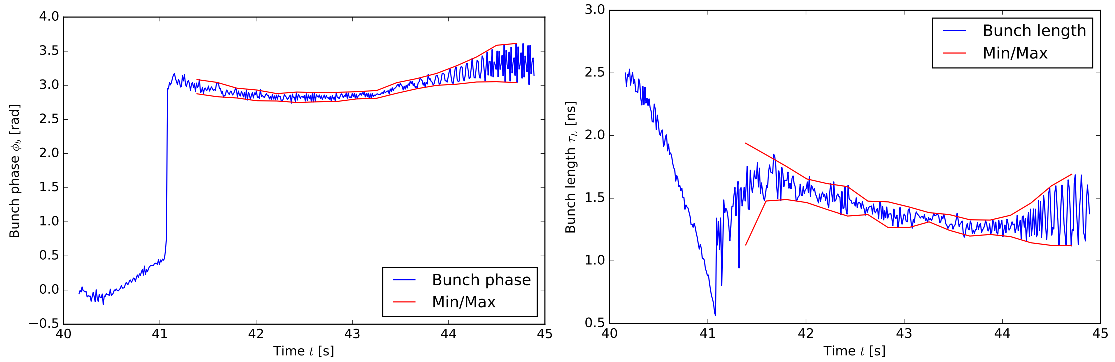

(a) Bunch phase

(b) Bunch length

Figure 5.15 – Example of instability measured for the 4th bunch in the batch. The bunch phase (left, unstable at $t \approx 43$ s) and the bunch length (right, unstable at $t \approx 44$ s) are shown as a function of time during the acceleration ramp. The red traces correspond to the maximum amplitude of the bunch phase/length.

An example of measured instability for the fourth bunch within the batch is presented in Fig. 5.15. At $t \approx 41$ ns, the effect of the transition crossing can be seen from the RF phase jump, and from the reduction of the bunch length. During transition crossing the adiabaticity condition presented in Eq. (1.54) is not fulfilled anymore since $\eta = 0$, and due to the change in sign of the slippage factor the effect of the impedance on potential well distortion is reversed. Bunch oscillations are initiated by this fast change in the potential well. In the present example, the oscillations caused by the mismatch due to transition crossing are well damped. However, an instability starts at $t \approx 43$ s manifesting as growing dipole oscillations (the amplitude of dipole oscillations below are expressed in degrees at the 200 MHz frequency). From $t \approx 44$ s, the dipole oscillations are complemented by bunch length oscillations leading to bunch filamentation.

Assuming that the motion of bunches in the beam is practically not coupled (absence of long range wakes), the (single) bunch stability was evaluated from the maximum dipole oscillations at flat top. Results are shown in Fig. 5.16a, and the criterion for the instability was set for an amplitude of dipole oscillations of 10°. Along the batch, the first bunches are the most unstable with the exception of the first two bunches. The last fact can be explained by the stabilisation by the RF phase loop. Indeed, the instability starts as dipole oscillations, and for these measurements the adjustment of the RF phase for the whole beam is based on the beam signal measured from the first two bunches, which are then better stabilised than the others.

At first, it may appear surprising that the following 10 bunches in the batch, which are also the bunches with lower intensity are unstable. To understand this fact, results are presented in Fig. 5.16b as a function of the bunch lengths and intensities at flat top energy. With this representation, it appears clearly that the most unstable bunches are not the ones with the highest intensities but the ones with the smallest bunch length, with a threshold at $\tau_L \approx 1.5$ ns.

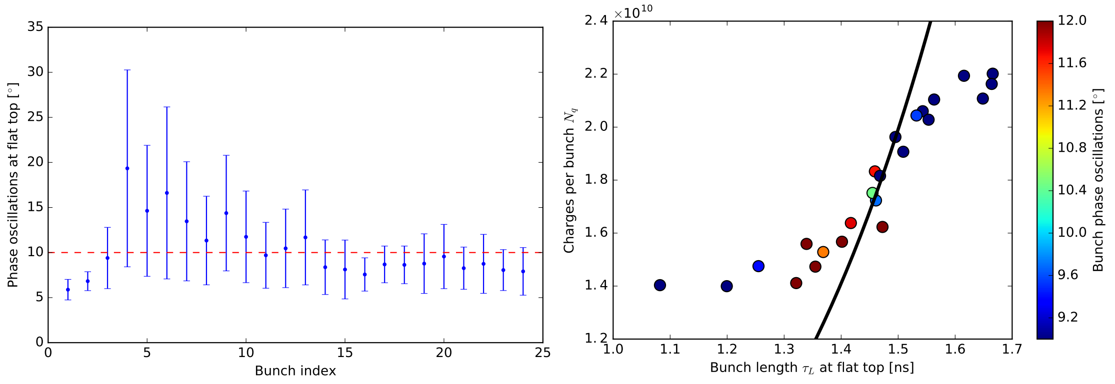

(a) Dipole oscillations for each bunch

(b) Intensity and bunch lenth threshold

Figure 5.16 – Beam stability depending on the bunch position in the batch. The amplitude of dipole oscillations as a function of the bunch index (a), with the criterion of instability (red dashed line). The dipole oscillations as a function of the bunch length and intensity at flat top (b), with the amplitude of dipole oscillations shown in colour (blue is stable and red is unstable), and with the expected threshold for loss of Landau damping (black line).

The significant dependence on the bunch length can be associated with the loss of Landau damping in single RF operation in presence of reactive impedance. The instability criterion can be expressed as [66]:

$$\frac{\mathrm{Im}\mathcal{Z}}{n} < \frac{F\left|\eta\right|E}{q^2\beta^2}\frac{\tau_L}{N_b}\left(\frac{\Delta E}{E}\right)^2\left(\frac{\Delta\omega_s}{\omega_s}\right), \tag{5.5}$$

where F is a form factor depending on the particle distribution. The scaling of the intensity threshold as a function of the bunch length (assuming that all the other parameters are constant) is obtained from Eq. (5.5) and can be expressed as:

$$N_{\mathrm{th}} \propto \frac{\tau_L^5}{\mathrm{Im}\mathcal{Z}/n}. \tag{5.6}$$

This scaling shows that the bunch length dependence is indeed expected to be very strong. This scaling is presented in Fig. 5.16b and agrees well with measurements. Note that the effective reactive impedance $\mathrm{Im}\mathcal{Z}/n$ was assumed constant in this example, although it was presented in Chapter 2 that the SPS effective reactive impedance also depends on bunch length. This approximation is reasonable since ion bunches have a Gaussian bunch profile ($\mu \to \infty$ in the binomial bunch profile (2.10)). In this case the bunch length dependence of the SPS effective reactive impedance is less strong, in comparison with the parabolic proton bunches, and the dependence on $N_{\mathrm{th}} \propto \tau_L^5$ is dominant.

To test the hypothesis that Landau damping is lost, macroparticle simulations were performed using the BLonD code for the ion bunches and for the machine parameters at flat top (V_{200} = 6 MV). The method used in simulations consisted of evaluating the damping

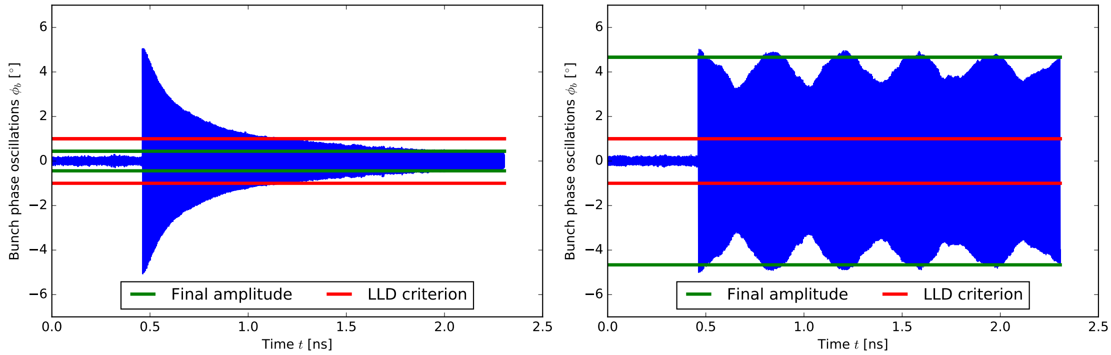

(a) Damped oscillations

(b) Un-damped oscillations

Figure 5.17 – Simulations of dipole oscillations caused by an initial phase kick of 5°. The bunch phase as a function of time for a stable (left) and an unstable (right) cases. The final amplitude of oscillations (green) should be below the criterion of loss of Landau damping (red) to be considered stable.

of dipole oscillations caused by an external excitation. The initial particle distribution was generated using a Gaussian bunch profile, matched to the RF bucket. A phase kick of 5° was applied, to excite a dipole motion without generating emittance blow-up from filamentation. The evolution of the bunch motion was simulated over 80’000 SPS turns, corresponding to a large number of synchrotron periods T_{s0}. The bunch was considered unstable if the dipole oscillations were not damped at the end of the simulation below an amplitude of 2°. Examples of stable and unstable simulated cases are shown in Fig. 5.17.

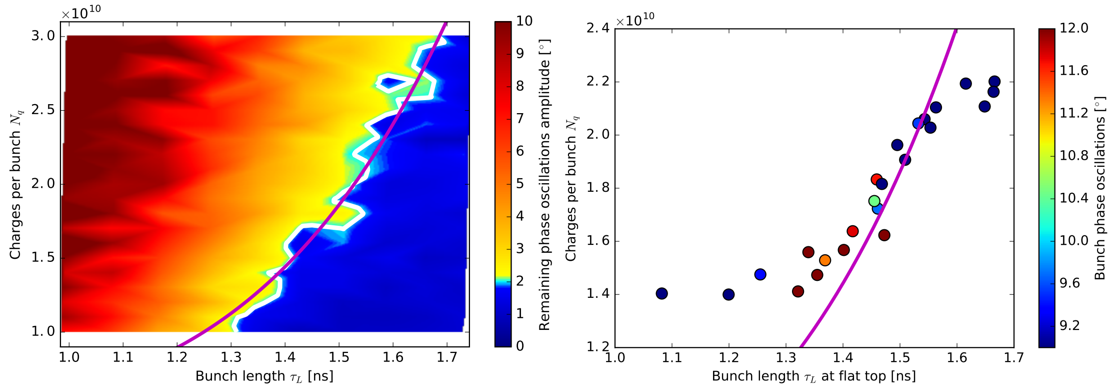

(a) Simulated stability map

(b) Simulated threshold with measurements

Figure 5.18 – Simulated stability map as a function of bunch length and intensity at flat top energy in single RF operation (left). The simulated loss of Landau damping threshold (magenta) is compared with measurements (right).

The initial bunch parameters (bunch length and intensity) were scanned, and results of simulations are shown in Fig. 5.18. The dependence of the instability threshold on bunch length and intensity matches well the expectations for loss of Landau damping. Moreover, the threshold obtained in simulations is in good agreement with measurements. This also supports the initial hypothesis that the measured instabilities for the ion bunches are caused by the loss of Landau damping. In addition, this implies that the reactive part of the present SPS impedance model is a reasonable representation of the reality.

An additional element of the study was to test in simulations the effect of the 4th harmonic RF system, which should increase the Landau damping. Simulations were done applying the same method as above, adding the contribution of the 800 MHz RF system with a voltage amplitude of $V_{800} = 0.1V_{200}$ in bunch shortening mode. Results are shown in Fig. 5.19. As expected, the operation with the 800 MHz significantly increases the threshold of loss of Landau damping. Although this RF system is not yet usable for the ion beam, it will be made operational during the Long Shutdown 2 (2019-2020) in the frame of the LLRF upgrade for the LIU-IONS project [5] and should help reducing the instability for the ion beams.

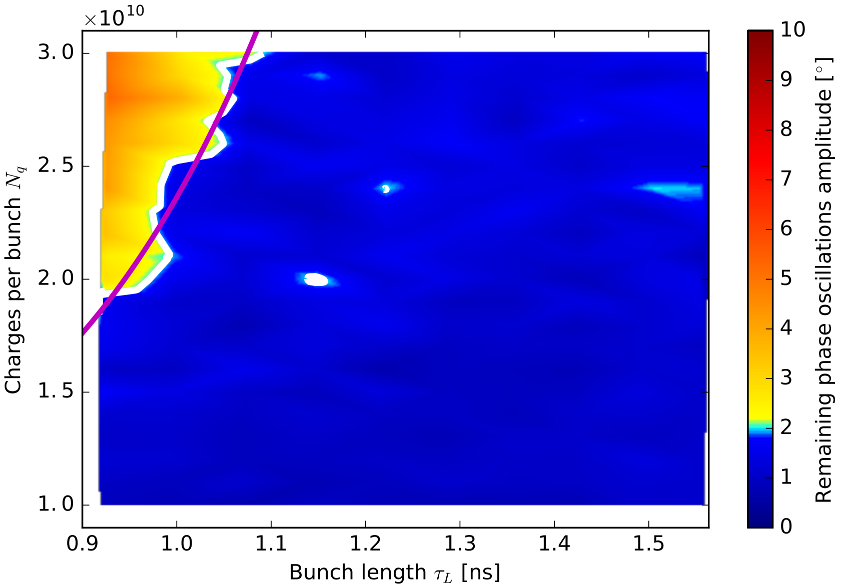

Figure 5.19 – Simulated intensity threshold of loss of Landau damping as a function of the bunch length in double RF operation with $V_{800} = 0.1V_{200}$ in bunch shortening mode at flat top energy.

5.4 Conclusions

The SPS instability thresholds have a non-monotonic dependence on the intensity and emittance. The present SPS impedance model used in BLonD simulations allows most of the observations for single bunch instabilities during the SPS ramp to be reproduced. In double RF, the agreement also depends on the knowledge of the voltage and phase of the fourth harmonic RF system. The small deviations between simulations and measurements remaining after correction of the RF parameters indicate that some impedance may still be missing in the SPS impedance model, which could correspond to the possible impedance sources discussed in Chapters 2 and 4.

The stability of ion bunches was also measured and the dependence of the instability on the bunch length and intensity was studied. A good agreement was found with the analytical threshold of loss of Landau damping in the presence of reactive impedance. Simulations at flat top using the present SPS impedance model were also able to reproduce the measured results. Therefore, this study is an additional argument to prove that the reactive impedance in the SPS impedance budget is well known. Like in the study with protons, the acceleration ramp could be simulated. However, the impact of the LLRF control (phase loop and radial loop) on the bunch oscillations initiated at transition crossing is important. An implementation of the SPS feedback loops would be necessary to accurately reproduce the measurements.

Thanks to the good agreement between measurements and simulations, the impedance source(s) responsible for instabilities can be investigated in more detail (see Chapter 6).

6 Applications for future projects

6.1 Introduction

In the previous chapters, the SPS impedance model was proven to be a reasonable representation of the reality from good agreement between measurements, simulations and theory. Therefore, the model was applied to make projections for projects relying on the SPS beam. In this chapter, initial results of simulations of the multi-bunch instability threshold for the LHC beam are presented.

The BLonD code was optimised to be able to perform simulations for the LHC beam in the SPS. The complexity resided in the high number of bunches (72), that significantly increases the number of operations. Presently, the simulation time-scale was reduced to the point where studies could be reasonably done, for simulations at flat top energy in the SPS with 72 bunches. Simulations were performed to evaluate the present instability threshold, and the future beam parameters that could be expected for the HL-LHC [3] project with the SPS upgrade which is part of the LIU project baseline [4]. This includes the upgrade of the RF systems [10] and the impedance reduction of the vacuum flanges which were presented in the previous chapters to be the main source of microwave instability in the SPS.

6.2 Simulation setup

In this section, simulations were performed to try to reproduce the measured instability threshold, find the most critical impedance sources for multi-bunch instabilities and evaluate the instability threshold after the SPS upgrade. Beam dynamics simulations were done using the BLonD code and the present SPS impedance model. For multi-bunch beams, the beam-loading effect in the 200 MHz RF system is compensated by the one turn delay feedback and feedforward systems, which are modelled in the following simulations by a reduction of the 200 MHz TWC impedance by -20 dB [83, 84]. In nominal operation, the LHC beam consists of 4 batches spaced by 225 ns. Each batch is composed of 72 bunches spaced by 25 ns. For this high number of bunches the simulation time is a limitation, and as the number of impedance sources is high an extensive number of simulations was needed to assess the effect of each of them. According to previous experimental studies the instability threshold doesn't depend on the number of batches [27], so the number of bunches in simulations was set to 72. All bunches were generated with the same emittance and intensity, and matched to the bucket including induced voltage. The chosen particle distribution gives a line density close to the measured one by using the distribution function in Eq. (5.1).

The RF voltage V_{200} is set to 7 MV (operational value at flat top, corresponding to the limit due to beam loading for the nominal intensity) and the voltage at 800 MHz $V_{800} = 0.1\, V_{200}$ in bunch shortening mode. As the instability threshold scales as $1/E$ and reaches a minimum at flat top, simulations were done only at flat top (450 GeV/c) for a real time of 2.3 s (corresponding to 100,000 turns in the machine), which is longer than in operation in order to see slowly rising instabilities.

In order to obtain the stability threshold a large range of emittances and intensities was scanned. For each simulation, the bunch length τ was computed for each bunch as a function of time, obtained from Full-Width-Half-Maximum (FWHM), rescaled to $\tau = 4\sigma$ assuming a Gaussian profile). To determine whether a configuration is unstable, the difference between minimum and maximum bunch length $\Delta\tau$ is compared to the average τ_{av}. The instability limit was set to $\Delta\tau/\tau_{\mathrm{av}} = 0.12$, which is efficient for the distinction between stable and unstable cases.

6.3 Present configuration

Simulations at flat top for the present beam and RF configuration, are compared with measurements in Fig. 6.1 for both single and double RF. Simulations are able to reproduce the instability threshold for 72 bunches for both cases. Results for 24 and 72 bunches are different, especially in double RF, showing that it is not possible to reduce the number of bunches in simulations to further simplify the computing. In single RF, the difference lies within the operational uncertainty (bunch to bunch variation in intensity). As the increase in the intensity threshold obtained from the 800 MHz RF system is large and crucial for the LHC operation, a good knowledge of the RF parameters is important (see Chapter 5) [74]. The reference point for the present configuration is $N_b = 1.35 \times 10^{11}$ ppb with $\tau_{\mathrm{av}} = 1.65$ ns.

The effect of the various impedance sources in double RF was tested first by completely removing them in simulations. Results are presented in Fig. 6.2. As the number of impedance sources is very large, efforts were focused on the ones that are the most critical in terms of beam stability and could be considered for impedance reduction: the vacuum flanges VF (shielding, redesign) and the HOM at 630 MHz (further damping). Completely removing either the HOM or all the VF gives a comparable gain in terms of instability threshold, about 15% for the nominal bunch length ($\tau = 1.65$ ns). For smaller bunch lengths, the gain from removing the vacuum flanges is bigger, their impedance contribution is mainly at high frequencies. As the gain is fairly small, it suggests that the VF and the HOM could have a comparable instability threshold. The next step was to test the combinations of removing the HOM and subsets of flanges (e.g.: between dipole and quadrupole magnets MQF, between BPMs and quadrupoles BPQX, unshielded pumping ports UPP). Removing the HOM and all the VF together gives large gain (40%), confirming that the HOM and VF are both limiting the beam stability. In case of impedance reduction of vacuum flanges, as many as possible should be shielded in all groups. All the remaining impedance sources were tested and their removal gives a small gain, except for the kickers. However, kickers impedance cannot be reduced easily.

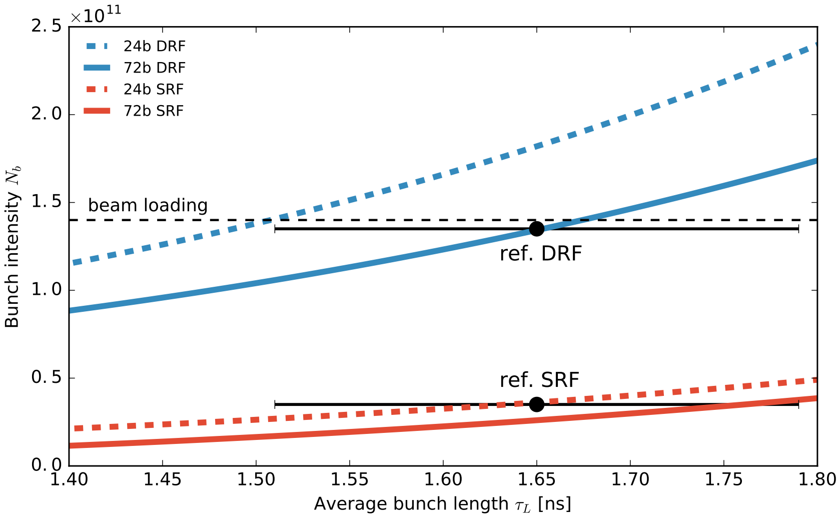

Figure 6.1 – Stability limits for the present operations found by simulations for single and double RF, 24 and 72 bunches at $V_{200} = 7$ MV and $V_{800} = 0.7$ MV, compared with measurements (error bars are the bunch-to-bunch variations, 72 bunches). The horizontal line corresponds to the present limit due to beam loading.

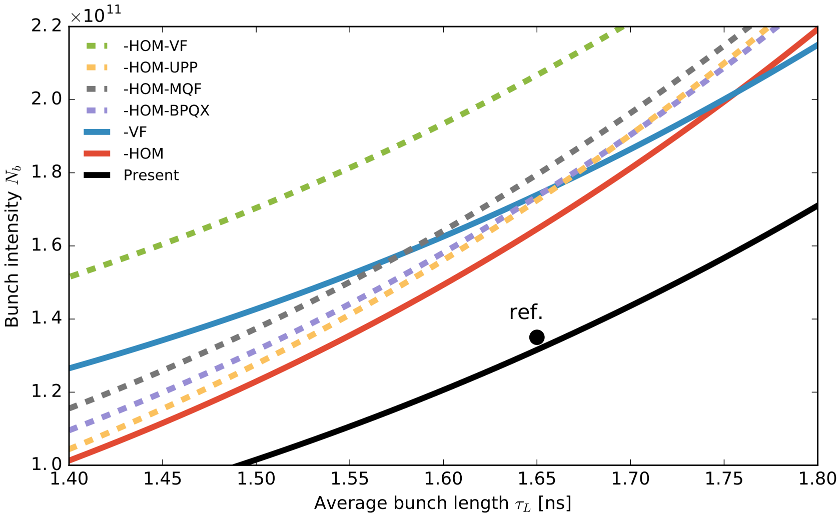

Figure 6.2 – Stability threshold for 72 bunches with $V_{200} = 7$ MV and $V_{800} = 0.7$ MV, for various impedance removal. VF stands for the removals of all vacuum flanges, BPQX/MQF/UPP describes the removal of subsets of the vacuum flanges, and HOM of the 630 MHz HOM.

The maximum intensity reachable in the SPS is also limited due to beam loading [85]. To overcome this limitation, an RF upgrade is planned and further studies were done to see potential gain of impedance reduction for future RF configurations.

6.4 Projection for future RF configurations

During the Long Shutdown 2 (LS2, 2019-2020), the configuration of the 200 MHz RF system will change (to 4 cavities of 3 sections and 2 cavities of 4 sections) and the RF power will be upgraded [10], reducing the limitation from beam loading and increasing the maximum RF voltage to $V_{200} = 10$ MV for an intensity of $N_b = 2.4 \times 10^{11}$ ppb (25 ns beam). The upgrade will also change the total impedance of the TWC, both for the main harmonic and the HOMs. The main impedance for 3 sections was estimated using Eq. (1.34) [9], while the HOMs impedance was scaled down by 40% with respect to the 4 sections TWC, keeping R_s/Q constant.

Results of simulations for the future RF configuration are compared with the current one in Fig. 6.3. It can be seen that the achievable parameters without impedance reduction would be $N_b = 2.1 \times 10^{11}$ ppb at $\tau_{\text{av}} = 1.65$ ns, still below the requirements for the HL-LHC project.

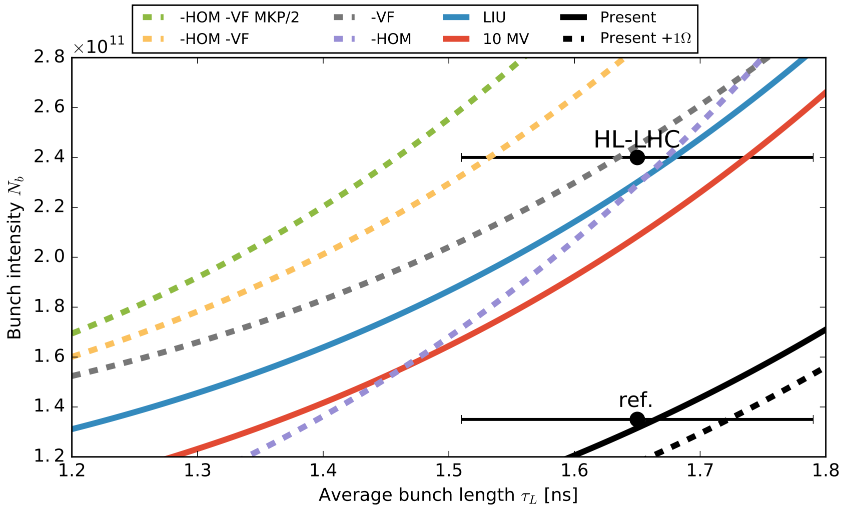

Figure 6.3 – Effect of the removal of different impedance sources with $V_{200} = 10$ MV and $V_{800} = 1$ MV to reach the HL-LHC goal: VF corresponds to the removal of all vacuum flanges, HOM to the removal of the 630 MHz HOM and MKP/2 to the effect of reducing the MKP kickers impedance by a factor of 2, LIU stands for the baseline impedance reduction for realistic models. The present configurations are shown for comparison (black), together with the effect of an extra $\text{Im}\mathcal{Z}/n \approx 1\,\Omega$ (dashed black).

Therefore, an impedance reduction is foreseen to increase further the instability threshold. Again, the effect of the different impedance sources was tested by completely removing them. Results are shown in Fig. 6.3. Similar to the present 7 MV case, removing either the VF or the HOM at 630 MHz gives a small gain, while removing both is better and would allow reaching the HL-LHC requirements with a small margin. Concerning the kickers, the biggest contributors are the MKPs. A reduction by a factor 2 of their impedance would further increase the beam stability and the margin.

The impedance sources cannot be completely removed so realistic values were used based on a shielding model designed for the most critical vacuum flanges. Its impedance was estimated through RF simulations [33]. Results for the realistic impedance reduction considered now as the LIU baseline are shown in Fig. 6.3. The reference point after the RF upgrade and a realistic impedance reduction is $N_b = 2.3 \times 10^{11}$ ppb at $\tau_{\mathrm{av}} = 1.65$ ns. The gain is even bigger for larger bunches. In operation the bunch to bunch variability may lead to beam configurations where the spread in bunch length is bigger than in simulations. The beam stability would then be limited by the shortest bunches, and the dependence of the intensity with bunch length is important. Finally, there is no margin with respect to the HL-LHC requirements. Further damping of the HOM at 630 MHz would give more margin, but as it is already being damped by a dedicated coupler further damping is difficult. Another source of uncertainty is that some impedance may still be missing from the impedance model according to synchrotron frequency shift studies (see Chapter 2). The missing impedance can be simplified as a constant reactive impedance of $\mathrm{Im}\mathcal{Z}/n \approx 1\,\Omega$, and the effect on the stability for the present configuration is shown in Fig. 6.3. The effect is to reduce the overall instability threshold, making our prediction slightly more pessimistic whilst remaining in the uncertainty. It shows mainly the minimum margin that should be taken to safely reach future requirements.

The RF upgrade and the impedance reduction make it possible to reach the HL-LHC requirements but with a very small margin, other means to increase it were also studied [85].

6.5 Conclusions

The simulations using the BLonD code and the SPS impedance model are able to reproduce the intensity threshold observed for the LHC-type beam at flat top. According to simulations with the upgraded RF systems and impedance reduction, the HL-LHC goal is achievable, but with a tight margin. Since the present SPS impedance model was demonstrated to be a reasonable representation of the reality, more complex studies for the LHC-type beam can be done, taking into account the acceleration ramp, the influence of the LLRF feedbacks, and optimisations of the 800 MHz RF parameters.

The AWAKE project will also benefit from the SPS upgrade in the baseline of the LIU project. The increased available RF voltage will allow to get smaller bunch length, while the impedance reduction will stabilise the bunch for smaller longitudinal emittances and higher intensities. This will allow to reach higher peak current for the proton bunch. Another benefit of the present SPS impedance model reliability is that it is now possible to perform particle simulations to find means of optimisation to the operational cycle (e.g. adjustments of the 800 MHz RF parameters which were shown in Chapter 5 to be important), and evaluate the expected gain in terms of bunch peak current after the SPS upgrade.

Summary and conclusions

Beam measurements of the impedance are very useful to verify the impedance model of a machine and identify missing elements. The focus of this thesis was the CERN SPS longitudinal impedance causing serious limitations in terms of future LHC beam intensity due to longitudinal instabilities. Several methods of beam measurements of the impedance to extract the maximum information about the SPS impedance were applied and presented in this thesis.

In Chapter 2, the results of the study of the synchrotron frequency shift with intensity were presented. The aim was to probe the reactive part of the SPS effective impedance. The synchrotron frequency shift measurements are usually done for a fixed bunch length. An important contribution of this thesis was the study of the synchrotron frequency shift as a function of bunch length, allowing to probe the complex frequency structure of the SPS impedance. Overall, measurements and simulations using the present SPS impedance model are in good agreement. The bunch length dependence of the shift was exploited to evaluate the frequency distribution of some possible missing impedance from the remaining small difference between measurements and simulations. This contribution could be described by a resonator at $f_r \approx 350$ MHz with $R_s/Q \approx 3$ kΩ.

Another result of the synchrotron frequency shift study was that the longitudinal space charge impedance should be included into the SPS model at flat bottom energy. Consequently, the longitudinal space charge impedance was accurately calculated and added to the present SPS impedance model, as presented in Chapter 3. This was done by taking into account the exact variation of the beam size and aperture geometry along the ring. Its value for the proton beams at 26 GeV/c is $\mathrm{Im}\mathcal{Z}/n \approx (-1.1 \pm 0.1)\ \Omega$, with small variations depending on the optics, and the transverse and longitudinal emittances.

The high frequency impedance contributions were also probed by measuring the modulation of long bunches at injection in the SPS with the RF voltage switched off. The results are described in Chapter 4. The modulation is caused by microwave instability, which is also critical in the SPS with RF on. Therefore, this method revealed the most important impedance sources driving microwave instability in the SPS, which are the vacuum flanges. Most of the peaks in the unstable bunch spectrum could be associated with the resonant frequencies of the various types of vacuum flanges. In addition, their contribution in terms of resistive impedance was evaluated from the measured bunch energy loss during the instability, and results are in good agreement with simulations. The remaining deviations were used to show that an existing impedance source at $f \approx 1.8$ GHz is under-evaluated in the present model, or another one is probably missing.

Another means to benchmark the SPS impedance model is to try to reproduce the measured instabilities in macroparticle simulations. In this thesis, single bunch instabilities were measured during the acceleration ramp and results are presented in Chapter 5. First, the measured instabilities for proton bunches and for various RF configurations (single and double RF operation) were reproduced in simulations. In single RF operation, the intensity threshold of the instability is in reasonable agreement with measurements. This study also revealed the non-monotonic behaviour of the intensity threshold with the injected emittance, which is related to the bunch length dependence of the synchrotron frequency shift in the SPS. In double RF operation, the agreement of measurements and macroparticle simulations rely on the corrections of the effective parameters of the fourth harmonic RF system. Including the suggested corrections based on the measurements of the bunch profile tilt, a good agreement is reached between simulations and measurements. Beam instabilities were also measured for ion bunches and their threshold could be associated with loss of Landau damping. Simulations using the present SPS impedance model were able to reproduce the instability threshold for ions at flat top. Since the loss of Landau damping is determined by the effective reactive impedance, these results were another evidence of the validity of the present SPS impedance model.

The main achievement of this thesis is the proof that the present SPS impedance model (with the addition of the longitudinal space charge impedance) is a reasonable representation of the reality. This statement is based on the good overall agreement between measurements, simulations and theory. Some possible missing impedance sources were revealed (and their estimations can be used to search for the corresponding element in the ring), but they should have a small impact on the beam stability. Therefore, the present SPS impedance can be used for studies of the future machine performance with applications to the LIU and the AWAKE projects. Initial calculations were done in the frame of this thesis, showing that the impedance reduction of the vacuum flanges and a further damping of the 630 MHz high order mode of the main RF system should help to reach the requirements of the HL-LHC project. The SPS RF upgrade and the impedance reduction in the baseline LIU project are also beneficial for the AWAKE project. Together with the single bunch instability study presented in this thesis, the RF parameters can be optimised to find better beam parameters for the AWAKE experiment.

A Synthèse en français

Un des enjeux pour les projets futurs en physique basés sur l'utilisation d'accélérateurs de particules est le besoin de faisceaux de haute intensité, qui peuvent être limités par des effets collectifs. Le projet High Luminosity LHC (HL-LHC) au CERN requiert une intensité de faisceau deux fois plus élevée par rapport aux performances actuelles [3]. Cependant, le Super Proton Synchrotron (SPS) qui est le dernier accélérateur de la chaîne d'injecteurs du LHC est le principal facteur limitant en termes d'intensité de faisceau, à cause du *beam loading* (réduction de la tension accélératrice dans la cavité radiofréquence (RF) due à la charge du faisceau) et des instabilités du faisceau dans le plan longitudinal. Pour résoudre ce problème, un des buts du projet LHC Injector Upgrade (LIU) est d'identifier les sources des limitations du SPS, et d'évaluer les solutions possibles [4].

Les instabilités du faisceau sont dues à l'interaction du faisceau avec son environnement. Les changements de géométrie de la chambre à vide sont la source de perturbations électromagnétiques après le passage d'une particule chargée, qui peuvent être représentées par l'impédance de couplage $\mathcal{Z}$. Pour établir un modèle d'impédance du SPS, un inventaire des éléments de la machine a été accompli et leur contribution en impédance évaluée par des simulations numériques et des mesures en laboratoire. Le modèle actuel inclut les systèmes RF accélérateurs (cavités à ondes progressives, *Travelling Wave Cavities*, TWC) et leurs résonances d'ordres supérieurs (*High-Order Modes*, HOM), les aimants d'injection/extraction (*kickers*), les brides de vide (dont les plus importantes contributions sont celles à proximité des aimants focalisant QF), les ports de pompage, ainsi que d'autres sources mineures. Les effets de charge d'espace longitudinale peuvent aussi être modélisés par une impédance de couplage $(\mathrm{Im}\mathcal{Z}/n)_{\mathrm{SC}}$ et ne sont pas négligeables à basse énergie dans le SPS. Le modèle d'impédance actuel du SPS, qui est utilisé dans les simulations de dynamique faisceau est représenté Fig. A.1 (voir Introduction pour plus de détails).

L'impédance d'un accélérateur de particules peut être mesurée en utilisant le faisceau comme une sonde, afin de vérifier le modèle existant ou d'identifier des sources manquantes. Les caractéristiques du faisceau sont mesurées pour différentes intensités et comparées avec des formules analytiques ou des simulations de type macro-particules utilisant le modèle

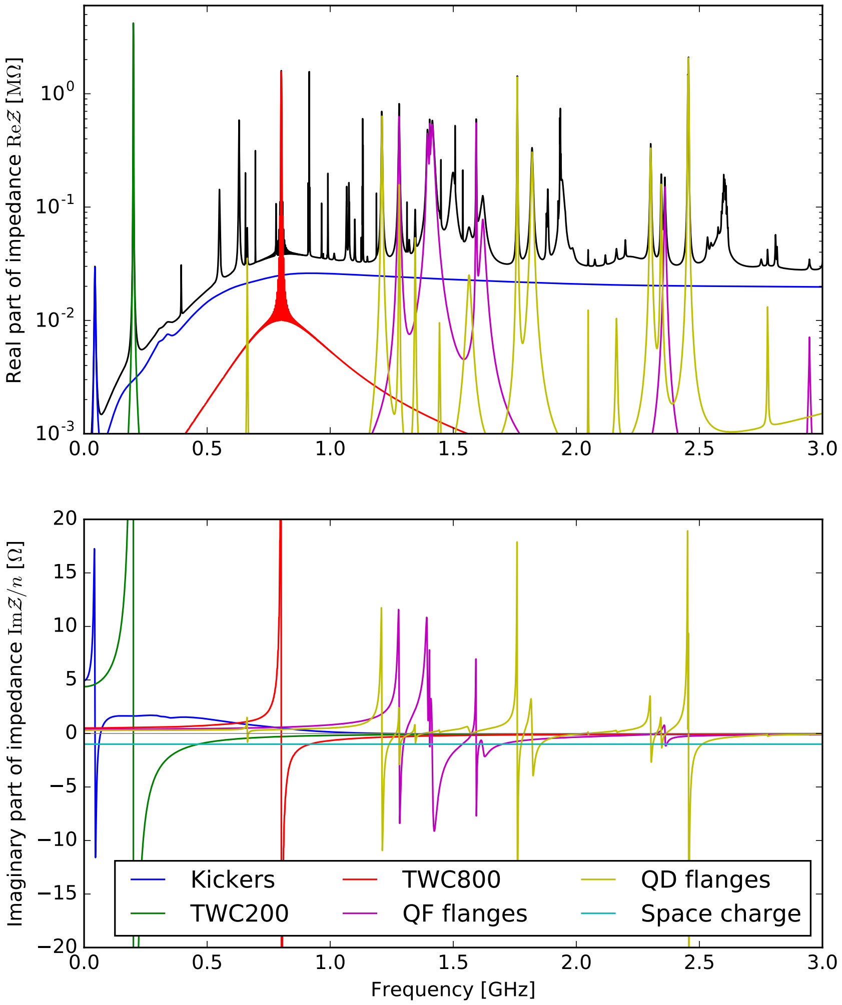

Figure A.1 – Le modèle d'impédance actuel du SPS jusqu'à 3 GHz: partie résistive (haut) et réactive (bas). Les groupes d'impédance les plus importants sont représentés en couleurs, le modèle total est représenté en noir (uniquement la partie résistive).

d'impédance. Les mesures effectuées avec un faisceau stable donnent des informations sur l'impédance effective, correspondant au produit du spectre du faisceau avec l'impédance. La partie résistive de l'impédance Re$\mathcal{Z}$ et la partie réactive Im$\mathcal{Z}$ ont des effets différents sur le faisceau, et diverses méthodes sont utilisables pour les mesurer séparément. L'impédance peut aussi être mesurée en utilisant un faisceau instable. Dans ce cas, le spectre du faisceau inclut aussi des informations spécifiques sur la source d'impédance responsable de l'instabilité. Dans le cadre de cette thèse, les méthodes classiques de mesures de l'impédance avec le faisceau ont été approfondies et étendues, afin d'extraire le maximum d'information sur l'impédance complexe du SPS. Les bases théoriques nécessaires aux études présentées dans cette thèse ainsi que les bases du code de simulation BLonD (*Beam Longitudinal Dynamics*) sont présentées au Chapitre 1.

La première approche consiste à sonder la partie réactive de l'impédance du SPS en étudiant le déplacement de la fréquence synchrotronique en fonction de l'intensité. Les résultats de cette étude sont présentés au Chapitre 2. Les mesures du déplacement en fréquence synchrotronique se font habituellement pour une longueur de paquet de particules fixe. Une contribution importante de cette thèse est l'étude du déplacement en fréquence synchrotronique en fonction de la longueur du paquet de particules, permettant de sonder la structure en fréquence de l'impédance réactive du SPS. Dans l'ensemble, l'accord entre les mesures et les simulations est raisonnable. La dépendance du déplacement de la fréquence synchrotronique avec la longueur du paquet de particules a été exploitée afin d'évaluer la distribution en fréquence d'une source d'impédance potentiellement manquante au modèle. Celle-ci peut être décrite par un résonateur avec une fréquence résonance de $f_r \approx 350$ MHz et une impédance $R_s/Q \approx 3$ kΩ (voir Fig. A.2).

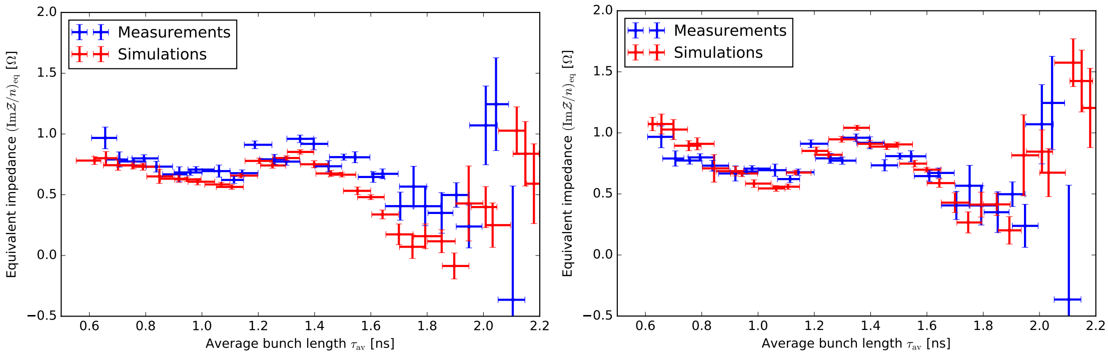

(a) Modèle SPS actuel

(b) Source d'impédance ajoutée

Figure A.2 – Impédance équivalente du SPS en fonction de la longueur du paquet de particules mesurée (bleu) et simulée (rouge): avec le modèle d'impédance actuel du SPS (gauche), et en ajoutant une source d'impédance supplémentaire avec $f_r = 350$ MHz et $R/Q = 3$ kΩ (droite).

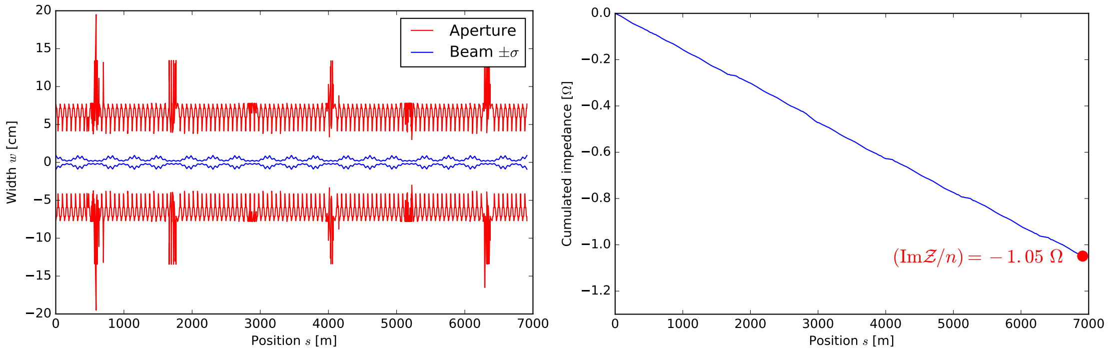

(a) Taille ouverture et faisceau

(b) Impédance charge d'espace

Figure A.3 – Taille de l'ouverture de la chambre à vide et du faisceau dans le plan horizontal (gauche) et l'impédance de charge d'espace intégrée le long de l'anneau (droite), pour une émittance transverse normalisée de $\varepsilon_{x,y} = 1,7\,\mu$m et un écart relatif des particules en quantité de mouvement de $\delta_{\mathrm{rms}} = 1,1 \times 10^{-3}$.

Un autre résultat de l'étude précédente est la mise en évidence que l'impédance de la charge d'espace longitudinale n'est pas négligeable à basse énergie et doit être intégrée au modèle d'impédance du SPS. Par conséquent, l'impédance de la charge d'espace longitudinale a été calculée précisément en prenant en compte la variation de la taille transverse du paquet de particules relativement à la taille de l'ouverture de la chambre à vide, le long de l'anneau (voir Fig. A.3). Les résultats sont détaillés au Chapitre 3. Pour un faisceau de protons à 26 GeV/c, sa valeur est de $\mathrm{Im}\mathcal{Z}/n \approx (-1.1 \pm 0.1)\ \Omega$, avec de petites variations en fonction de l'optique appliquée, et de l'émittance transverse et longitudinale.

Les contributions d'impédance à haute fréquence ont aussi été sondées en mesurant la modulation de longs paquets de particules à l'injection dans le SPS, avec la tension RF éteinte. Les résultats sont décrits dans le Chapitre 4. La modulation du profil du paquet est due à l'instabilité micro-onde (*microwave*), qui est aussi critique dans le SPS avec la tension RF allumée. Par conséquent, cette méthode révèle aussi les sources d'impédance responsables de l'instabilité *microwave* dans le SPS, qui sont les brides de vide. La plupart des pics dans le spectre du paquet de particules instable ont pu être associés aux fréquences de résonance des différents types de brides de vide. De plus, leur contribution en termes d'impédance résistive a été évaluée depuis les mesures des pertes d'énergie du paquet de particules durant l'instabilité (via le déplacement du paquet en temps durant l'acquisition), et les résultats sont en accord avec les simulations. Les écarts restants entre mesures et simulations ont été utilisés pour montrer qu'une source d'impédance à $f \approx 1.8$ GHz est soit sous-évaluée, soit manquante au modèle d'impédance présent (voir Fig A.4).

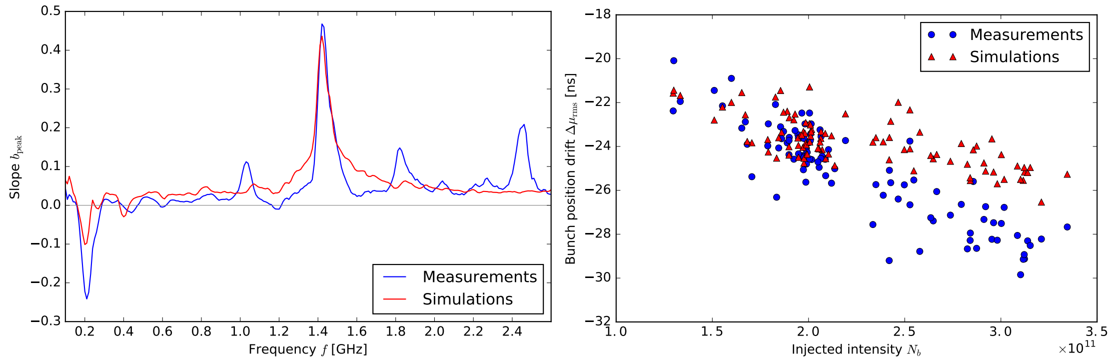

(a) Modulation du spectre

(b) Déplacement du paquet en temps

Figure A.4 – Comparaison des mesures (bleu) et des simulations (rouge) pour la modulation du spectre du paquet de particules dû à l'instabilité *microwave* (gauche), et la perte d'énergie durant l'acquisition mesurée depuis le déplacement en temps du paquet (droite).

Un autre moyen d'évaluer le modèle d'impédance du SPS est d'essayer de reproduire les instabilités mesurées dans les simulations. Les instabilités d'un paquet de particules unique ont été mesurées durant la rampe d'accélération et les résultats sont présentés dans le Chapitre 5. Tout d'abord, les mesures d'instabilités pour un paquet de protons ont été étudiées et comparées avec les simulations pour diverses configurations RF (opération en avec un ou deux systèmes RF actifs avec multiple harmonique). En opération avec un unique système RF, le seuil en intensité de l'instabilité obtenu dans les simulations est en bon accord avec les mesures. Cette étude a aussi révélé le comportement non monotone du seuil de l'instabilité en fonction de l'émittance longitudinale à l'injection, qui est en relation avec la dépendance du déplacement en fréquence synchrotronique avec la longueur du paquet de particules décrite au Chapitre 2. En opération double RF, l'accord entre les mesures et les simulations repose sur une bonne connaissance des paramètres effectifs du système RF de quatrième harmonique. En incluant dans les simulations les corrections sur ces paramètres, basé sur la mesure de l'inclination du profil du paquet de particules, un meilleur accord est obtenu entre les mesures et les simulations (voir Fig.A.5). Les instabilités du faisceau ont aussi été mesurées pour des paquets d'ions (^{208}Pb^{82+}) et la forte dépendance du seuil de l'instabilité avec la longueur du paquet de particules a pu être associée avec la perte de l'amortissement de Landau. Les simulations faites à haute énergie incluant le modèle d'impédance du SPS présent sont en bon accord avec les mesures. Comme la perte d'amortissement de Landau dépend surtout de la partie réactive de l'impédance effective de la machine, ce résultat est une preuve supplémentaire de la validité du modèle d'impédance du SPS présent (voir Fig. A.6).

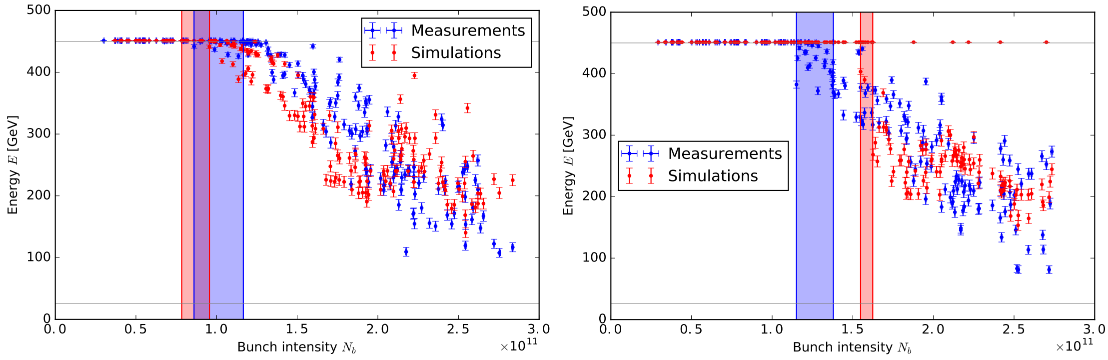

(a) 1RF - CBA (b) 1RF - HV

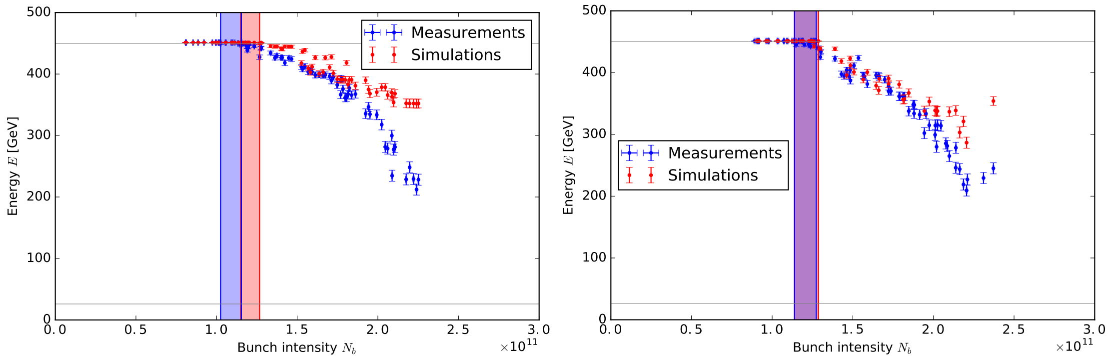

(c) 2RF - CBA (d) 2RF - HV

Figure A.5 – Énergie durant la rampe d'accélération à laquelle le paquet de protons devient instable, en fonction de l'intensité du paquet. Les mesures (bleu) sont comparées aux simulations (rouge), en opération RF unique (haut) et double RF (bas). Deux programmes RF sont présentés: CBA (gauche) et HV (droite) (voir Fig. 5.1).

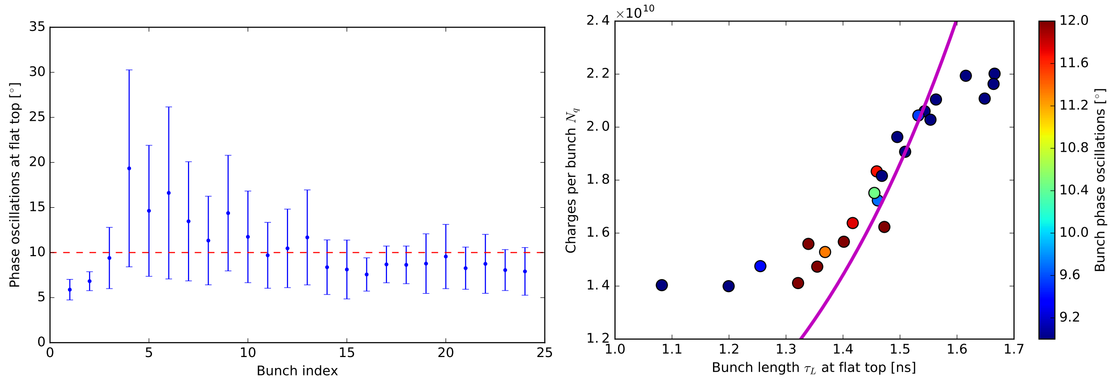

(a) Oscillations dipolaires pour chaque paquet

(b) Seuil d'instabilité simulé et mesures

Figure A.6 – Stabilité des paquets d'ions en fonction de leur position le long du faisceau (gauche). Les premiers paquets correspondent à ceux les plus courts et les moins intenses, qui sont ceux les plus instables (droite, accord avec la perte d'amortissement de Landau). Le seuil d'instabilité (magenta) est obtenu en simulations avec le modèle d'impédance du SPS présent.

La principale réalisation de cette thèse est la preuve que le modèle d'impédance du SPS présent (auquel a été ajouté l'impédance de charge d'espace longitudinale) est une représentation raisonnable de la réalité. Cette affirmation est basée sur l'accord général entre les mesures, les simulations et la théorie. Des potentielles sources d'impédance manquantes ont été révélées (et l'estimation de leur amplitude et distribution en fréquence peut être utilisée pour rechercher l'élément correspondant dans l'anneau), mais devraient avoir un faible impact sur la stabilité du faisceau. Par conséquent, ce modèle d'impédance du SPS peut être utilisé pour étudier les performances futures de la machine pour les projets LIU et AWAKE. Des premiers calculs ont été effectués dans le cadre de cette thèse, montrant que la réduction d'impédance des brides de vide et l'amortissement supplémentaire du HOM à 630 MHz du système RF principal devrait aider à atteindre les prérequis du projet HL-LHC, avec une marge cependant restreinte. L'amélioration des systèmes RF du SPS ainsi que la réduction impédance du projet LIU vont aussi bénéficier au projet AWAKE. En effet, ce projet requiert l'accélération d'un paquet unique de protons de très haute intensité et l'étude de stabilité présentée dans cette thèse permet l'optimisation des paramètres RF pour produire un meilleur faisceau.

Bibliography

[1] ATLAS collaboration, "Observation of a new particle in the search for the Standard Model Higgs boson with the ATLAS detector at the LHC ," *Physics Letters B*, vol. 716, no. 1, pp. 1 – 29, 2012.

[2] CMS collaboration, "Observation of a new boson at a mass of 125 GeV with the CMS experiment at the LHC," *Physics Letters B*, vol. 716, no. 1, pp. 30 – 61, 2012.

[3] G. Apollinari, I. Béjar Alonso, O. Brüning, M. Lamont, and L. Rossi, "High-Luminosity Large Hadron Collider (HL-LHC): Preliminary Design Report," Tech. Rep. CERN-2015-005, CERN, Geneva, Switzerland, Dec 2015.

[4] H. Damerau, A. Funken, R. Garoby, S. Gilardoni, B. Goddard, K. Hanke, A. Lombardi, D. Manglunki, M. Meddahi, B. Mikulec, G. Rumolo, E. Shaposhnikova, M. Vretenar, and J. Coupard, "LHC Injectors Upgrade, Technical Design Report, Vol. I: Protons," Tech. Rep. CERN-ACC-2014-0337, CERN, Geneva, Switzerland, Dec 2014.

[5] J. Coupard, H. Damerau, A. Funken, R. Garoby, S. Gilardoni, B. Goddard, K. Hanke, D. Manglunki, M. Meddahi, G. Rumolo, R. Scrivens, and E. Shaposhnikova, "LHC Injectors Upgrade, Technical Design Report, Vol. II: Ions," Tech. Rep. CERN-ACC-2016-0041, CERN, Geneva, Apr 2016.

[6] A. Caldwell, E. Gschwendtner, K. Lotov, P. Muggli, and M. Wing, "AWAKE Design Report: A Proton-Driven Plasma Wakefield Acceleration Experiment at CERN," Tech. Rep. CERN-SPSC-2013-013, Apr 2013.

[7] UA1 collaboration, "Experimental observation of isolated large transverse energy electrons with associated missing energy at s=540 GeV," *Physics Letters B*, vol. 122, no. 1, pp. 103 – 116, 1983.

[8] UA2 collaboration, "Observation of single isolated electrons of high transverse momentum in events with missing transverse energy at the CERN pp collider," *Physics Letters B*, vol. 122, no. 5–6, pp. 476 – 485, 1983.

[9] G. Dôme, "The SPS acceleration system travelling wave drift-tube structure for the CERN SPS," Tech. Rep. CERN-SPS-ARF-77-11, May 1977.

[10] E. N. Shaposhnikova, E. Ciapala, and E. Montesinos, “Upgrade of the 200 MHZ RF System in the CERN SPS,” in *Proceedings of IPAC2011*, (San Sebastián, Spain), pp. 214–216, Aug 2011.

[11] L. D. Landau, “On the vibrations of the electronic plasma,” *J. Phys.(USSR)*, vol. 10, pp. 25–34, 1946. [Zh. Eksp. Teor. Fiz.16,574(1946)].

[12] E. Shaposhnikova, “Signatures of microwave instability,” in *Beam measurement. Proceedings, Joint US-CERN-Japan-Russia School on Particle Accelerators, Montreux and Geneva, Switzerland, May 11-20, 1998*, pp. 351–377, 1999.

[13] T. Bohl, T. P. R. Linnecar, E. Shaposhnikova, and J. Tückmantel, “Study of Different Operating Modes of the 4th RF Harmonic Landau Damping System in the CERN SPS,” in *Proceedings of EPAC98*, (Stockholm, Sweden), pp. 978–980, Jun 1998.

[14] T. Argyropoulos, *Longitudinal Beam Instabilities in a Double RF System.* PhD thesis, National Technical University of Athens, Athens, 2015.

[15] T. Argyropoulos, “Longitudinal Microwave Instability in a Multi-RF System,” in *Proceedings of HB2014*, (East-Lansing, MI, USA), pp. 404–408, November 2014.

[16] E. Shaposhnikova, “Longitudinal stability of the LHC beam in the SPS,” Tech. Rep. SL-Note-2001-031-HRF, CERN, Geneva, Aug 2001.

[17] H. Damerau, M. E. Angoletta, T. Argyropoulos, P. Baudrenghien, A. Blas, T. Bohl, A. Butterworth, A. Findlay, R. Garoby, S. Gilardoni, S. Hancock, W. Höfle, J. Molendijk, E. Montesinos, M. Paoluzzi, D. Perrelet, C. Rossi, and E. Shaposhnikova, “Upgrades of the RF Systems in the LHC Injector Complex,” in *Proceedings of HB2014*, (East-Lansing, MI, USA), pp. 165–169, November 2014.

[18] B. W. Zotter and S. A. Kheifets, *Impedances and wakes in high-energy particle accelerators.* Singapore: World Scientific, 1998.

[19] A. W. Chao, *Physics of collective beam instabilities in high energy accelerators.* New York, NY: Wiley, 1993.

[20] Y. H. Chin. http://abci.kek.jp/abci.htm.

[21] O. Napoly, Y. H. Chin, and B. Zotter, “A generalized method for calculating wake potentials,” *Nuclear Instruments and Methods in Physics Research Section A: Accelerators, Spectrometers, Detectors and Associated Equipment*, vol. 334, no. 2, pp. 255 – 265, 1993.

[22] CST MICROWAVE STUDIO. https://www.cst.com/products/cstmws.

[23] F. Caspers, “Impedance Determination from Bench Measurements,” in *Handbook of Accelerator Physics and Engineering* (A. W. Chao and M. Tigner, eds.), ch. 7.5.1, pp. 745–750, Singapore: World Scientific, 1999.

[24] J. E. Varela Campelo, T. Argyropoulos, T. Bohl, F. Caspers, J. Esteban Müller, J. Ghini, A. Lasheen, D. Quartullo, B. Salvant, E. Shaposhnikova, and C. Zannini, "An Extended SPS Longitudinal Impedance Model," in *Proceedings of IPAC2015*, (Richmond, VA, USA), pp. 360–362, May 2015.

[25] E. Métral, G. Arduini, T. Bohl, H. Burkhardt, R. Calaga, F. Caspers, H. Damerau, T. Kroyer, H. Medina, G. Rumolo, B. Salvant, M. Schokker, E. Shaposhnikova, B. Spataro, and J. Tückmantel, "CERN SPS Impedance in 2007," in *Proceedings of EPAC08*, (Genoa, Italy), pp. 1691–1693, Aug 2008.

[26] B. Salvant, N. Mounet, C. Zannini, G. Arduini, O. Berrig, F. Caspers, A. Grudiev, E. Métral, G. Rumolo, E. Shaposhnikova, B. Zotter, M. Migliorati, and B. Spataro, "Update of the SPS Impedance Model," in *Proceedings of IPAC'10*, (Kyoto, Japan), pp. 2057–2059, Jun 2010.

[27] LIU-SPS Beam Dynamics Working Group meetings. http://cern.ch/spsu/.

[28] P. Kramer, J. Varela Campelo, F. Caspers, C. Vollinger, and E. Montesinos, "In situ Measurements of the SPS 200MHz Accelerating Cavity III," Tech. Rep. CERN-ACC-NOTE-2015-0021, Aug 2015.

[29] T. Roggen, R. Calaga, F. Caspers, and C. Vollinger, "Measurements on the SPS 200 MHz Travelling Wave Cavity towards an Impedance Model," Tech. Rep. CERN-ACC-NOTE-2016-0051, Jul 2016.

[30] D. Bazyl and J. E. Varela Campelo, "Characterization of the SPS 800MHz Travelling Wave Cavities," Tech. Rep. CERN-STUDENTS-Note-2015-009, Jul 2015.

[31] C. Zannini, *Electromagnetic Simulation of CERN accelerator Components and Experimental Applications.* PhD thesis, Ecole Polytechnique, Lausanne, Mar 2013. Presented 15 Apr 2013.

[32] T. Kroyer, F. Caspers, and E. Gaxiola, "Longitudinal and Transverse Wire Measurements for the Evaluation of Impedance Reduction Measures on the MKE Extraction Kickers," Tech. Rep. CERN-AB-Note-2007-028, CERN, Geneva, Jul 2007.

[33] J. E. Varela Campelo, "Longitudinal Impedance Characterization of the CERN SPS Vacuum Flanges," in *Proceedings of IPAC2015*, (Richmond, VA, USA), pp. 363–365, May 2015.

[34] B. Salvant, G. Arduini, C. Boccard, F. Caspers, A. Grudiev, R. Jones, E. Métral, G. Rumolo, C. Zannini, B. Spataro, D. Alesini, M. Migliorati, F. Roncarolo, and R. Calaga, "Coupling Impedance of the CERN SPS Beam Position Monitors," in *Proceedings of PAC09*, (Vancouver, BC, Canada), pp. 4646–4648, Sep 2009.

[35] J. Ghini, "Longitudinal Impedance of the SPS Pumping Ports," Tech. Rep. CERN-STUDENTS-Note-2014-187, Sep 2014.

[36] CERN Impedance meetings. https://impedance.web.cern.ch/impedance/.

[37] A. Lasheen, “Longitudinal Space Charge in the SPS,” Tech. Rep. CERN-ACC-NOTE-2016-0074, Dec 2016.

[38] E. Shaposhnikova, T. Bohl, H. Damerau, K. Hanke, T. Linnecar, B. Mikulec, J. Tan, and J. Tückmantel, “Reference Measurements of the Longitudinal Impedance in the CERN SPS,” in *Proceedings of PAC09*, (Vancouver, Canada), pp. 4667–4669, May 2009.

[39] T. Bohl, T. P. R. Linnecar, and E. Shaposhnikova, “Impedance Reduction in the CERN SPS as seen from Longitudinal Beam Measurements,” in *Proceedings of EPAC 2002*, (Paris, France), pp. 1446–1448, May 2002.

[40] E. Shaposhnikova, T. Argyropoulos, T. Bohl, F. Caspers, A. Lasheen, J. Esteban Muller, B. Salvant, H. Timko, and J. E. Varela, “Identification of High-Frequency Resonant Impedance in the CERN SPS,” in *Proceedings of IPAC2014*, (Dresden, Germany), pp. 1416–1418, June 2014.

[41] S. Y. Lee, *Accelerator Physics; 2nd ed.* London: World Scientific, 2004.

[42] J. L. Laclare, “Bunched beam coherent instabilities,” in *Proceedings of CAS 1985 Vol. I*, (Geneva, Switzerland), pp. 264–326, 1987.

[43] K. Y. Ng, *Physics of intensity dependent beam instabilities.* Hoboken, NJ: World Scientific, 2006.

[44] J. F. Esteban Müller, K. Iliakis, A. Lasheen, D. Quartullo, and H. Timko. http://blond.web.cern.ch/.

[45] H. Timko, J. E. Müller, A. Lasheen, and D. Quartullo, “Benchmarking the Beam Longitudinal Dynamics Code BLonD,” in *Proc. of International Particle Accelerator Conference (IPAC’16), Busan, Korea, May 8-13, 2016*, no. 7 in International Particle Accelerator Conference, (Geneva, Switzerland), pp. 3094–3097, JACoW, June 2016. doi:10.18429/JACoW-IPAC2016-WEPOY045.

[46] J. MacLachlan, “User’s guide to ESME v. 8.0,” 1993.

[47] G. Rumolo and F. Zimmermann, “Practical user guide for HEADTAIL,” Tech. Rep. SL-Note-2002-036-AP, CERN, Geneva, Nov 2002.

[48] A. Shishlo, S. Cousineau, J. Holmes, and T. Gorlov, “The Particle Accelerator Simulation Code PyORBIT,” *Procedia Computer Science*, vol. 51, pp. 1272 – 1281, 2015.

[49] V. Forte, E. Benedetto, A. Lombardi, and D. Quartullo, “Longitudinal Injection Schemes For the CERN PS Booster at 160 MeV Including Space Charge Effects,” in *Proceedings of IPAC2015*, (Richmond, VA, USA), pp. 378–381, 2015.

[50] M. Migliorati and L. Palumbo, “Multibunch and multiparticle simulation code with an alternative approach to wakefield effects,” *Phys. Rev. ST Accel. Beams*, vol. 18, p. 031001, Mar 2015.

[51] P. W. Krempl, “The Abel-type Integral Transformation with the Kernel (t2-x2)-1/2 and its Application to Density Distributions of Particle Beams,” Tech. Rep. CERN Note MPS/Int. BR/74-1, CERN, 1974.

[52] M. A. Allen, J. M. Paterson, J. R. Rees, and P. B. Wilson, “Beam Energy Loss to Parasitic Modes in Spear II,” *IEEE Transactions on Nuclear Science*, vol. 22, pp. 1838–1842, June 1975.

[53] J. F. Esteban Müller, P. Baudrenghien, T. Mastoridis, E. Shaposhnikova, and D. Valuch, “High-accuracy diagnostic tool for electron cloud observation in the LHC based on synchronous phase measurements,” *Phys. Rev. ST Accel. Beams*, vol. 18, p. 112801, Nov 2015.

[54] N. S. Sereno, Y. C. Chae, K. C. Harkay, A. H. Lumpkin, S. V. Milton, and B. X. Yang, “A potpourri of impedance measurements at the Advanced Photon Source storage ring,” in *Proceedings of the 1997 Particle Accelerator Conference (Cat. No.97CH36167)*, vol. 2, pp. 1700–1702 vol.2, May 1997.

[55] M. Migliorati, N. Biancacci, H. Damerau, S. Persichelli, G. Sterbini, and L. Ventura, “Measurements of the CERN PS Longitudinal Resistive Coupling Impedance,” in *Proc. of International Particle Accelerator Conference (IPAC’16), Busan, Korea, May 8-13, 2016*, no. 7 in International Particle Accelerator Conference, (Geneva, Switzerland), pp. 626–629, JACoW, June 2016. doi:10.18429/JACoW-IPAC2016-MOPOR014.

[56] E. Shaposhnikova, T. Bohl, A. Hofmann, T. P. R. Linnecar, and J. Tückmantel, “Energy loss of a single bunch in the SPS,” Tech. Rep. CERN-AB-Note-2004-017, CERN, Geneva, Mar 2004.

[57] S. Chattopadhyay, *Some fundamental aspects of fluctuations and coherence in charged-particle beams in storage rings.* Geneva: CERN, 1984.

[58] M. Blaskiewicz, J. Brennan, P. Cameron, and W. Fischer, “Longitudinal Impedance Measurement in RHIC,” in *Proceedings of EPAC 2002*, (Paris, France), pp. 1488–1490, May 2002.

[59] M. Blaskiewicz, J. Brennan, and K. Mernick, “Longitudinal impedance of RHIC,” in *Proceedings of IPAC2015*, (Richmond, VA, USA), pp. 746–747, May 2015.

[60] E. Shaposhnikova, T. Bohl, and T. Linnecar, “Longitudinal Peak Detected Schottky Spectrum,” in *Proceedings of HB2010*, (Morschach, Switzerland), pp. 363–367, September 2010.

[61] J. F. Esteban Müller, T. Argyropoulos, T. Bohl, N. Mounet, E. Shaposhnikova, and H. Timko, “Beam measurements of the LHC impedance and validation of the impedance model,” in *Proceedings of IPAC2014*, (Dresden, Germany), pp. 1698–1700, Jun 2014.

[62] D. Boussard, “Schottky Noise and Beam Transfer Function Diagnostics,” in *Advanced accelerator physics. 1.*, 1986.

[63] M. Migliorati, S. Persichelli, H. Damerau, S. Gilardoni, S. Hancock, and L. Palumbo, “Beam-wall interaction in the CERN Proton Synchrotron for the LHC upgrade,” *Phys. Rev. ST Accel. Beams*, vol. 16, p. 031001, Mar 2013.

[64] J. Haïssinski, “Exact longitudinal equilibrium distribution of stored electrons in the presence of self-fields,” *Il Nuovo Cimento B (1971-1996)*, vol. 18, no. 1, pp. 72–82, 1973.

[65] B. W. Zotter, “Potential-well bunch lengthening,” Tech. Rep. CERN-SPS-81-14-DI, CERN, Geneva, 1981.

[66] V. I. Balbekov and S. V. Ivanov, “Thresholds of longitudinal instability of bunched beam in the presence of dominant inductive impedance,” Tech. Rep. IHEP-91-14, Protvino Inst. High Energy Phys., Protvino, Feb 1991.

[67] T. Bohl, T. P. R. Linnecar, and E. Shaposhnikova, “Measuring the Resonance Structure of Accelerator Impedance with Single Bunches,” *Phys. Rev. Lett.*, vol. 78, pp. 3109–3112, Apr 1997.

[68] B. Salvant, L. Rivkin, and E. Metral, *Impedance model of the CERN SPS and aspects of LHC single-bunch stability.* PhD thesis, Ecole Polytechnique, Lausanne, Switzerland, 2010. Presented on 04 Mar 2010.

[69] H. Bartosik, G. Iadarola, Y. Papaphilippou, G. Rumolo, B. Salvant, and C. Zannini, “TMCI thresholds for LHC single bunches in the CERN SPS and comparison with simulations,” in *Proceedings of IPAC2014*, (Dresden, Germany), pp. 1407–1409, Jun 2016.

[70] C. Zannini, H. Bartosik, G. Iadarola, G. Rumolo, and B. Salvant, “Benchmarking the CERN-SPS Transverse Impedance Model with Measured Headtail Growth Rates,” pp. 402–405, 2015.

[71] S. Hancock, “Improved Longitudinal Blow-up and Shaving in the Booster,” Tech. Rep. CERN-ATS-Note-2013-040 MD, Jul 2013.

[72] T. Bohl. private communications, 2016.

[73] H. Timko, T. Argyropoulos, T. Bohl, H. Damerau, J. F. Esteban Müller, S. Hancock, and E. Shaposhnikova, “Longitudinal transfer of rotated bunches in the CERN injectors,” *Phys. Rev. ST Accel. Beams*, vol. 16, p. 051004, May 2013.

[74] A. Lasheen, T. Bohl, S. Hancock, E. Radvilas, T. Roggen, and E. Shaposhnikova, “Single Bunch Longitudinal Instability in the CERN SPS,” in *Proc. of International Particle Accelerator Conference (IPAC’16), Busan, Korea, May 8-13, 2016*, pp. 1670–1673, June 2016.

[75] L. Wang and Y. Li, “Analysis of the longitudinal space charge impedance of a round uniform beam inside parallel plates and rectangular chambers,” *Phys. Rev. ST Accel. Beams*, vol. 18, p. 024201, Feb 2015.

[76] H. Bartosik. private communications, 2015.

[77] L. Wang. private communications, 2015.

[78] E. Benedetto, J. L. Abelleira, C. Bracco, V. Forte, B. Mikulec, and G. Rumolo, “CERN PS Booster Upgrade and LHC Beams Emittance,” in *Proceedings of IPAC2015*, (Richmond, VA, USA), pp. 3897–3900, May 2015.

[79] E. Shaposhnikova, “Nonlinear bunch motion in an accelerator with reactive impedance,” in *Proceedings of EPAC96*, (Barcelona, Spain), pp. 1021–1023, Jul 1996.

[80] G. Papotti, “A Beam Quality Monitor for LHC Beams in the SPS,” in *Proceedings of EPAC08*, (Genoa, Italy), pp. 3324–3326, Sep 2008.

[81] E. Radvilas, A. Lasheen, and E. Shaposhnikova, “Simulations of single-bunch instability on flat top,” Tech. Rep. CERN-STUDENTS-Note-2015-048, Aug 2015.

[82] F. Antoniou, G. Arduini, H. Bartosik, T. Bohl, S. Cave, K. Cornelis, D. Manglunki, and Y. Papaphilippou, “Performance of SPS Low transition Energy Optics for LHC Ion Beam,” in *Proceedings of IPAC2013*, (Shanghai, China), pp. 1667–1669, May 2013.

[83] D. Boussard and G. Lambert, “Reduction of the apparent impedance of wide band accelerating cavities by rf feedback,” *IEEE Transactions on Nuclear Science*, vol. 30, pp. 2239–2241, Aug 1983.

[84] P. Baudrenghien, “Control of strong beam loading: Results with beam,” in *Proceedings of Chamonix XI*, (Chamonix, France), Jan 2001.

[85] E. Shaposhnikova *et al.*, “Removing Known SPS Intensity Limitations for High Luminosity LHC Goals,” in *Proc. of International Particle Accelerator Conference (IPAC’16), Busan, Korea, May 8-13, 2016*, no. 7 in International Particle Accelerator Conference, (Geneva, Switzerland), pp. 989–991, JACoW, June 2016. doi:10.18429/JACoW-IPAC2016-MOPOY058.

université PARIS-SACLAY
ÉCOLE DOCTORALE
PHENIICS

Titre: Mesures de l'Impédance Longitudinale avec le Faisceau du Super Proton Synchrotron au CERN

Mots clés: *accélérateurs de particules, dynamique longitudinale du faisceau, mesures avec le faisceau, CERN SPS, impédance de couplage, instabilités du faisceau*

Résumé: Un des défis pour les futurs projets en physique basé sur les accélérateurs de particules est le besoin de faisceaux à hautes intensités. Les effets collectifs sont cependant une limitation majeure qui peuvent détériorer la qualité du faisceau ou limiter l'intensité maximale à cause des pertes. Le CERN SPS, qui est le dernier injecteur pour le LHC, n'est actuellement pas en mesure de délivrer les faisceaux requis pour les futurs projets à cause des instabilités longitudinales.

Les nombreux équipements dans la machine (les cavités RF accélératrices, les aimants d'injection et d'extraction, les brides de vide, etc.) entrainent des variations dans la géométrie et les matériaux de la chambre dans laquelle le faisceau transite. Les interactions électromagnétiques internes au faisceau (charge d'espace) et du faisceau avec son environnement sont représentées par une impédance de couplage qui affectent le mouvement des particules et mènent à des instabilités pour des intensités élevées de faisceau. Par conséquent, les sources d'impédance critiques doivent être identifiées et des solutions évaluées. Pour avoir un modèle d'impédance fiable d'un accélérateur, les contributions de tous les équipements dans l'anneau doivent être évaluées à partir de simulations et de mesures électromagnétiques.

Dans cette thèse, le faisceau lui-même est utilisé comme une sonde de l'impédance de la machine en mesurant le déplacement de la fréquence synchrotronique avec l'intensité et la longueur du paquet, ainsi que la modulation de longs paquets injectés avec la tension RF éteinte. Ces mesures sont comparées avec des simulations par macroparticules en utilisant le modèle d'impédance du SPS existant, et les déviations sont étudiées pour identifier les sources d'impédance manquantes pour raffiner le modèle.

L'étape suivante consiste à reproduire en simulations les instabilités mesurées pour un paquet unique durant l'accélération. Grâce à l'amélioration du modèle d'impédance, une meilleure compréhension des mécanismes de l'instabilité est rendue possible pour les faisceaux de protons et d'ions.

Finalement, le modèle pour les simulations étant digne de confiance, il est utilisé pour estimer les caractéristiques du faisceau après les améliorations prévues du SPS pour le projet High Luminosity-LHC au CERN.

Title: Beam Measurements of the Longitudinal Impedance of the CERN Super Proton Synchrotron

Key words: *particle accelerators, longitudinal beam dynamics, beam-based measurements, CERN SPS, beam coupling impedance, beam instabilities*

Abstract: One of the main challenges of future physics projects based on particle accelerators is the need for high intensity beams. However, collective effects are a major limitation which can deteriorate the beam quality or limit the maximum intensity due to losses. The CERN SPS, which is the last injector for the LHC, is currently unable to deliver the beams required for future projects due to longitudinal instabilities.

The numerous devices in the machine (accelerating RF cavities, injection and extraction magnets, vacuum flanges, etc.) lead to variations in the geometry and material of the chamber through which the beam is travelling. The electromagnetic interaction within the beam (space charge) and of the beam with its environment are described by a coupling impedance which affects the motion of the particles and leads to instabilities for high beam intensities. Consequently, the critical impedance sources should be identified and solutions assessed. To have a reliable impedance model of an accelerator, the contributions of all the devices in the ring should be evaluated from electromagnetic simulations and measurements.

In this thesis, the beam itself is used to probe the machine impedance by measuring the synchrotron frequency shift with intensity and bunch length, as well as the line density modulation of long bunches injected with the RF voltage switched off. These measurements are compared with macroparticle simulations using the existing SPS impedance model, and the deviations are studied to identify missing impedance sources and to refine the model.

The next important step is to reproduce in simulations the measured single bunch instabilities during acceleration, in single and double RF system operation. Thanks to the improved impedance model, a better understanding of instability mechanisms is achieved for both proton and ion beams.

Finally, as the simulation model was shown to be trustworthy, it is used to estimate the beam characteristics after the foreseen SPS upgrades the High Luminosity-LHC project at CERN.

Université Paris-Saclay
Espace Technologique / Immeuble Discovery
Route de l'Orme aux Merisiers RD 128 / 91190 Saint-Aubin, France